

THESE

Présentée devant



(INSTITUT NATIONAL DES SCIENCES APPLIQUEES DE LYON)

Pour obtenir

LE GRADE DE DOCTEUR

Ecole Doctorale des Sciences de l'Ingénieur de Lyon:

Mécanique, Energétique, Génie civil, Acoustique (MEGA)

Spécialité:

MECANIQUE – GENIE MECANIQUE

Par

Muhammad ASAD

**ELABORATION OF CONCEPTS AND METHODOLOGIES TO STUDY
PERIPHERAL DOWN-CUT MILLING PROCESS FROM
MACRO-TO-MICRO SCALES**

**ELABORATION DE CONCEPTS ET METHODOLOGIES POUR
L'ETUDE DU FRAISAGE DE PROFIL LORS DU PASSAGE
D'ECHELLES MACRO-MICRO**

Thèse soutenue le 17 septembre 2010 devant la commission d'examen

Rapporteurs :

Martin BÄKER

Professeur des universités (TU Braunschweig, Germany)

Joël RECH

Maître de Conférences/HDR (ENISE, France)

Examineurs :

Jean-Claude BOYER

Professeur des universités (INSA de Lyon, France)

Benjamin HAGEGE

Maître de Conférences (UTC, France)

Philippe LORONG

Professeur des universités (ENSAM ParisTech, France)

Directeurs de thèse :

Tarek MABROUKI

Maître de Conférences (INSA de Lyon, France)

Jean François RIGAL

Professeur des universités (INSA de Lyon, France)



LaMCoS, INSA-Lyon, CNRS UMR5259, F69621.
(Laboratoire de Mécanique des Contacts et des Structures)
20, Av. Albert Einstein, 69621 Villeurbanne Cedex, France.



**INSA Direction de la Recherche-Ecoles Doctorales-Quadriennal
2007-2010**

| SIGLE | ECOLE DOCTORALE | NOM ET COORDONNEES DU RESPONSABLE |
|------------------|--|---|
| CHIMIE | CHIMIE DE LYON http://sakura.cpe.fr/ED206 M. Jean Marc LANCELIN Insa : R. GOURDON | M. Jean Marc LANCELIN Université Claude Bernard Lyon 1 Bât CPE 43 bd du 11 novembre 1918 69622 VILLEURBANNE Cedex Tél : 04.72.43 13 95 Fax : lancelin@hikari.cpe.fr |
| E.E.A. | ELECTRONIQUE, ELECTROTECHNIQUE, AUTOMATIQUE http://www.insa-lyon.fr/eea M. Alain NICOLAS Insa : C. PLOSSU ede2a@insa-lyon.fr Secrétariat : M. LABOUNE AM. 64.43 – Fax : 64.54 | M. Alain NICOLAS Ecole Centrale de Lyon Bâtiment H9 36 avenue Guy de Collongue 69134 ECULLY Tél : 04.72.18 60 97 Fax : 04 78 43 37 17 eea@ec-lyon.fr Secrétariat : M.C. HAVGOUDOUKIAN |
| E2M2 | EVOLUTION, ECOSYSTEME, MICROBIOLOGIE, MODELISATION http://biomserv.univ-lyon1.fr/E2M2 M. Jean-Pierre FLANDROIS Insa : H. CHARLES | M. Jean-Pierre FLANDROIS CNRS UMR 5558 Université Claude Bernard Lyon 1 Bât G. Mendel 43 bd du 11 novembre 1918 69622 VILLEURBANNE Cédex Tél : 04.26 23 59 50 Fax 04 26 23 59 49 06 07 53 89 13 e2m2@biomserv.univ-lyon1.fr |
| EDISS | INTERDISCIPLINAIRE SCIENCES- SANTÉ Sec : Safia Boudjema M. Didier REVEL Insa : M. LAGARDE | M. Didier REVEL Hôpital Cardiologique de Lyon Bâtiment Central 28 Avenue Doyen Lépine 69500 BRON Tél : 04.72.68 49 09 Fax :04 72 35 49 16 Didier.revel@creatis.uni-lyon1.fr |
| INFOMATHS | INFORMATIQUE ET MATHÉMATIQUES http://infomaths.univ-lyon1.fr M. Alain MILLE Secrétariat : C. DAYEYAN | M. Alain MILLE Université Claude Bernard Lyon 1 LIRIS - INFOMATHS Bâtiment Nautibus 43 bd du 11 novembre 1918 69622 VILLEURBANNE Cedex Tél : 04.72. 44 82 94 Fax 04 72 43 13 10 infomaths@bat710.univ-lyon1.fr - alain.mille@liris.cnrs.fr |
| Matériaux | MATERIAUX DE LYON M. Jean Marc PELLETIER Secrétariat : C. BERNAVON 83.85 | M. Jean Marc PELLETIER INSA de Lyon MATEIS Bâtiment Blaise Pascal 7 avenue Jean Capelle 69621 VILLEURBANNE Cédex Tél : 04.72.43 83 18 Fax 04 72 43 85 28 Jean-marc.Pelletier@insa-lyon.fr |
| MEGA | MECANIQUE, ENERGETIQUE, GENIE CIVIL, ACOUSTIQUE M. Jean Louis GUYADER Secrétariat : M. LABOUNE PM : 71.70 –Fax : 87.12 | M. Jean Louis GUYADER INSA de Lyon Laboratoire de Vibrations et Acoustique Bâtiment Antoine de Saint Exupéry 25 bis avenue Jean Capelle 69621 VILLEURBANNE Cedex Tél :04.72.18.71.70 Fax : 04 72 43 72 37 mega@lva.insa-lyon.fr |
| ScSo | ScSo* M. OBADIA Lionel Insa : J.Y. TOUSSAINT | M. OBADIA Lionel Université Lyon 2 86 rue Pasteur 69365 LYON Cedex 07 Tél : 04.78.69.72.76 Fax : 04.37.28.04.48 Lionel.Obadia@univ-lyon2.fr |

*ScSo : Histoire, Géographie, Aménagement, Urbanisme, Archéologie, Science politique, Sociologie, Anthropologie

*To all Parents
&
Teachers*

Acknowledgments

Taking first foot steps towards presenting new understandings is a worthy experience. The dream of this lifetime experience can not be seen without the help and support of some earnest people. I would like to express my deepest gratitude to the project directors Pr. Tarek Mabrouki and Pr. Jean François Rigal for their support, contribution and enthusiasm for this work. Indeed, I feel honoured to remain under their learned supervision. None of this would have been possible without their consistent help and valuable guidance.

I owe my sincere thanks to Pr. Michel Brunet for sharing his expertise, his extended cooperation and fruitful suggestions in coding Vumat user subroutine; being a major part of this thesis.

I am extremely grateful to Pr. Martin Bäker, Pr. Jean-Claude Boyer, Pr. Benjamin Hagege, Pr. Philippe Lorong and Pr. Joël Rech for dedicating their valuable time in evaluating this work.

I would also like to express my indebtedness to Miss D. Alkadee, Mr. Y. Zhang, Mr. C. Courbon, Mr. S. M. A. Shah, Dr. M. A. Khan, Dr. M. Zain, Mr. F. Cazes, Dr. N. Tardif, Pr. F. Morestin, Pr. T. Elguedj, Pr. M. Coret, Pr. A. Gravouil, Dr. F. Cyprian, Mr. A.A. Taimoor, Mr. A. Memon, Mr. S. Akbar, Mr. T. Akbar, Mme. I. Comby and all others for sharing their knowledge and extending their assistance in completing this task.

How I can forget to extend my special thanks to contemporary research friend François Girardin. His socio-cultural knowledge is as impressive as technical. I really acknowledge his ever extended help in every aspect of my stay in France.

I would like to acknowledge the financial assistance provided by Higher Education Commission (HEC) of Pakistan in collaboration with Government of France through an Overseas Research Scholarship Program.

Finally, I would like to take this opportunity to express my heartfelt thanks to my parents, for their utmost love and constant encouragement. Special thanks to Ali, Meena and Javaria for their unremitting support, friendship and understanding during this time.

I will not say I failed 1000 times, I will say that I discovered 1000 ways that can cause failure.

Thomas Alva Edison

Abstract

Today, finite element method is a sufficiently developed technique, bringing an indispensable help to the engineers, during design and optimization stages of the engineering products. In certain cases, its role exceeds from the simple technological assistance and makes it possible to consider physical laws in the intimacy of the mediums inaccessible to the experimentation (nuclear fission and fusion, cracks propagation in the materials,...). In this context, the present contribution brings a scientific and technological comprehension of the chip formation process. The investigation of chip genesis is not an aim in itself, but it can inform what actually happens during the process. From experimental and application point of view, the work is focused on the machining of an aeronautic Aluminium alloy A2024-T351.

This study has been accomplished with four principle stages. Initially, an orthogonal cutting model for the case of turning process has been established. The work makes it possible to emphasize equally on the discretization level leading to an optimised mesh generation to capture physical phenomenon, as well as on the material behaviour level considering crucial aspects of damage and fracture energy.

Onward this model was adapted to the case of the down cut milling (with a null helix angle), where the removed material has a half crescent moon like form, presenting a continuously variable chip thickness tending towards zero (with a constant width). This model makes it possible to distinguish the macroscopic cutting zone from the microscopic one, based on the cut thickness. The well-known size effect phenomenon of micromechanics was thus found during macro to micro cutting passage increasing material strength, due to strain rate hardening characteristics of the material. This phenomenon in machining is well-known and corresponds to the quasi exponential increase in the specific cutting energy with the reduction of the cut thickness.

To facilitate the exploitation and to propose a physical tool for better comprehension of the material removal (especially at micro cutting level) to the scientific community and industry, in the third stage modified Johnson-Cook material model (strain gradient-based approach) of the equivalent stress has been formulated in ABAQUS[®]/EXPLICIT via its user subroutine VUMAT. In spite of the modelling difficulties a complete cutting model integrating the size effect phenomenon has been presented. The aim is to provide a numerical data on the

machined surface which can be compared with the experimental results. As it is the microscopic cutting part in high frequency and high speed dynamics domain which generates the machined surface.

During the fourth stage, the model was completely developed to simulate the down cut milling of Aluminium alloy A2024-T351. In addition to the size effect relating to the chip, the dynamic aspects relating to the machining system were taken into account through the proposition of a multi level cutting model, named hybrid dynamic cutting model (HDC-model). The proposed model combines the rigidity of a high speed milling machine (tool, tool holder, rotor,...) at the macroscopic level with the mechanics of mesoscopic level chip formation.

Finally, turning and milling cutting experiments were carried out to validate the suggested models. The numerical results were compared with experimental ones at each stage.

In general the results are in good agreement. It is however necessary to note that a number of parameters can affect the numerical model results. The predictive character of the model is primarily limited to the physical characteristics of the machined material. Under these circumstances one finds itself in the purely experimental investigations of 1970-80s, when the concept of tool material coupling (TMC) was conceived for the very first time. Today's approach, which is both experimental and numerical, however makes it possible to strongly reduce the costs and to quantify very interesting local phenomena such as for example in this contribution:

- chip segmentation tendency leading to fragmentation under certain cutting conditions,
- the chip contact length with tool cutting face,
- the amplitude of the machined surface defects due to global dynamics of machining system,
-

Keywords:

Finite element simulation, Orthogonal cutting model, Johnson-Cook, Damage evolution, Size effect, Strain rate, Strain gradient, Vumat user routine, Chip segmentation, Dynamic cutting modelling, A2024-T351, Experimentation

Résumé

Aujourd'hui, la méthode des éléments finis est suffisamment développée pour apporter aux ingénieurs, une aide indispensable lors des étapes de conception et d'optimisation des produits manufacturés. Dans certains cas, cette aide dépasse la simple assistance technologique et permet de considérer des lois physiques dans l'intimité d'un milieu inaccessible aux expériences (fission et fusion nucléaire, propagation des fissures dans les matériaux,...). C'est dans ce contexte à la fois scientifique et technologique que porte notre contribution sur la formation du copeau. D'un point de vue applicatif et expérimental, notre étude est centrée sur l'usinage de l'alliage d'Aluminium A2024-T351

Cette étude a été accomplie avec 4 étapes principales. La première étape porte sur la mise au point d'un modèle numérique 2D, de coupe orthogonale en tournage. Ce travail permet de choisir des solutions de détails pour ce modèle numérique, aussi bien au niveau de la discrétisation et de la partition du maillage qu'au niveau du comportement du matériau usiné sur les aspects cruciaux d'endommagement et d'énergie de rupture.

Lors de la deuxième étape ce modèle a été adapté au cas du fraisage de profil en avalant avec un angle d'hélice nul, où la matière susceptible d'être enlevée a une forme en demi lune, constant sur sa largeur, présente une épaisseur continûment variable et tendant vers zéro. Ce travail et les résultats obtenus permettent de distinguer la zone de coupe macroscopique de la zone microscopique à partir de l'épaisseur coupée. L'effet de taille bien connu en micromécanique a ainsi été retrouvé lors de ce passage macro-micro à travers l'influence de l'écrouissage due à la vitesse de déformation du matériau. Le phénomène bien connu expérimentalement de l'augmentation quasi exponentielle de l'énergie spécifique de coupe avec la diminution de l'épaisseur coupée a été étudié en relation avec les divers aspects de cet effet de taille.

Pour faciliter l'exploitation et proposer un outil de compréhension physique de l'enlèvement de matière à la communauté scientifique et à l'industrie, dans une troisième étape, le modèle de comportement de « Johnson-Cook » modifié par une approche basée sur le second gradient de déformation a été développé dans ABAQUS[®]/EXPLICIT sous la forme d'un sous programme (ou sous-routine VUMAT).

Finalement, au cours de la quatrième étape, l'application a été complètement développée pour simuler le fraisage de profil en avalant, de l'alliage d'Aluminium A2024-T351. En plus de l'effet de taille interne au copeau, les aspects dynamiques liés au comportement du système usinant ont été pris en compte à travers un modèle multi-échelle nommé « modèle dynamique hybride de coupe (HDC-modèle) » qui combine la rigidité équivalente d'une fraiseuse à grande vitesse (outil, porte-outil, broche, ...) au niveau macroscopique avec la mécanique de formation de copeau au niveau mésoscopique.

Cette application intégrant à la fois les effets d'échelles a pour but de fournir des données numériques sur la surface usinée qui puissent être comparées à des résultats expérimentaux. Malgré les difficultés de modélisation nous avons tenu à élaborer ce modèle complet car c'est bien la partie microscopique de la coupe en dynamique haute fréquence ou grande vitesse qui génère la surface usinée.

Pour finir, des coupes expérimentales ont été exécutées en tournage et en fraisage pour valider les modèles proposés. Les résultats numériques sont ainsi comparés à ceux expérimentaux à chacune des étapes.

De manière générale la concordance des résultats est bonne. Il faut cependant noter le grand nombre de paramètres des modèles numériques qui certains d'entre eux peuvent être des paramètres de recalage expérimental. Il apparaît donc que le caractère prédictif du modèle est limité essentiellement par les caractéristiques physiques de la matière usinée. On se retrouve dans la situation purement expérimentale des années 1970-80 qui a vu naître la notion de couple outil-matière (COM). L'approche d'aujourd'hui, à la fois expérimentale et numérique permet cependant de réduire fortement les coûts et de quantifier des phénomènes locaux très intéressants comme par exemple dans notre contribution :

- La propension à la segmentation et donc à la fragmentation dans certaines conditions de coupe,
- La longueur du contact copeau, face de coupe,
- L'amplitude des défauts de la surface usinée due à la dynamique globale,
- ...

Mots Clés:

Simulation numérique, Élément fini, Coupe orthogonal, Johnson-Cook, Endommagement, Effet de taille, Vitesse de déformation, Second gradient de déformation, Sous-routine Vumat, Segmentation de copeau, Modèle de coupe dynamique, A2024-T351, Expérimentation

Contents

| | |
|---|-------------|
| Abstract | i |
| Résumé | iii |
| Contents..... | v |
| List of figures | ix |
| List of tables..... | xiii |
| Nomenclature..... | xv |
| Introduction | 1 |
| 1 Literature Review | 5 |
| 1.1 Introduction | 5 |
| 1.2 Machining of materials by milling | 6 |
| 1.3 Principal of orthogonal cutting | 8 |
| 1.4 Chip formation..... | 8 |
| 1.5 Finite element modelling of macro/traditional machining process | 10 |
| 1.5.1 Approaches and movement description | 11 |
| 1.5.2 Constitutive material models and chip separation techniques | 12 |
| 1.5.3 Heat generation and thermal assumption | 14 |
| 1.5.4 Tool - chip interface | 14 |
| 1.6 Micro machining and size effect phenomenon..... | 17 |
| 1.7 Conclusions | 22 |
| 2 Dry Machining Modelling of an Aluminium Alloy at Mesoscopic Scale..... | 25 |
| 2.1 Introduction | 25 |
| 2.2 ABAQUS [®] software and its explicit dynamic approach..... | 26 |
| 2.3 Finite element model for orthogonal turning..... | 29 |
| 2.3.1 Geometrical model and hypothesis | 29 |

| | |
|---|-----------|
| 2.3.2 Tool - workpiece interactions | 30 |
| 2.3.3 Meshing..... | 32 |
| 2.3.4 Material behaviour model and chip separation criteria..... | 34 |
| 2.3.5 Heat transfer modelling..... | 41 |
| 2.4 Experiment for orthogonal turning | 42 |
| 2.4.1 Experimental device..... | 42 |
| 2.4.2 Geometrical analysis | 43 |
| 2.4.3 Video acquisition results | 44 |
| 2.4.4 Cutting force measurement | 46 |
| 2.5 Results and discussion on orthogonal turning operation..... | 47 |
| 2.6 Modelling of an orthogonal peripheral down-cut milling case | 54 |
| 2.6.1 Geometrical and material models | 54 |
| 2.6.2 Meshing and interactions | 56 |
| 2.7 Results and discussion on orthogonal down-cut milling..... | 56 |
| 2.8 Conclusions | 61 |
| 3 Concept and Methodology for Micro Cutting Modelling..... | 63 |
| 3.1 Introduction | 63 |
| 3.2 Modelling methodology | 64 |
| 3.2.1 Geometrical model and hypothesis | 64 |
| 3.2.2 Material behaviour law | 66 |
| 3.2.3 Model validation by numerical elementary tests | 71 |
| 3.3 Down-cut peripheral milling experiments..... | 77 |
| 3.4 Results and analysis..... | 80 |
| 3.4.1 Temperature effect on material strengthening | 80 |
| 3.4.2 Strain rate effect on material strengthening | 80 |
| 3.4.3 Strain gradient effect on material strengthening..... | 83 |
| 3.5 Conclusions | 86 |
| 4 Hybrid Dynamic Cutting (HDC) Model for Milling | 89 |
| 4.1 Introduction | 89 |
| 4.2 Hybrid dynamic cutting model (HDC-Model)..... | 90 |

| | |
|--|------------|
| 4.2.1 Machining system definition at macroscopic level | 92 |
| 4.2.2 Workpiece definition at mesoscopic level..... | 93 |
| 4.3 Results and discussion..... | 94 |
| 4.3.1 Stiffness and damping effects on chip morphology and machined surface topology | 95 |
| 4.3.2 Cutting speed effects on cutting force, chip morphology and machined surface topology | 100 |
| 4.3.3 Stiffness and damping effects on tool - chip interaction and chip shear angle. | 105 |
| 4.4 Conclusions | 107 |
| Synopses and Perspectives..... | 109 |
| Bibliography | 115 |

List of figures

| | |
|--|----|
| Fig. 1.1 Classification of milling operation [CUS10] | 7 |
| Fig. 1.2 Schematic representation of climb or down-cut milling | 7 |
| Fig. 1.3 Schematic representation of conventional or up-cut milling | 8 |
| Fig. 1.4 Schematic representation of orthogonal cutting..... | 8 |
| Fig. 1.5 Principal affected zones in chip formation | 9 |
| Fig. 1.6 Chip formation during micro cutting. | 10 |
| Fig. 1.7 Orthogonal chip formation [HAG08, MAB06] | 11 |
| Fig. 1.8 Movement description in Lagrangian, Eulerian and ALE formulations..... | 12 |
| Fig. 1.9 Frictional and normal stress along the rake face [VAZ07]..... | 15 |
| Fig. 1.10 Specific cutting energy vs uncut chip thickness [BAC52] | 17 |
| Fig. 1.11 Specific cutting energy vs uncut chip thickness [KOP84]..... | 18 |
| Fig. 1.12 Specific cutting energy vs uncut chip thickness [NAK67]..... | 19 |
| Fig. 1.13 Specific cutting energy vs UCT for various rake angles [LUC93]..... | 20 |
| Fig. 1.14 Specific cutting energy vs UCT for various cut material [FUR88] | 20 |
| Fig. 1.15 Specific cutting energy vs UCT for various tool tip radius [KOU02] | 21 |
| Fig. 2.1 ABAQUS [®] calculation methodology [ABQ07] | 27 |
| Fig. 2.2 Geometric model and boundary conditions | 30 |
| Fig. 2.3 Tool-workpiece interactions | 31 |
| Fig. 2.4 Contact stresses between solids | 32 |
| Fig. 2.5 Cutting force plots for various mesh element densities for ($f = 0.4$ mm/rev and $V_C =$ 100 m/min). | 33 |
| Fig. 2.6 Average cutting force versus mesh element densities for ($f = 0.4$ mm/rev and $V_C =$ 100 m/min). | 34 |
| Fig. 2.7 Typical uniaxial stress-strain response of a metal specimen [ABQ07] | 36 |
| Fig. 2.8 Schematic representation of chip formation under mixed loading modes I and II..... | 39 |
| Fig. 2.9 von Mises stress vs equivalent plastic strain plot with linear damage evolution for various element sizes (μm)..... | 40 |
| Fig. 2.10 von Mises stress vs equivalent displacement plot with linear damage evolution for various element sizes (μm)..... | 41 |

| | |
|--|----|
| Fig. 2.11 Workpiece preparation and tool geometry..... | 43 |
| Fig. 2.12 Chips embedded in resin ($f = 0.4$ mm/rev, $V_C = 200, 400$ and 800 m/min)..... | 44 |
| Fig. 2.13 Chip morphology for $f = 0.4$ mm/rev a) $V_C = 200$ m/min and b) $V_C = 800$ m/min... | 44 |
| Fig. 2.14 a) Fragmentation and b) segmentation frequencies according to cutting speed variation for different feed rate values | 44 |
| Fig. 2.15 Fragmentation phenomenon observed with video acquisition for $V_C = 200$ m/min and $f = 0.4$ mm/rev. | 45 |
| Fig. 2.16 Cutting force evolution versus time and (b) its frequency spectrum ($V_C = 200$ m/min, $f = 0.4$ mm/rev)..... | 46 |
| Fig. 2.17 Evolution of cutting force according to cutting speed variation for various feed rate values..... | 47 |
| Fig. 2.18 Computed damage evolution ($f = 0.4$ mm/rev, $V_C = 800$ m/min)..... | 48 |
| Fig. 2.19 Distribution of von Mises equivalent stresses during steady cutting regime ($f = 0.4$ mm/rev and $V_C = 800$ m/min) | 48 |
| Fig. 2.20 Distribution of equivalent plastic strain during steady cutting regime ($f = 0.4$ mm/rev and $V_C = 800$ m/min)..... | 49 |
| Fig. 2.21 Distribution of temperature during steady cutting regime ($f = 0.4$ mm/rev and $V_C =$ 800 m/min) | 49 |
| Fig. 2.22 Chip morphology evolution ($V_C = 200$ m/min and $f = 0.4$ mm/rev) regarding damage variable D (SDEG) and experimental comparison..... | 51 |
| Fig. 2.23 Computed damage variable D (SDEG) according to the distance of initial chip free side | 51 |
| Fig. 2.24 Equivalent von Mises plastic stresses on the machined surface ($V_C = 800$ m/min and $f = 0.4$ mm/rev)..... | 52 |
| Fig. 2.25 Distribution of residual stresses under the machined surface ($V_C = 800$ m/min and f $= 0.4$ mm/rev)..... | 53 |
| Fig. 2.26 Trochoidal paths traced by two cutter teeth..... | 55 |
| Fig. 2.27 Tool workpiece geometrical model and boundary conditions for 2D down-cut milling | 55 |
| Fig. 2.28 Temperature evolution and chip morphology ($G_f = 18$ N/mm, $V_C = 200$ m/min) ... | 57 |
| Fig. 2.29 Experimental chip for A2024-T351 ($V_C = 200$ m/min, $a_p = 4$ mm, $f = 0.4$ mm/rev). | 57 |
| Fig. 2.30 Temperature evolution and chip morphology ($G_f = 16$ N/mm, $V_C = 200$ m/min) ... | 58 |
| Fig. 2.31 Temperature evolution and chip morphology ($G_f = 16$ N/mm, $V_C = 300$ m/min) ... | 59 |
| Fig. 2.32 Temperature evolution and chip morphology ($G_f = 16$ N/mm, $V_C = 400$ m/min) ... | 59 |

| | |
|---|----|
| Fig. 2.33 von Mises stress distribution on machined surface corresponding to segmented chip morphology obtained at $V_C = 400$ m/min..... | 60 |
| Fig. 2.34 Residual stress distribution from machined surface to workpiece core corresponding to chip morphology obtained at $V_C = 400$ m/min..... | 61 |
| Fig. 3.1 Tool workpiece geometrical model and boundary conditions for down-cut milling.. | 66 |
| Fig. 3.2 Chip formation with regard of cutter edge radius (a) Chip formed (b) no chip formed [KIM04a]..... | 70 |
| Fig. 3.3 ABAQUS [®] /EXPLICIT VUMAT programme flow chart developed for the present study | 72 |
| Fig. 3.4 Uni-axial displacement (along y-axis) plot at time = 1 msec a) ABAQUS model b) VUMAT model | 73 |
| Fig. 3.5 von Mises stress vs equivalent plastic strain curves without damage model (at nodes 1 and 2, shown in Fig. 3.4)..... | 74 |
| Fig. 3.6 Temperature curves (at nodes 1 and 2, shown in Fig. 3.4) | 74 |
| Fig. 3.7 Shear displacement plot at time = 1msec a) ABAQUS model b) VUMAT model .. | 75 |
| Fig. 3.8 von Mises stress vs equivalent plastic strain curves without damage model (at node 2, shown in Fig. 3.7)..... | 75 |
| Fig. 3.9 Temperature curves (at node 2, shown in Fig. 3.7) | 76 |
| Fig. 3.10 von Mises stress vs equivalent plastic strain curves with exponential damage evolution model for $G_f = 20$ N/mm (at node 2, shown in Fig. 3.7) | 76 |
| Fig. 3.11 von Mises stress vs equivalent plastic strain curves with linear damage evolution model for $G_f = 20$ N/mm (at node 2, shown in Fig. 3.7) | 77 |
| Fig. 3.12 Coated carbide insert referenced AOMT123608PEER-M a) 3D view b) Optical device generated 2D profile | 78 |
| Fig. 3.13 Workpiece mounted on dynamometer | 79 |
| Fig. 3.14 Schematic representation of the experimental set up..... | 79 |
| Fig. 3.15 Orthogonal down-cut milling force diagram | 79 |
| Fig. 3.16 Maximum secondary shear zone temperatures vs uncut chip thickness h for various cutting speeds (w/o SG) | 80 |
| Fig. 3.17 Specific cutting energy evolution at various uncut chip thickness values (w/o SG) | 81 |
| Fig. 3.18 Simulated tool rake face-chip contact length (μm) for $V_C = 200$ m/min (w/o SG) .. | 82 |
| Fig. 3.19 Simulated tool rake face-chip contact lengths (w/o SG) at various uncut chip thickness for various cutting speeds..... | 83 |

| | |
|---|-----|
| Fig. 3.20 Specific cutting energy evolution for various uncut chip thickness values at different cutting speeds (at $V_C = 800$ m/min forces were not registered) | 84 |
| Fig. 3.21 von Mises stress plot at uncut chip thickness value of $22 \mu\text{m}$ at $V_C = 200$ m/min a)w/o SG b) with SG | 85 |
| Fig. 3.22 Experimental chip, $V_C = 200$ m/min..... | 85 |
| Fig. 3.23 von Mises stress plot at uncut chip thickness value of $22 \mu\text{m}$ at $V_C = 800$ m/min a)w/o SG b) with SG | 86 |
| Fig. 4.1 A schematic 2D-representation of the down-cut milling | 90 |
| Fig. 4.2 2D-representation of an industrial milling spindle system (mm) | 91 |
| Fig. 4.3 Tool-workpiece geometrical model and boundary conditions..... | 94 |
| Fig. 4.4 Chip morphology at $V_C = 800$ m/min a) Nodal temperature (NT) distribution on workpiece in the case of (SC-model) b) Experimentally obtained chip..... | 95 |
| Fig. 4.5 Nodal temperature (NT) distribution and chip morphologies at $V_C = 800$ m/min (case of HDC-model, 2 dof and $\zeta_{eq} = 0$) a) $k_{eq} = 2E7$ N/m b) $k_{eq} = 2E8$ N/m | 96 |
| Fig. 4.6 Nodal temperature (NT) distribution and chip morphologies at $V_C = 800$ m/min (case of HDC-model, 2 dof, $\zeta_{eq} = 0$ and $k_{eq} = 2E8$ N/m) | 96 |
| Fig. 4.7 Nodal temperature (NT) distribution and chip morphology at $V_C = 800$ m/min (case of HDC-model with 3 dof and $k_{eq} = 2E8$, $k_{eqr} = 2E8$ Nm/rad a) $\zeta_{eq} = 0$ b) $\zeta_{eq} = 0.1$ | 97 |
| Fig. 4.8 Radial amplified five TTC paths traced for SC and HDC-models considering various parametric values (Table 4.2) at $V_C = 800$ m/min | 98 |
| Fig. 4.9 Radial displacements of machined surface nodes for SC and HDC-models at $V_C = 800$ m/min, (Profile i defined in Table 4.2)..... | 100 |
| Fig. 4.10 Nodal temperature (NT) distribution and chip morphology at $V_C = 300$ m/min a) 2 dof ($k_{eq} = 2E7$ N/m, $\zeta_{eq} = 0$) b) 2 dof ($k_{eq} = 2E8$ N/m, $\zeta_{eq} = 0$) c) 3 dof ($k_{eq} = 2E8$, $k_{eqr} =$ $2E8$ Nm/rad, $\zeta_{eq} = 0$) d) 3 dof ($k_{eq} = 2E8$, $k_{eqr} = 2E8$ Nm/rad, $\zeta_{eq} = 0.1$)..... | 101 |
| Fig. 4.11 Radial displacements of machined surface nodes for SC and HDC-models at $V_C =$ 300 m/min, (Profile i defined in Table 4.2)..... | 102 |
| Fig. 4.12 Cutting force plots for SC and HDC-models considering various parametric values (Table 4.2) at $V_C = 800$ m/min, (Plot i defined in Table 4.2) | 104 |
| Fig. 4.13 Cutting force plots for SC and HDC-models considering various parametric values (Table 4.2) at $V_C = 300$ m/min, (Plot i defined in Table 4.2) | 104 |
| Fig. 4.14 A qualitatively representation of the milling TTC oscillation effects on chip morphology and machined surface | 107 |

List of tables

| | |
|---|-----|
| Table 2.1 Johnson-Cook parameter used to simulate the behaviour of A2024-T351 [TEN06] | 35 |
| Table 2.2 Workpiece and tool physical parameters [KNO07] | 35 |
| Table 2.3 Fracture toughness properties of A2024-T351 [MAT07] | 39 |
| Table 2.4 Cutting force deduced by numerical simulations regarding cutting speed variation | 52 |
| Table 2.5 Workpiece mesh density for 2D milling model | 56 |
| Table 3.1 Material properties used for SG-plasticity based model [XUE02] | 70 |
| Table 4.1 Parameters for macroscopic model | 92 |
| Table 4.2 TTC paths, cutting force plots and machined surface profiles for various machining system parameters | 98 |
| Table 4.3 Effects of cutting speed variation on TTC oscillations (μm), surface profile and chip morphology | 103 |
| Table 4.4 Dynamic cutting effects on friction at 16.5° of TTC angular position | 106 |

Nomenclature

List of symbols

| | |
|----------------------|---|
| A | Initial yield stress (MPa) |
| a_p | Cutting depth or axial depth of cut (mm) |
| a_e | Radial depth of cut (mm) |
| B | Hardening modulus (MPa) |
| b | Burgers vector (nm) |
| C | Strain rate dependency coefficient |
| c_{eq} | Equivalent linear damping of machining system (kg s^{-1}) |
| c_{eqr} | Equivalent rotational damping of machining system ($\text{kg m}^2\text{s}^{-1}\text{rad}^{-1}$) |
| C_p | Specific heat ($\text{Jkg}^{-1}\text{°C}^{-1}$) |
| [C] | Constitutive tensor |
| D | Overall damage variable |
| $D_1\dots D_5$ | Coefficients of Johnson-Cook material shear failure initiation criterion |
| D_T | Tool diameter (mm) |
| E | Young's modulus (MPa) |
| f | Feed rate (mm/rev) |
| $\sum F_{x,y}$ | Summation of forces along x and y axis (N) |
| F_i | Cutting force (N) along various axis ($i = c, r, x, y, z$) |
| $\overline{F_{tot}}$ | Total cutting force (N) |
| G | Shear modulus (MPa) |
| G_f | Fracture energy (N/m) |
| h | Numeric value of the uncut chip thickness (UCT) at a given tool position (mm) |

| | |
|------------|---|
| H_v | Vickers hardness |
| I_z | Moment of inertia of the assembly (tool, tool-holder and rotor) (kg m^2) |
| J | Amount of heat evacuated in chip (less than one) |
| K_C | Fracture toughness ($\text{MPa}\sqrt{\text{m}}$) |
| K_r | Insert attack angle or entering angle (deg) |
| k_{eq} | Equivalent linear stiffness of machining system (N/m) |
| k_{eqr} | Equivalent rotational stiffness of machining system (Nm/rad) |
| L | Mesh characteristic length (square root of the integration point element area (mm)) |
| l | Spring current length (mm) |
| L_C | Tool rake face-chip contact length (μm) |
| l_c | Tool chip transitional length (mm) |
| l_o | Spring initial length (mm) |
| L_P | Length of primary shear zone (mm) |
| l_r | Tool chip contact length from tool tip to a given point on rake face (mm) |
| M | Moment along z-axis (Nm) |
| M_t | Taylor factor |
| m | Thermal softening coefficient |
| m_{eq} | Equivalent moving mass (kg) |
| N | Spindle rotation frequency (rev/min) |
| n | Work-hardening exponent |
| P | Hydrostatic pressure (MPa) |
| $Px_{(i)}$ | X coordinate of the i^{th} tooth of the milling tool ($i=1, 2, \dots, z_t$) |
| $Py_{(i)}$ | Y coordinate of the i^{th} tooth of the milling tool ($i=1, 2, \dots, z_t$) |
| \bar{r} | Nye factor |

| | |
|--------------------------|---|
| R_n | Tool hone edge radius (μm) |
| T | Temperature at a given calculation instant ($^{\circ}\text{C}$) |
| T_{melt} | Melting temperature ($^{\circ}\text{C}$) |
| T_n | Nodal temperature ($^{\circ}\text{C}$) |
| T_{room} | Room temperature ($^{\circ}\text{C}$) |
| t | Cutting time (millisecond) |
| \bar{u} | Equivalent plastic displacement (mm) |
| \bar{u}_f | Equivalent plastic displacement at failure (mm) |
| Δu | Relative displacement of spring element (mm) |
| V_C | Cutting speed (m/min) |
| V_f | Tool feed velocity (mm/min) |
| z_t | Total number of milling tool teeth |
| $P/\bar{\sigma}$ | Stress triaxiality |
| $\bar{\epsilon}$ | Equivalent plastic strain |
| $\dot{\bar{\epsilon}}$ | Plastic strain rate (s^{-1}) |
| $\dot{\bar{\epsilon}}_0$ | Reference strain rate (10^{-3} s^{-1}) |
| $\bar{\epsilon}_f$ | Equivalent plastic strain at failure |
| $\Delta\bar{\epsilon}$ | Equivalent plastic strain increment |
| $\bar{\epsilon}_{0i}$ | Plastic strain at damage initiation |
| $\bar{\sigma}$ | von Mises plastic equivalent stress (MPa) |
| σ_{JC} | Johnson-Cook equivalent stress (MPa) |
| σ_n | Normal stress (MPa) |
| σ_y | Yield stress (MPa) |
| $\tilde{\sigma}$ | Effective or undamaged material stress |

| | |
|--------------|---|
| τ_f | Friction shear stress (MPa) |
| τ_Y | Yield shear stress (MPa) |
| ω | Damage initiation criterion |
| ω_r | Tool angular velocity (rad/s) |
| ν | Poisson's ratio |
| α | Taylor's constant |
| α_d | Expansion coefficient ($\mu\text{m}\cdot\text{m}^{-1}\cdot\text{C}^{-1}$) |
| α_o | Flank/ clearance angle (deg) |
| γ_o | Rake/cutting angle (deg) |
| λ | Thermal conductivity ($\text{W m}^{-1}\cdot\text{C}^{-1}$) |
| λ_s | Mill helix angle (deg) |
| ρ | Density (kg/m^3) |
| ρ_g | Density of geometrically necessary dislocations (GND) |
| ρ_s | Density of statistically stored dislocations (SSD) |
| ρ_T | Total density of dislocations |
| ζ_{eq} | Equivalent damping ratio of machining system |
| θ | Rotational vibration (degree) |
| ϕ | Primary shear angle (deg) |
| μ | Friction coefficient |
| χ | Geometric factor defining the density of geometrically necessary dislocations |
| η | Strain gradient coefficient |
| η_p | Inelastic heat fraction, also called the Taylor–Quinney empirical constant |

List of abbreviations

| | |
|-------------|--|
| ALE | Arbitrary Lagrangian-Eulerian formulation |
| dof | Degree of freedom |
| FE | Finite element |
| FEA | Finite element analysis |
| FEM | Finite element method |
| GND | Geometrically necessary dislocation |
| HDC-model | Hybrid dynamic cutting model |
| JC | Johnson-Cook |
| MD | Molecular dynamics |
| OP | Orthogonal plane |
| Path i | Curve traced by TTC ($i = 1 \dots 5$) |
| Plot i | Curve representing the cutting force ($i = 1 \dots 5$) |
| Profile i | Curve representing the cut surface topology ($i = 1 \dots 5$) |
| rpm | Revolution per minute |
| SC-model | Steady state cutting model corresponding to a perfectly rigid spindle system |
| SCE | Specific cutting energy |
| SG | Strain gradient |
| SSD | Statistically stored dislocations |
| TTC | Tool tip centre |
| UCT | Uncut chip thickness (also presented by a numeric value noted h) |
| w/o | Without |
| 2D/3D | Two/Three dimensional model |

Introduction

Preamble

Machining efficiency at its optimisation stage requires a sufficient comprehension of physical phenomena accompanying tool workpiece interaction. This quest had been aroused since the beginning of material cutting itself. Thanks to the advancement in computational efficiency and numerical techniques developments during last two decades, various models replicating the machining process to improve the phenomenological comprehension of the multi-physical cutting phenomena have been presented. These models have efficiently predicted the useful information like cutting forces, localized temperatures distribution at tool workpiece interface, stress and strain profiles, residual stresses and machined surface topologies, etc.

Nevertheless, the cutting process is characterised by multi-physical aspects which enclose highly nonlinear phenomena due to tool-workpiece contact, large strains, high strain rates, damage, and material behaviour of the machined workpiece. These all aspects make more complex the cutting modelling, especially when passing from macro-cutting scale (traditional cutting) to micro or nanometric cutting ones. Indeed, in micro-scale cutting some encountered issues are fundamentally different from macro-scale one and a simple scaling cannot be used to model phenomena occurring in relationship with micro-machining operations. These issues include differences in the underlying mechanisms of the process, resulting in changes in the chip formation process, machining forces, material specific cutting energy (SCE) and machined surface integrity. For example, in the case of down-milling and at certain tool angular position, the cutting tool edge geometry becomes comparable in size to the uncut chip thickness (UCT), causing a negative effective rake angle. This in turn causes the ploughing phenomenon and an associated elastic-plastic deformation state of the workpiece material. Furthermore, at micrometer length scales of material removal, the well-known size effect phenomenon takes place [BAC52, LUC93, KOU02].

Moreover, by consulting bibliography on machining studies exploiting FEM, it can be noticed that the cutting tool is assumed to be rigid or highly elastic body unaffected by machine dynamics. So, if the dynamic effects of machining system are also included in numerical models, one can well imagine a high level of complexity of machining modelling.

In this framework is situated the present contribution which aims to improve finely the physical comprehension of the tool workpiece interaction during down-milling process based on a numerical cutting model. Initially, an orthogonal cutting model in turning case in which the coupling between material damage evolution and its fracture energy has been established. Onward, this model has been modified and exploited to study the case of macro-to-micro scale milling process (down-cut milling case) for a strain rate dependent aeronautical Aluminium alloy A2024-T351. The introduced modifications were brought in material model behaviour by including the effect of strain gradient at micro scale cutting. The objective is to predict properly the chip morphology evolution and to fully capture the size effect phenomenon. Finally, the built model was exploited to develop a hybrid dynamic cutting model (HDC-model) to reproduce machining under dynamic cutting conditions. The HDC-model takes into account the dynamic effect of the machining system presented by a combination of discrete elements (spring, dashpot) reproducing an industrial milling spindle on a workpiece presented by an isotropic elasto-plastic continuum material.

Problem statement and objectives

Various thermo-mechanical models of macro and micro-cutting processes have been presented by numerous researchers [KIM99a, LIU06, XIN08]. However, the approach of macro-to-micro level cutting with macro cutting tool including the effects of intense strain gradient, when tool approaches from macro-to-micro level of UCT (typical case of down-cut peripheral milling operations) for strain rate dependent materials has not been established yet (to best of my knowledge). Also, no numerical model has been developed to analyze the chip morphology and surface profile generated in cutting by introducing dynamic cutting effects of milling process. This is of vital importance in macro/micro level cutting processes with macro level tools. So, the specific objectives of this thesis could be underlined as following:

- Establishment of a FE model by exploiting the capabilities of ABAQUS[®]/EXPLICIT software to simulate chip formation mechanism for orthogonal down-cut peripheral milling case.

- Development of a chip formation model that can incorporate strain gradient effects when chip thickness approaches to micro-level dimensions during down-cut milling. The aim is to analyze and comprehend the contributions of various factors (temperature, strain rate, etc.) on the nonlinear increase in SCE with the decrease in UCT (size effect phenomenon) for a strain rate dependent Aluminium alloy A2024-T351.
- Development of an understanding of the relative roles of strain gradient, strain rate and temperature drop etc. at micro-level UCT, on material strengthening for a strain rate dependent material. For that, an improvement in the Johnson-Cook (JC) constitutive behaviour material model to study the size effect phenomenon for a strain rate dependent material via ABAQUS[®]/EXPLICIT user subroutine VUMAT was proposed. The modified JC model takes into account the strain gradient-based approach [XIN08] by including the effects of strain gradient which is known to be an important factor affecting the material strength during micro-cutting.
- Introduction of a hybrid scale dynamic cutting model to investigate the variation of the machining system (tool, tool-holder and spindle) stiffness and damping on the localized chip morphology and surface topology under dynamic cutting conditions.
- Experimental validation of the developed approaches.

Dissertation – At a glance

For clear and comprehensive presentation of the work, manuscript is outlined succinctly in the following, four chapters:

Chapter 1 provides a literature review on the cutting process and the finite element modelling of machining process. Experimental observations and scientific concepts to explain the size effect phenomenon during micro cutting are also presented.

Chapter 2 concisely presents the finite element code ABAQUS[®]/EXPLICIT (Ver. 6.7.1) used for the present work. A new numerical model based on the coupling between material damage evolution and its fracture energy has been proposed. Numerical results concerning chip segmentation, fragmentation and machined surface residual stress distribution for orthogonal turning case are discussed. Also, details concerning experimental procedure in turning have

been provided. The chapter ends with exploitation of the proposed model for the case of orthogonal down-cut milling.

Chapter 3 discusses the material strain rate hardening characteristics and strain gradient as dominating factors in increasing material strength, during micro level cutting for a strain rate dependent material. A modified Johnson-Cook equivalent stress model, including strain gradient, is formulated in ABAQUS[®]/EXPLICIT via its user subroutine VUMAT to study the influence of strain gradient on size effect.

Chapter 4 proposes a methodology to build a finite element based hybrid dynamic cutting model (HDC-model) in order to predict the chip formation process for down-cut milling case.

The manuscript is ended by a general conclusion including the major points outlined in this dissertation and a discussion of possible avenues in future as a continuation of this research work.

1 Literature Review

1.1 Introduction

Metal cutting is one of the most widespread processes in which, by action of a cutting edge of a tool, unnecessary material is removed. It is one of the most common manufacturing processes for producing parts and obtaining specified geometrical dimensions and surface finish. Turning, drilling, and milling are examples of different industrial applications that use this principle with different tool geometries and number of cutting edges.

The understanding of the material removal process in metal cutting is important in selecting tool material, its design and in assuring consistent dimensional accuracy and surface integrity of the finished product. It is well-known among scientific community that modelling task of cutting process is particularly complex due to the diversity of physical phenomena involved, including large elasto-plastic deformation, the ambiguities of contact/friction formulation, the presence of thermo-mechanical coupling and the variability of chip separation mechanisms. One factor that has caused considerable difficulty and frustration to researchers investigating the chip formation is the fact that the phenomena occurring in the vicinity of the cutting edge are highly localized and not directly observable from experimental point of view. After more than a hundred years of research, the study of metal machining still constitutes a current challenging task.

Although the first theoretical models were able to describe the problem only qualitatively, their principles and assumptions laid foundations for further advancements. The main shortcoming of existing solutions for chip formation mechanisms perhaps lies in the oversimplification and consequent disregard of the complex interplay of the different parameters. Numerical simulation by the FEM has proven to be a reliable alternative to analyse precisely several metal forming operations. Thanks to the advent of high-speed computer processors, robust large-strain/large-displacement procedures, contact/fracture algorithms, adaptive re-meshing procedures for inelastic problems and robust finite/discrete

algorithms, etc. that numerical simulations of forming operations, which involve material removal have become possible.

After, describing the basics of milling process, principal of orthogonal cutting and the major deformation zones during chip formation mechanism, this chapter reviews some of the previous researches made on various aspects of the macro/traditional/classical and micro machining. The focus is on the application of FEM to model cutting process and experimental observations of size effect phenomenon. The mechanisms that have been proposed to explain the size effect in micro-machining are also presented.

1.2 Machining of materials by milling

Milling is the complex shaping of metal parts (in comparison to turning process) by removing unneeded material to form the final shape. The milling machine dedicated to this process is a power driven machine and in its fundamental form is comprised of a milling cutter that rotates about the spindle axis and a work table that can move in multiple directions (usually in three-dimensional Cartesian coordinate space). The motion across the surface of the workpiece is accomplished by moving the table on which the workpiece is mounted. In its very basic form milling process can be classified in three major categories (Fig. 1.1).

- i) Peripheral milling or slab milling:** In this case the machined surface is generated by the teeth located on the periphery of the cutter body. The axis of cutter rotation is generally in a plane parallel to the workpiece surface to be machined (this case is studied in the present work)
- ii) Face milling:** The cutter is mounted on a spindle having an axis of rotation perpendicular to the workpiece surface. The milled surface results from the action of cutting edges located on the periphery and face of the cutter.
- iii) End milling:** The cutter rotates on an axis vertical to the workpiece. It can be tilted to the machine tapered surfaces. Cutting teeth are located on both the end face and periphery of cutter body.

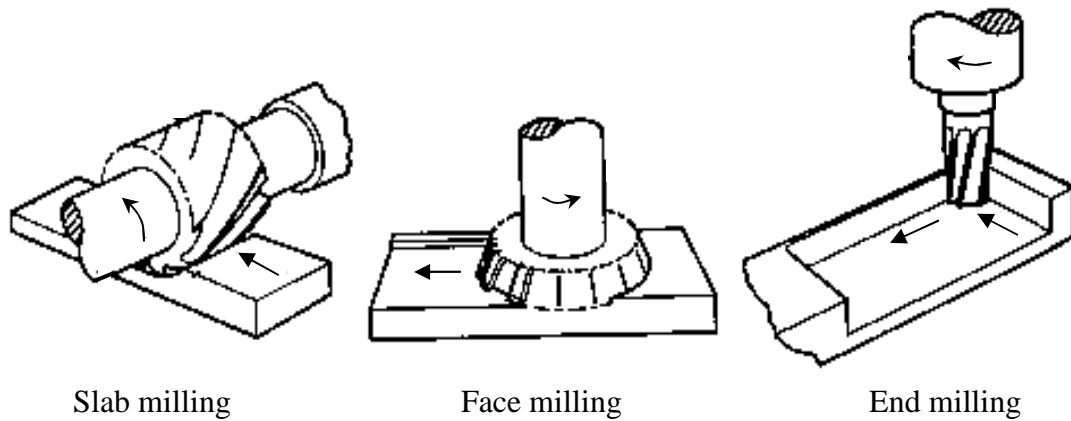


Fig. 1.1 Classification of milling operation [CUS10]

Milling cutting process is usually performed in two modes.

- i) **Climb or down-cut milling:** The direction of cutter rotation is the same as the table feed motion. For example, if the cutter rotates anticlockwise then workpiece is fed from left to right direction as shown in the adjoining Fig. 1.2 (this case is modelled in the present study).

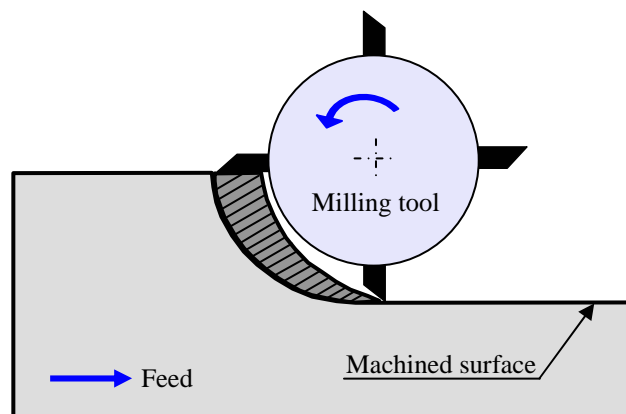


Fig. 1.2 Schematic representation of climb or down-cut milling

- ii) **Conventional or up-cut milling:** The direction of the cutter rotation opposes the feed motion. For example, if the cutter rotates clockwise then workpiece is fed from left to right direction as shown in the Fig. 1.3.

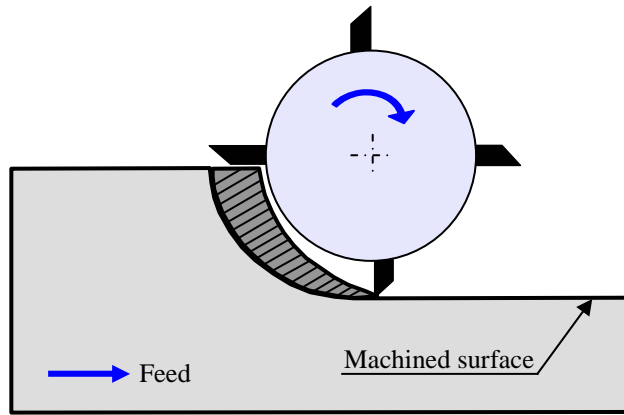


Fig. 1.3 Schematic representation of conventional or up-cut milling

1.3 Principal of orthogonal cutting

Most of the industrial applications that remove material by machining operations use complex insert geometries with various chip breakage. To avoid this complexity when modelling cutting process, usually two dimensional plane strain assumptions are proposed. The elaborated cutting models are known as orthogonal cutting ones. They permit a 2D cutting simulation, supposing a unit depth of workpiece. In these conditions the tool cutting edge is simultaneously orthogonal to the cutting velocity and the feed velocity as shown in Fig. 1.4. In general case, the orthogonal cutting corresponds to a given insert with an edge inclination and entering angles equal to 0° and 90° , respectively.

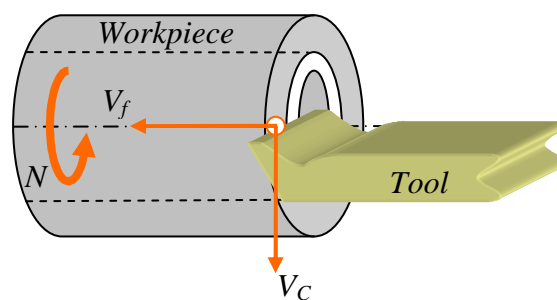


Fig. 1.4 Schematic representation of orthogonal cutting

1.4 Chip formation

It is accompanied by complex phenomena and its morphology is mainly affected by the thermo-mechanical characteristics of the material to be machined, tool material grade and its

geometry, cutting speed, feed rate, type of the cutting fluid and machine dynamic behaviour. Carrying out experimental studies like measuring of cutting forces, metallographic chip investigations, chip micro-cinematographic visualisations, quick-stop method, etc. allow to investigate some interesting phenomena of mechanical, tribological and surface engineering aspects. Despite, some experimental difficulties met during these studies the following cutting zones have been found during tool-workpiece interaction (Fig. 1.5).

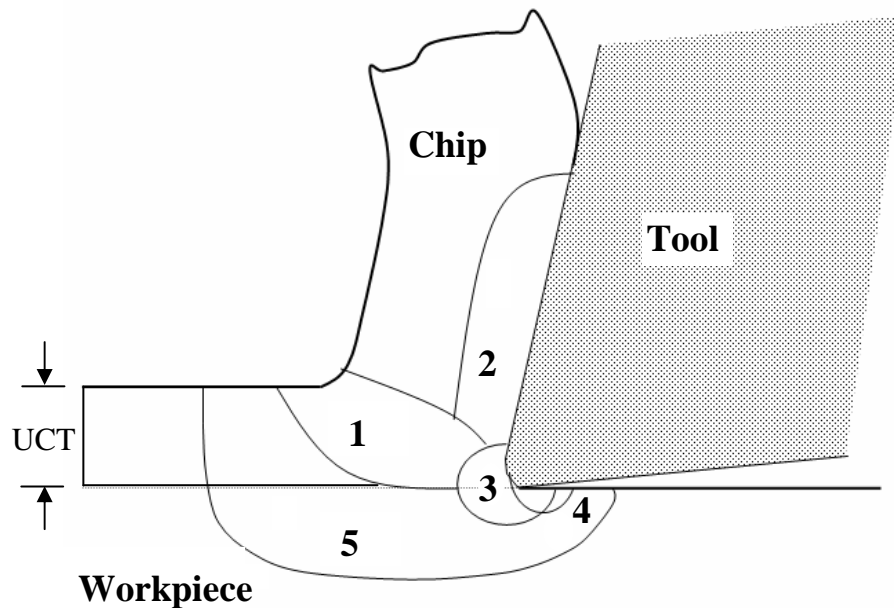


Fig. 1.5 Principal affected zones in chip formation

- **Zone 1:** Primary shear zone. It results by change of direction of the material. This zone undergoes sudden deformation by shear. In addition to high strain rates, there generates a strong rise in temperature by plastic work.
- **Zone 2:** Secondary shear zone. It is induced by friction on insert rake face. This zone is simultaneously subjected to high strain rates and strong rise in temperature due to dissipation of heat by friction.
- **Zone 3:** Separation zone of the workpiece. It is characterised by an intense deformation due to tool compression. The latter also provokes elastic and plastic deformations which, by means of “spring back”, induce residual stresses on the surface of the machined workpiece.
- **Zone 4:** In this zone machined surface is solicited by the insert clearance face which is affected by wear phenomenon due to friction.
- **Zone 5:** This is the zone limiting the workpiece deformation during the tool-workpiece interaction.

In each of these zones, different thermo-physical and chemical phenomena like adhesion, welding, diffusion, chemical transformation, etc. can occur. This induces metallurgical structure transformation mainly due to mechanical loadings and rise in temperature.

For the case of micro cutting the small depth of cut, due to the small feed rate and edge radius of the tool causes a large negative rake angle (Fig. 1.6). Consequently chips are formed by shearing of the workpiece [CHA06]. The friction between the tool and the workpiece increases resulting in thermal growth and a pronounced tool wear rate [XIA03]. The later can lead to undesirable burr formation [WEU01, HIG08]. Micro chip formation causes ploughing, a rough machined surface and an elastic recovery of the workpiece [KIM04b, LIU04b].

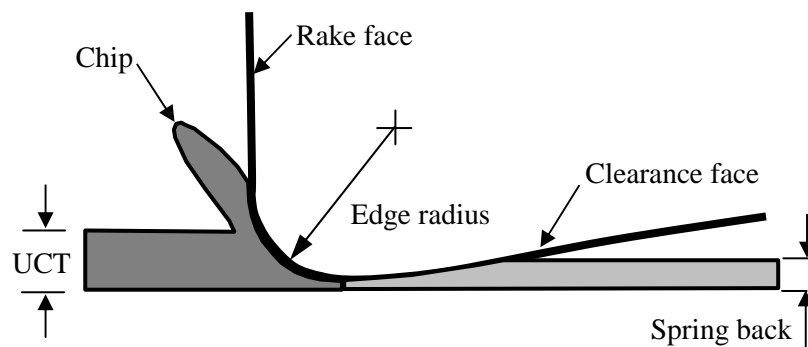


Fig. 1.6 Chip formation during micro cutting.

1.5 Finite element modelling of macro/traditional machining process

The first analytical model that laid the framework for modelling of orthogonal machining processes was proposed by Merchant [MER44] in 1944. With the invention of the computer and the rapid growth in computing power, finite element techniques have been widely used by many investigators. We cite here non-exhaustive references [OBI97, MAM01, BÄK05] with notable success in modelling the machining process. All these authors have used different numerical methods for calculations. Nevertheless, whatever methods are adopted there are some core particularities associated with the finite element simulation of cutting process e. g:

- movement description ,
- constitutive material models and chip separation techniques,
- heat generation and thermal assumption,
- tool-chip interface characterisation,
- etc.....

1.5.1 Approaches and movement description

Among literature, to simulate machining processes, two common methods for movement description are adopted: Eulerian and Lagrangian formulations.

In the Eulerian formulation (Fig. 1.7a), the finite element grid through which the material flows is fixed in space. The advantage of this formulation is that the shapes of the elements do not change with time. So, the element distortion does not take place. This implies numerically the possibility to make assumptions of high values of friction coefficients at tool-workpiece interface. However, an initial shape of the free surface of the chip has to be assumed and chip formation process cannot be modelled hence chip morphologies are not comparable to the experimental ones.

The Lagrangian method (Fig. 1.7b) involves a moving frame of reference. The mesh is attached to the material and moves along with the material. However, the elements change shape during the material flow and in extreme cases it may become necessary to control the distorted elements. Therefore, re-meshing or adaptive-meshing is often required for these types of formulations [XIE94]. In addition, a chip separation criterion needs to be specified to simulate chip formation [BÄK02, BAR05, MAB06].

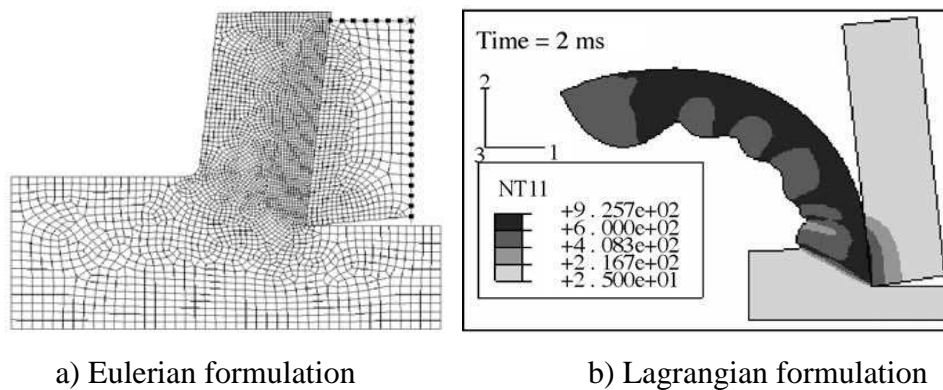


Fig. 1.7 Orthogonal chip formation [HAG08, MAB06]

Although the Eulerian approach possesses the advantage of no element distortion and can avoid many instabilities which can be met in Lagrangian one, but it can only be used for steady-state analysis and can not efficiently model the real chip morphology. Nevertheless, with recent advances in hardware and software, a global formulation taking into account in the same time the nature of both pure Lagrangian and Eulerian formulations was elaborated and so-called ALE (Arbitrary Lagrangian-Eulerian) movement description. The latter formulation is used by many researchers [CER98, ÖZE00, LIU04a] and is incorporated in

various commercially available software packages such as (ABAQUS, DEFORM, LS-DYNA, NIKE2, MARC, etc.) for modelling material removal processes.

In an ALE-formulation, the mesh points move but not necessarily with the material (Fig. 1.8). While the finite element mesh spans the complete analysis domain throughout the solution and its boundaries move with the movements of free surfaces and structural boundaries, the material moves relative to the mesh points. This approach is suitable for modelling large deformation processes, general free surfaces and interactions between fluid flows and structures. When ALE method is adopted, three criteria must be formulated:

- remeshing criterion, in order to determine new node coordinates,
- material flow among boundary elements which is calculated by convective forces,
- conversion of internal variables must be carried out after remeshing, from old mesh to the new one.

To obtain physical results, high adaptive meshing frequency is required. Latter makes this approach a time-costly technique.

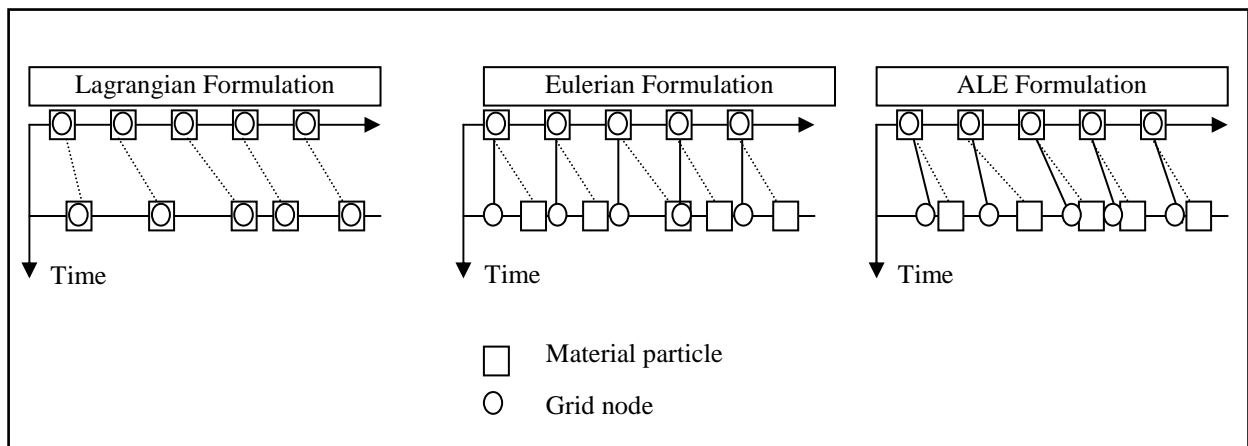


Fig. 1.8 Movement description in Lagrangian, Eulerian and ALE formulations

1.5.2 Constitutive material models and chip separation techniques

FE simulations for machining are greatly influenced by the flow stress characteristics of the material in different cutting regimes. It is well-known that the flow stress of the material is a function of the strain, strain rate and temperature.

Various numerical studies have been performed using a wide range of constitutive models for the workpiece, such as rigid-plastic, rigid-viscoplastic, elasto-perfectly-plastic, elasto-plastic

and elasto-viscoplastic. Elastic-to-plastic materials have been the most commonly used in simulations, with the plastic strain-rate dependency being included in some studies [LIN92, YAN02]. The elasto-viscoplastic model has been frequently adopted by other authors such as Shih and co-workers [SHI90]. Some researchers, aiming at simplifying the analysis, have used rigid-plastic [IWA84, CER99] and rigid-viscoplastic materials [SEK93, KOU02, UMB04]. One of the most popular material formulation (elasto-thermo-visco-plastic) adopted in the present study is that proposed by Johnson and Cook [JOH85]. Several modelling studies have shown the effectiveness of this material flow stress model [RAM02, GUO04, JIN04].

A critical aspect which can be evoked during FE based simulation (for Lagrangian and ALE formulations) of the cutting process is the specification of the technique as chip separation criteria which can be classified in following three categories:

- Node separation technique is a geometry-based approach [PAR96, HAS99, GUO00]. A predefined parting line is used to separate the chip layer from the workpiece. At each point on the parting line, two nodes are tied together initially and share the same degrees of freedom. When the tool approaches the tied pair of nodes, they separate when a pre-specified criterion is met. Other commonly used criterion is the tool node distance, critical effective stress, and critical effective plastic strain.
- Element deletion technique [RAM02] is also a geometry-based approach in which the chip layer is predetermined by a sacrificial element layer positioned at the bottom of the chip layer. When the tool approaches a sacrificial element, it will be deleted based on a criterion such as critical effective plastic strain or critical energy density.
- Using of fracture to determine chip separation is controversial since there is no consensus in the literature on whether chip formation indeed occurs by fracture or not [SHA84, SCH00]. However, this technique is also being used by many researchers giving promising results [BAR05, BEL05, MAB06]. Recently, Subbiah and Melkote [SUB08] have shown experimentally based on quick-stop test that the chip separation is occurred by fracture in the tool edge vicinity when machining A2024.

1.5.3 Heat generation and thermal assumption

Another important feature of finite element based cutting simulation is the consideration of heat generation due to simultaneous phenomena of inelastic deformation and friction. This in turn changes the material properties. Therefore, thermo-mechanical modelling is required to obtain stress, strain and temperature solutions simultaneously as the material is being cut. So, coupled temperature-displacement analysis is usually performed.

Nevertheless, some studies have generated physical results with adiabatic hypothesis [KAL97, MAB06, WEN06]. The solution of the field equation for the heat conduction is not required when this assumption is made, but this approximation can only be safely adopted for low diffusivity materials or in high-speed processes. The temperature increase is calculated directly at the material integration points according to the adiabatic thermal energy balance. If the cooling to room temperature is needed in order to evaluate residual stresses of the workpiece, it is not advisable to adopt this simplification [VAZ07]. If such numerical model assumes that the conditions are adiabatic at a given cutting speed, this is probably not true. It should either perform a calculation with heat conduction to check the adiabatic assumption or it should be judicious to use the criterion developed by Recht [REC64] or that given by Frost and Ashby [FRO82] to see whether conditions are in fact adiabatic.

Certainly, for specific cutting parameters both inelastic heating and conduction of the heat are important. So, a coupled temperature displacement analysis must be performed. Therefore, in the present work, coupled temperature-displacement analysis has been carried-out. The heat transfer modelling formulation adopted in the present study is detailed in next chapter.

1.5.4 Tool - chip interface

The friction characteristic at the tool-chip interface is difficult to determine since it is influenced by many factors such as local cutting speed, local contact pressure, temperature, tool and workpiece material, etc [REC09]. It influences the chip geometry, built-up edge formation, cutting temperature and tool wear. Therefore it is necessary to understand the friction mechanism across the faces and around the edge of the tool, in order to be able to develop accurate model(s) for cutting forces and temperature.

The most simple friction model is Coulomb friction. Usually the friction coefficient μ is assumed to be constant for a given interface. However, extensive studies have been performed on the mechanics of interaction along the tool-chip interface and several models that are more relevant for the cutting process where rate, pressure and temperature dependency are

accounted for have been developed. Among them, Zorev's stick–slip friction model [ZOR63] has been one of the most commonly used to present frictional contact between chip and tool. Zorev advocated the existence of two distinct tool-chip contact regions: near the tool tip, where shear stresses τ_f are assumed to be equal to the shear strength of the material being machined τ_Y , whereas, in the sliding/slip region, the frictional stress is proportional to the normal stress σ_n

$$\tau_f = \begin{cases} \tau_Y, 0 \leq l_r \leq l_c (\mu \sigma_n \geq \tau_Y) \rightarrow \text{stick} \\ \mu \sigma_n, l_r > l_c (\mu \sigma_n < \tau_Y) \rightarrow \text{slide} \end{cases} \quad (1.1)$$

Where τ_Y is defined as $\tau_Y = \frac{\sigma_y}{\sqrt{3}}$; σ_y is the approximated uniaxial (or equivalent) flow stress of the material, μ is commonly associated with the Coulomb's friction coefficient and l_c is the transitional zone, assumed to be known in advance in most cases (Fig. 1.9).

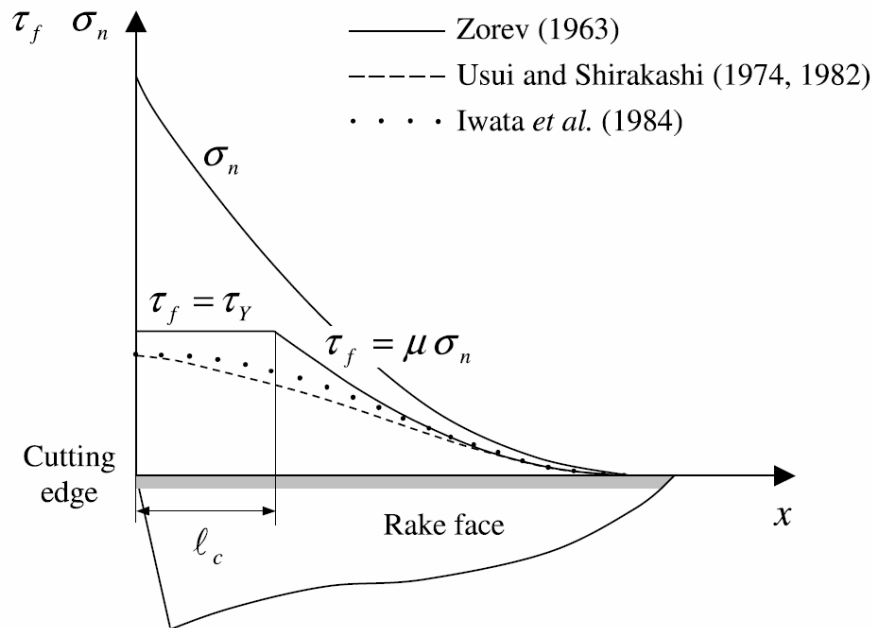


Fig. 1.9 Frictional and normal stress along the rake face [VAZ07]

Similar approaches have been applied to simulate machining processes, such as defining an average friction coefficient over the rake face, separate coefficients for each region, different lengths for the sticking region, or even neglecting altogether the low stress variation of shear and normal stresses and simply assuming $\tau_f = m\tau_Y$ ($m < 1$) along the rake face [SHI90, GUO02, EE05]. Experimental models were introduced by Usui and co-workers [USU82, OBI96,

OHB05], who used a non-linear stress expression to relate the normal stress and frictional stress as:

$$\tau_f = \tau_Y \left[1 - \exp\left(-\frac{\mu\sigma_n}{\tau_Y}\right) \right] \quad (1.2)$$

Where μ is a tool-chip material constant and τ_Y is the maximum shear stress of the chip surface layer in contact with the rake face of the tool. Eq. 1.2 approaches $\tau_f = \tau_Y$ for large normal stresses (sticking region) and the classical Coulomb's law, $\tau_f = \mu\sigma_n$ for smaller values of σ_n (sliding region), as illustrated by the dashed line shown in Fig. 1.9. Childs and co-workers [CHI00, DIR01] introduced further modifications in (Eq. 1.2) as follows:

$$\tau_f = m\tau_Y \left[1 - \exp\left(-\frac{\mu\sigma_n}{m\tau_Y}\right)^n \right]^{1/n} \quad (1.3)$$

In their proposed model (Eq. 1.3) the exponent n controls the transition from the sticking to the sliding region and the coefficient m accounts for a lubrication effect. Özel [ÖZE06], by comparing experimental results with several friction models based on (Eqs. 1.1 and 1.2) and (Eq. 1.3), concluded that predictions are more accurate when utilising friction models established from the measured normal and frictional stresses on the tool rake face and when implemented as variable friction models at the tool-chip contact in the FE simulations. Based on the experiment where a bar-shaped tool slides over the inner surface of a ring specimen, Iwata et al. [IWA84] proposed an expression for frictional stress dependence on Coulomb's friction coefficient, normal stress and Vickers hardness of the workpiece material, H_v as:

$$\tau_f = m\tau_Y \tanh\left(\frac{\mu\sigma_n}{m\tau_Y}\right) \quad (1.4)$$

where, $m\tau_Y = \frac{H_v}{0.07}$.

Which was later approximated using the shear flow stress to guarantee that $\tau_f < \tau_Y$ in the elements immediately in contact with the rake face. Noticeably, (Eq. 1.4) yields a close approximation of Usui's friction model [SHI74, USU82] when defining $H_v/0.07$ tending to $m\tau_Y$, as illustrated by the dotted line depicted in Fig. 1.9.

Despite the importance of friction in machining simulation, most authors agree that the existing models present limitations and further experimental–numerical efforts are required to describe interaction between tool and workpiece.

In the present numerical simulation work we do not intend to develop a new frictional model but we will exploit a previous model such as the most widely used Zorev's [ZOR63] friction one which is also known as an extended coulomb's law. By referring to the work [NI06] an average friction coefficient equals to 0.17 has been used in our models.

1.6 Micro machining and size effect phenomenon

Micro-cutting is characterized by very small amounts of material removal with UCT values varying from a few microns (or less) to several hundred microns. Besides, it had been seen that at typical length scales, even in macro-to-micro level cutting (e.g. in down milling process), the UCT becomes comparable to the size of crystal grains. At these length scales, the size effect phenomenon is expected to be dominant. In machining, the size effect is typically characterized by a non-linear increase in the SCE as the UCT is decreased.

It has also been reported in micro- and nano-indentation tests, where remarkable material strengthening behaviour has been observed [STE93]. Experimental observations of size effect in machining of different materials under various cutting conditions have been reported in the literature. Backer and Shaw [BAC52] have accounted the increase to the SCE in orthogonal turning tests performed on SAE 1112 steel (Fig. 1.10) to the size effect. Their tests were performed on a $\varnothing 57.2$ mm bar pre-machined in the form of a thin-walled tube having a wall thickness of 5 mm. The used insert was a carbide tool with 0° rake and 5° clearance angles. Cutting tests were conducted at a cutting speed of 137.16 m/min with UCT ranging from 294.6 μm to 58.4 μm .

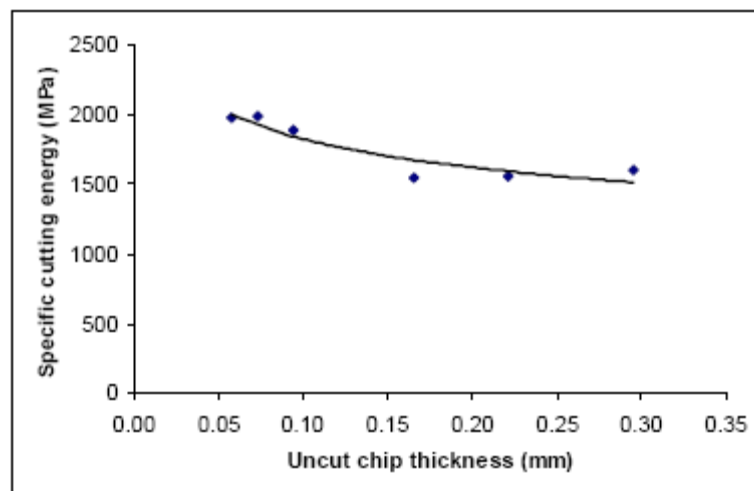


Fig. 1.10 Specific cutting energy vs uncut chip thickness [BAC52]

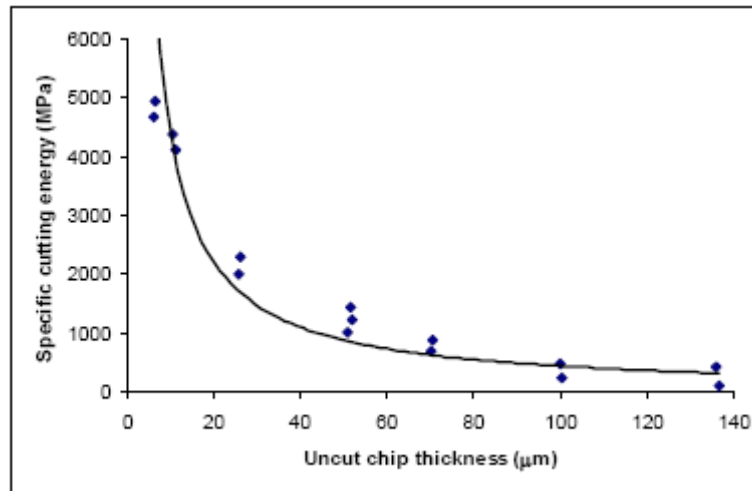


Fig. 1.11 Specific cutting energy vs uncut chip thickness [KOP84]

Kopalinsky and Oxley [KOP84] conducted turning tests on plain carbon steel (0.48% C, 0.3% Si, 0.13% S, 0.8% Mn and 0.019% P) with a cutting speed of 420 m/min. The cutting tool used was a black ceramic indexable tip with -5° rake and 2° clearance angles. The cutting edge radius of the tool was ground by a fine grit diamond wheel to a radius smaller than $6\ \mu\text{m}$, which was also the smallest value of UCT used in their tests. Their results, reproduced in Fig. 1.11, show a clear nonlinear scaling effect in the SCE with decrease in uncut chip thickness.

Nakayama and Tamura [NAK67] performed an experimental investigation on orthogonal cutting of brass. The cutting speed was kept at 0.1 m/min in all their tests in the aim to avoid thermal and strain rate effects. High speed steel tools with an edge radius of $3\sim 4\ \mu\text{m}$ at different rake angles (0° , -20° , -40°) were used (Fig. 1.12). The size effect detected in the SCE and thrust forces variations is clearly evident at low cutting speed of 0.1 m/min.

Lucca et al. [LUC93] conducted an experimental study of the effect of single crystal diamond tool edge geometry on the resulting cutting and thrust forces and SCE in ultra precision cutting. Edge radii of newly sharpened single crystal diamond tools were measured with an atomic force microscope (AFM) by scanning the AFM's cantilever tip across the diamond tool edge normal to the rake and flank faces. Single crystal diamond tools with edge radius of $0.25\ \mu\text{m}$ ($\pm 0.02\ \mu\text{m}$) at different rake angles (0° , -10° , -20° and -30°) were used for cutting Te-Cu, which has a nominal chemical composition of 99.4-99.5% Cu and 0.5-0.6% Te. The experiments were conducted at a cutting speed of 7.6 m/min with the UCT ranging from $20\ \mu\text{m}$ down to 10 nm. Their results demonstrate also the importance of size effect when dealing with SCE (Fig. 1.13).

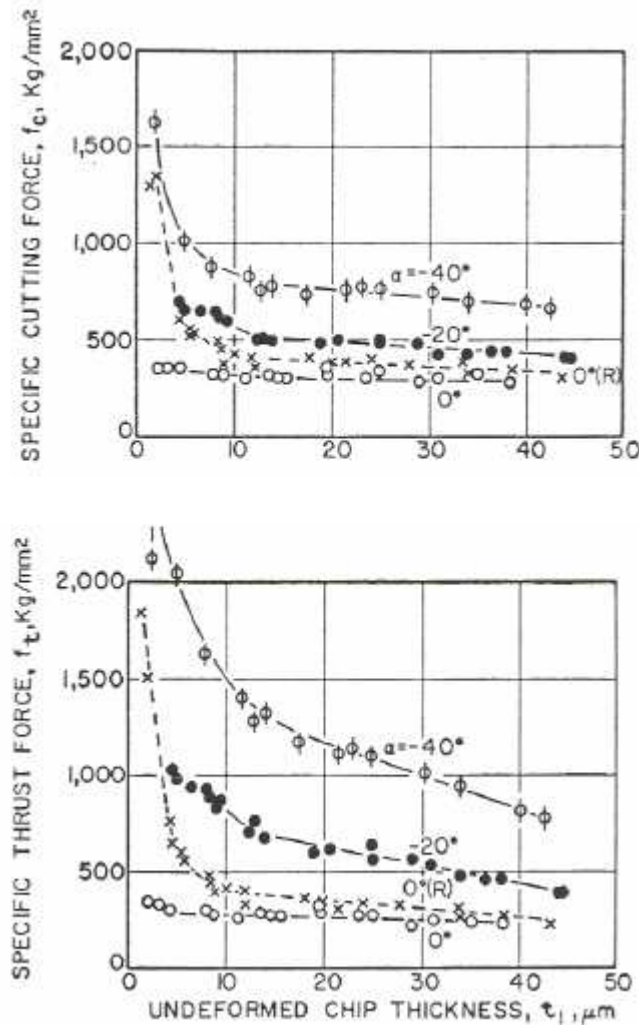


Fig. 1.12 Specific cutting energy vs uncut chip thickness [NAK67]

Furukawa et al. [FUR88] had also reported the presence of size effect in the SCE (Fig. 1.14) over an UCT ranging from 0.5 to 10 μm in their investigation of micro-cutting of several different materials. Later have diversified properties including Aluminium alloy, Oxygen Free Copper (OFC), Germanium (difficult to finish precisely because of its high hardness and brittleness), Fluorite (a single crystal used for ultraviolet ray components, and is not very hard but is very brittle, CaF_2) and Acryl resin (PMMA, a soft amorphous material used for optical components) etc. A single crystal diamond tool with 0° rake and $2\sim 3^\circ$ clearance angles was used at a cutting speed of 6 m/min.

Schimmel and Endres [SCH02] and Kountanya [KOU02] investigated the effect of the variation of tool edge radius on cutting forces in orthogonal cutting case. Experiments were performed on materials such as pure zinc, cast iron and Al-2024 at a cutting speed of 56.4

m/min, with carbide tools having edge radii ranging from a few microns to a few hundred microns. Fig. 1.15 reproduces their results and the nonlinear scaling effect can be seen.

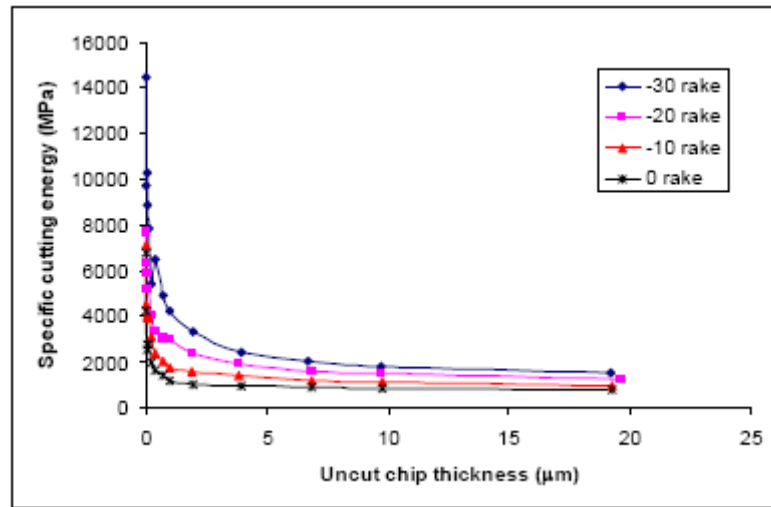


Fig. 1.13 Specific cutting energy vs UCT for various rake angles [LUC93]

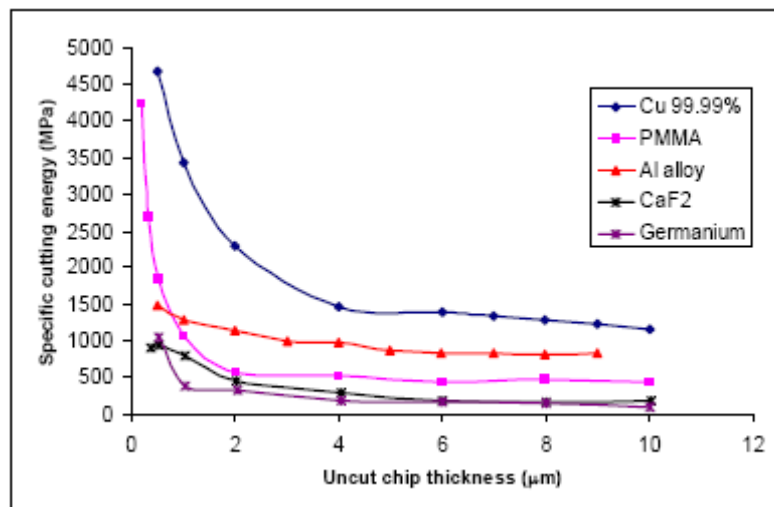


Fig. 1.14 Specific cutting energy vs UCT for various cut material [FUR88]

Various researches have shown that the size effect can even arise while cutting with sharp tools [LUC93] and when the effects of temperature and strain rate are negligible (i.e. at very low cutting speeds) [NAK67].

Backer et al. [BAC52] attributed the size effect to crystallographic defects such as grain boundaries, missing and impurity atoms, etc. They argued that since a significantly reduced number of imperfections are encountered when deformation takes place in a small volume. The material strength would be expected to increase and approach the theoretical strength.

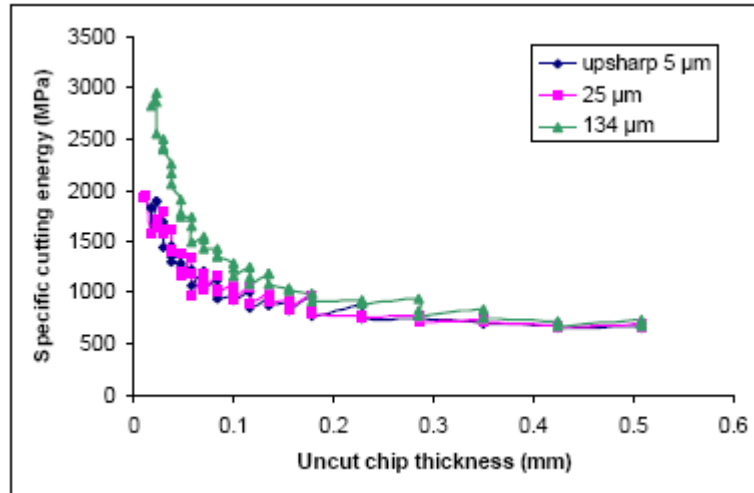


Fig. 1.15 Specific cutting energy vs UCT for various tool tip radius [KOU02]

Larsen-Basse and Oxley [LAR73] explained the scaling phenomenon in machining in terms of the strain-rate sensitivity of the workpiece material. Their reasoning is based on empirical data drawn from experiments when machining plain carbon steel. They suggest that the maximum shear strain rate within the primary shear zone is inversely proportional to the UCT. Therefore, a decrease in the latter will leave the strain occurring in the shear zone unchanged but the strain rate will increase inversely with it. For most metals, an increase in the strain rate causes an increase in the flow stress with the strain-rate sensitivity of flow stress increasing rapidly in the range applicable to machining processes. This could therefore explain the increase in SCE with reduction in UCT.

Kopalinsky and Oxley [KOP84] attributed the size effect in the SCE to a decrease in the shear plane angle; due to decrease in the tool-chip interface temperature. Their prescribed approach, leads to an increase in the shear strength of the workpiece material.

Recent work by Atkins [ATK03] attributes the size effect in cutting to the energy required for new surface creation via ductile fracture. The author found that the work associated with separation criteria in finite element models is close to the typical value of fracture toughness for the material in ductile fracture mechanics. He suggested that the energy required for the formation of new surface should not be considered negligible in metal cutting analysis. Its contribution to the overall SCE should increase at small UCT values.

Fang [FAN03] has presented a complex slip-line model for orthogonal machining and attributed the size effect to the material constitutive behaviour of varying shear flow stress with UCT. Nakayama and Tamura [NAK67] analyzed size effect in machining through micro cutting experiments performed at a very low cutting speed (0.1 m/min) to minimize

temperature and strain rate effects. They observed plastic flow in the subsurface layer of the workpiece and suggested that its contribution to size effect becomes important with reduction in the UCT. The main cause of this subsurface plastic flow is believed to be the extension of the shear zone below the machined surface. Therefore, they have attributed the size effect to the fact that the energy consumed in plastic flow in the subsurface layer is proportional to the UCT and to the decrease in shear angle with a decrease in UCT.

It has been argued by many researchers that this size dependent strengthening cannot be explained by the classical continuum plasticity theory. Based on the notion of geometrically necessary dislocations (GND) in dislocation mechanics, strain gradient (SG) plasticity theories have been proposed. Fleck and Hutchinson [FLE93, FLE94], Gao and Huang [GAO99], Acharya and Bassani [ACH00] had introduced the SG dependence of flow stress into the material constitutive model.

Simultaneously, numerous researches have been attributed to develop finite element models on this subject in the last decade. Chuzhoy et al. [CHU02] developed a finite element model for the orthogonal cutting of ductile iron taking into account the various phases of iron. This was the first attempt of finite element modelling at the microstructure level to account for the heterogeneity of the workpiece material.

Though the presented literature review on the topics of micro cutting and size effect strengthening is not exhaustive, however it can be deduced that the size effect in micro-cutting may arise due to multiple mechanisms.

1.7 Conclusions

To bring more physical comprehension of chip formation process with the ultimate aim of improving machining efficiency, various numerical models had been proposed by researchers. FEM is one of the most common numerical modelling techniques being used for this purpose. Thanks to the advent of high-speed computers, robust large-strain/large-displacement procedures, contact/fracture algorithms for inelastic problems and robust finite/discrete algorithms etc. cutting simulations have shown cost effective reliable results.

Though there are some issues related to model this multiphysical phenomenon, for example large elasto-plastic deformation, complex contact/friction conditions, thermo-mechanical coupling, chip separation mechanisms, size effect (in micro machining), etc. Nevertheless, once established, a robust numerical model of machining operations constitutes a useful tool for the prediction of the workpiece machining with cutting tool, optimum cutting parameters

and tool design etc. Consequently, a subsequent reduction in extensive and costly cutting experimentation can be achieved.

In the continuation to improve the comprehension of the physical phenomena of micro level chip formation process, the present study proposes a finite element model for down-cut milling process of a strain rate dependent Aluminium alloy Al204-T351. In the latter process the chip thickness approaches from macro to micro level dimensions because of the trochoidal motion of milling tool. Furthermore, to incorporate the SG plasticity effects in the existing material model (Johnson-Cook equivalent stress model, used for the present study) to efficiently capture the size effect for micro cutting operation ABAQUS[®]/EXPLICIT, a user subroutine VUMAT has been written. Moreover, a finite element (FE) based hybrid dynamic cutting model (HDC-model), to improve the comprehension of chip formation under dynamic cutting conditions has been established. The model(s) details are presented in the following chapters.

2 Dry Machining Modelling of an Aluminium Alloy at Mesoscopic Scale

2.1 Introduction

After presenting a non-exhaustive literature review that can help the reader to get a global idea on FE modelling of machining operation, the present chapter proposes our methodology to build a FE model for dry machining of an Aluminium alloy in the case of orthogonal turning and peripheral down-cut milling. For this introductory section a brief review on the dry cutting is proposed.

Today, in the automotive and aeronautic industries, there is great demand of low-density materials, which can bear high load increase. Aluminium alloys with a wide range of properties is one example of its use in engineering structures. These materials are often subjected to machining operations where the criterion of minimization of lubricant use makes its importance; as more than 16% of the manufacturing cost can be attributed to the coolants [NOU03]. Consequently, it is interesting for researchers to develop green manufacturing processes like dry high-speed machining [NIC02, SRE00]. Nonetheless, for dry machining like the cutting of Aluminium alloys, working parameters have not yet been optimized. Currently, a high value of cutting force is recorded due to an adhesive interaction between the cutting tool and the workpiece (tendency of built-up edge formation or other physiochemical phenomena that can occur at high temperature). Different approaches had been proposed by many researchers to have a better control of Aluminium alloy machining. For example, the effects of the insert coating adhesion on workpiece and the reduction of built-up edge formation have been studied [HOV06]. Similarly, parametric investigations have been performed to find the optimal working parameters for a given tool–Aluminium alloy combination [LIS05]. A valuable experimental home database is now available. However, it has limited use exploitation as it depends on the machine power, the torque limitation, the

insert wear, etc. The latter is one factor among others, which can decrease the production cost. To avoid that, tool wear have been studied by numerous researchers with different methods. For example, the field temperature distributions in the tool during Aluminium alloy machining was estimated [VER02, KAR06a, KAR06b] and the effect of tool edge geometry on the evolution of cutting force has been investigated numerically [FAN05].

In the context of improving the comprehension of physical phenomena accompanying green cutting, the present study develops a FE methodology taking into account the coupling between material damage and its fracture energy evolution for the dry cutting of an aeronautic Aluminium alloy referenced as A2024-T351. This material is widely used for structures under tension, for example fuselages, thin-walled structures, lower wing surfaces, engine baffles, etc. The main objective of the work concerns the presentation of a finite-element-based numerical model for orthogonal cutting. In the proposed model the capabilities of ABAQUS[®]/EXPLICIT software [ABQ07] have been exploited. For experimental investigations, series of tests have been performed in the case of straight turning operations.

In the following, a brief introduction of ABAQUS[®] software and its explicit dynamic approach, mesh optimization, tool-workpiece contact methodology, tool-workpiece geometry, material model and finally results concerning orthogonal turning and milling cases are discussed.

2.2 ABAQUS[®] software and its explicit dynamic approach

According to the amount of published papers dealing with simulation of machining which is a high-speed dynamic phenomenon, the FEM based modelling seems to be now somehow yet developed as it provides a pertinent understanding of chip formation mechanism, heat generation in cutting zones, tool-chip frictional characteristics and integrity of machined surfaces. It provides a good understanding of the effect of some physical parameters on temperatures and stress distribution both in the tool and the workpiece. The FEM in its basic form discretizes the actual geometry of the structure into a finite number of elements joined by nodes. In a simple stress–displacement analysis, displacements at nodes are calculated using implicit methods. Once displacement is known, the stresses and strains in each finite element can be determined.

Presently, there are many commercial FE codes that are capable of modelling the machining processes (DEFORM[®] 2D/3D, ABAQUS[®], ANSYS[®] LS-DYNA and Third Wave's AdvantEdge[®], etc). Nevertheless, ABAQUS[®] seems to be more convivial with its graphic user

interface (GUI) and is more flexible than some of the other codes to define user-defined subroutines. Simultaneously, it is equally good to simulate problems of diversified areas like stress/displacement, heat transfer, mass diffusion, coupled analysis, acoustics, soil mechanics, and piezoelectric analyses.

ABAQUS[®] consists of two main analysis products; ABAQUS[®]/STANDARD and ABAQUS[®]/EXPLICIT. The first product solves a wide range of linear and nonlinear problems in the domain of static, dynamic, and thermal response of the components. The second one is suitable for modelling transient dynamic events, such as impact and blast problems, and is very efficient for highly nonlinear problems involving changing contact conditions, such as forming simulations and machining etc. The explicit capabilities of ABAQUS[®] have been exploited as the FE platform for the present research work.

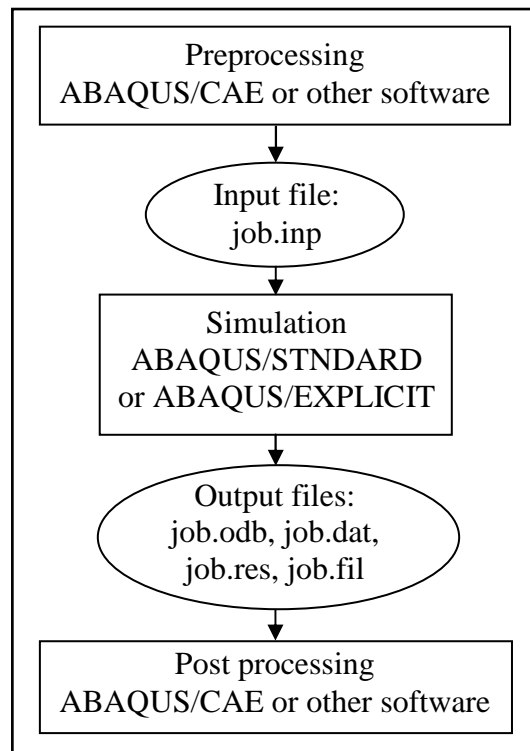


Fig. 2.1 ABAQUS[®] calculation methodology [ABQ07]

ABAQUS[®] provides an interactive graphical environment (ABAQUS[®]/CAE) to create 2D/3D models of the structures to be analysed. It allows to define material properties, boundary conditions, contact model and finally the meshing rules. The file generated in this environment is the “input file” which can be modified for specific purposes. The input file is then submitted to ABAQUS[®]/EXPLICIT solver generating an “output file”, containing the

required results. Finally, these results could be viewed (graphically and numerically) in the postprocessor ABAQUS®/VIEWER. This whole procedure can be represented in the block form, as shown in Fig 2.1.

To simulate high-speed dynamic events, explicit dynamic methods are commonly used. In which time is discretized into a very small number of increments. The explicit dynamic analysis procedure is based upon the implementation of an explicit integration rule together with the use of lumped mass matrix \mathbf{M} . The general equation of motion is:

$$\mathbf{M}\ddot{\mathbf{u}}_n = \mathbf{F}_{\text{ext}} - \mathbf{F}_{\text{int}} \quad (2.1)$$

Where \mathbf{F}_{ext} the externally applied load is vector and \mathbf{F}_{int} is the internal force vector. The equation of motion for the body is integrated using the explicit central-difference rule, where operator satisfies the dynamic equilibrium at the beginning of the increment. The accelerations calculated at time t^i (the superscript i refers to an increment) are computed and are used to advance the velocity solution to time $t + \Delta t/2$ and the displacement solution to time $t + \Delta t$. The central-difference integration operator is explicit in the sense that the kinematic state is advanced using known values of $\dot{\mathbf{u}}_n^{i-1/2}$ and $\ddot{\mathbf{u}}_n^i$ from the previous increment to calculate $\dot{\mathbf{u}}_n^{i+1/2}$.

$$\dot{\mathbf{u}}_n^{i+1/2} = \dot{\mathbf{u}}_n^{i-1/2} + \frac{\Delta t^{i+1} + \Delta t^i}{2} \ddot{\mathbf{u}}_n^i \quad (2.2)$$

On a time step Δt^i , from t^i to t^{i+1} , the central difference scheme gets the solution \mathbf{u}_n^{i+1} from \mathbf{u}_n^i by:

$$\mathbf{u}_n^{i+1} = \mathbf{u}_n^i + \Delta t^{i+1} \dot{\mathbf{u}}_n^{i+1/2} \quad (2.3)$$

Where \mathbf{u}_n^i is a degree of freedom (displacement or rotation component). Time increment Δt is very critical as it defines the stability limit and computational efficiency of the analysis, which finally defines the reliability and accuracy of the result obtained. For a stable simulation, the condition $\Delta t \leq \frac{2}{w_{\text{max}}}$ has to be satisfied, where w_{max} is the maximum natural frequency of the

system and is based on complex set of interacting factors. However, a simple element-by-element estimation can be performed (Eq. 2.4)

$$\Delta t \approx \frac{L_{\text{min}}}{C_d} \quad (2.4)$$

Where L_{\min} is the smallest element dimension in the mesh and C_d is the material dilatational wave speed defined by Eq. 2.5.

$$C_d = \sqrt{\frac{\lambda + \mu}{\rho}} \quad (2.5)$$

Where ρ is the material density. λ and μ are Lamé's constants defined in terms of Young's modulus E , and Poisson's ratio ν .

In ABAQUS[®]/EXPLICIT modal mass, material and mesh size influence time increment. Artificial mass scaling can be assumed for small or poorly shaped elements, which are usually small in numbers. By increasing the mass of these elements, stability limit can be increased significantly, while the overall physics of the system remains the same.

The explicit dynamic procedure performs a large number of small time increments efficiently. The use of small increments (dictated by the stability limit) is advantageous because it allows the solution to proceed without iterations and without requiring tangent stiffness matrices to be formed. It also simplifies the treatment of contact.

2.3 Finite element model for orthogonal turning

2.3.1 Geometrical model and hypothesis

A 2D orthogonal cutting model was conceived in ABAQUS[®]/EXPLICIT (Ver. 6.7.1). Fig. 2.2 shows a schematic representation of the studied model. Quadrilateral continuum elements CPE4RT for both tool and workpiece were used for a coupled temperature–displacement calculation in which both displacements and temperatures are the nodal variables.

It was supposed that the value of feed rate f is lower than that of cutting depth a_p . Consequently, plane strain assumptions for building the cutting model were considered. A contact surface pair (discussed later in section 2.3.2) was defined between the tool and the workpiece. It consists of two surfaces expected to come into contact during the tool–workpiece interaction. These contact surfaces were designated by the master and slave ones, respectively.

ABAQUS[®]/EXPLICIT uses a faceted geometry defined by the FE mesh as the surface definition. To optimize the contact management during simulation, a multi-part model (Fig. 2.2) was developed. It was composed of four parts: (1) the tool, (2) the chip, (3) the tool–tip passage zone, which is a narrower band and (4), the workpiece support. The thickness of the tool–tip passage zone (elements of this zone eventually are deleted; after meeting certain

criteria, to facilitate the chip separation from the workpiece) was assumed to the order of tool edge radius ($R_n = 20 \mu\text{m}$). Subbiah and Melkote [SUB08] have recently shown in their numerical and experimental work on the same material that, the thickness of the tool passage zone should be greater than R_n .

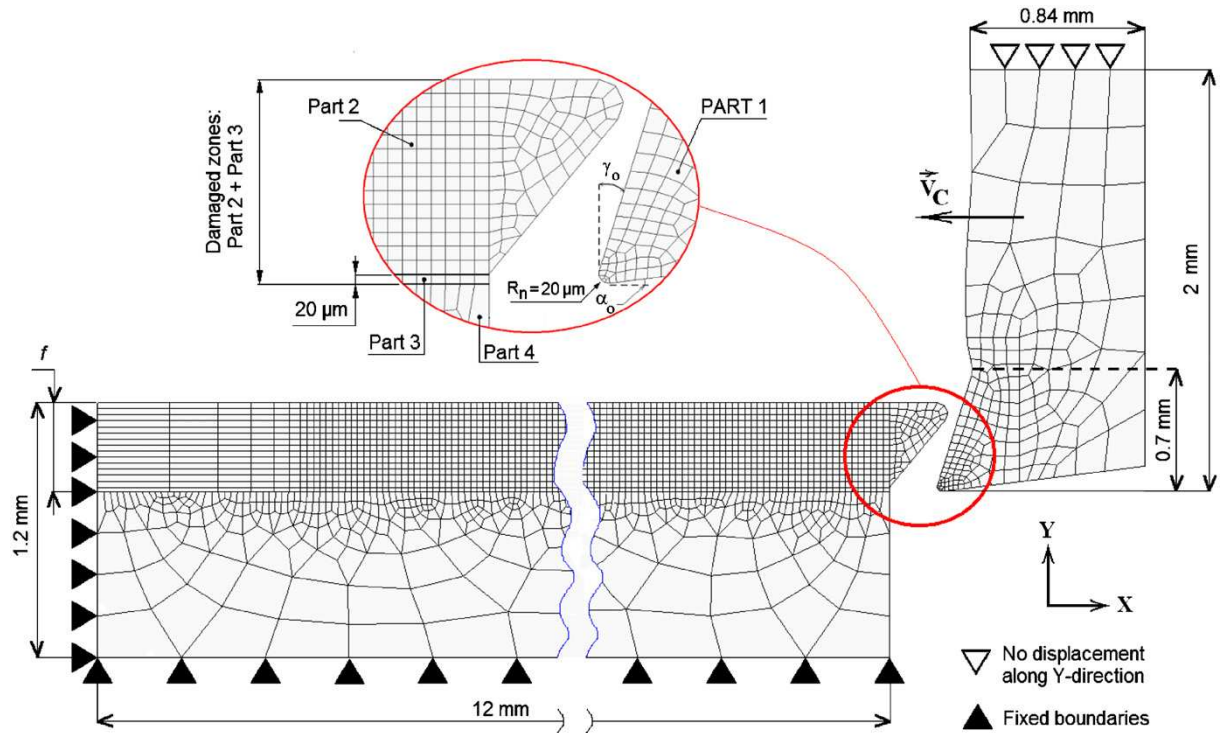


Fig. 2.2 Geometric model and boundary conditions

A chamfer was designed on part 2 to avoid distortion problems at the beginning of calculation. The assembly of the various parts numbered 2–4 was carried out by setting a joint type constraint (Tie constraint). The centre of the tool tip was placed exactly at the middle height of part 3. The tool geometry is exactly the same as that used in experimentation (defined in Fig. 2.10, cross section B–B). The tool face angles are: entering angle 90° , rake angle 17.5° and flank (or clearance) angle 7° . Also, for convenience, it is brought to the reader's attention that in the case of orthogonal cutting conditions, the feed rate f corresponds to the uncut chip thickness (UCT).

2.3.2 Tool - workpiece interactions

During cutting operation, tool comes in contact with the workpiece and also chip can come in contact with itself as shown in Fig. 2.3. Therefore, the management of contact algorithms is

an essential step, among others, to succeed the elaboration of FE cutting model. ABAQUS[®]/EXPLICIT provides two algorithms for modelling contact interactions. The general contact algorithm and the contact pair one. General contact algorithm allows very simple definitions of contact with very few restrictions on the types of surfaces involved. While, contact pair algorithm has more restrictions on the types of surfaces involved and often requires more careful definition to adopt.

Although the general contact algorithm is more powerful and allows defining simple contact definitions, but it must be used in certain cases where more specialized contact features are desired. Some features for example, kinematically enforced contact necessary for self contact (chip with itself) and interactions between 2D surfaces are available only when the contact pair algorithm is used. Therefore, in the present model contact pair algorithm has been used. Interactions definition in ABAQUS[®]/EXPLICIT including, contact surfaces, surface properties, contact properties, and contact formulations are defined during the pre-processing step.

When two surfaces come in contact, contact stresses can be decomposed into normal and tangential components whose ratio gives the frictional coefficient between bodies as shown in Fig. 2.4.

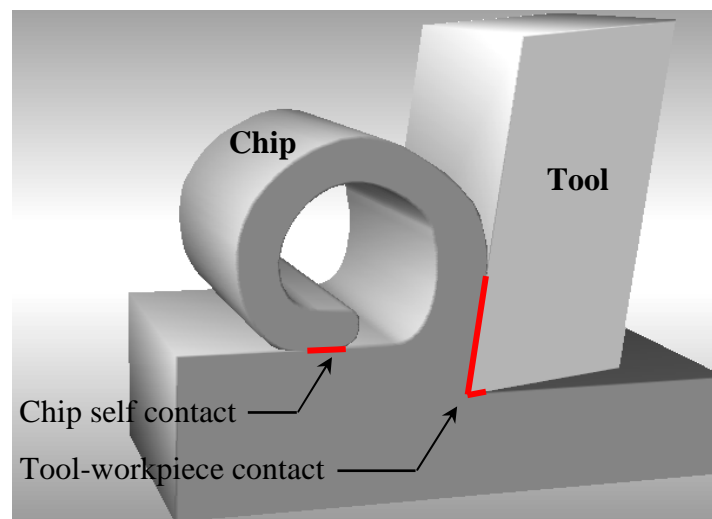


Fig. 2.3 Tool-workpiece interactions

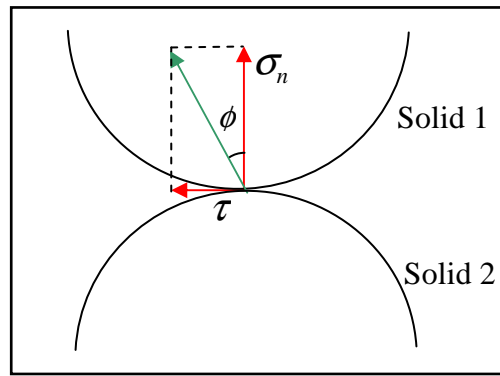


Fig. 2.4 Contact stresses between solids

For the present numerical simulation work, the most widely used Zorev's [ZOR63] friction model also known as extended Coulomb's law is with an average friction coefficient 0.17 [NI06] has been used for tool-chip-workpiece interface.

2.3.3 Meshing

Four node bilinear-quadrilateral continuum elements referenced as CPE4RT in ABAQUS[®] were used for a coupled temperature displacement calculation in which both displacement and temperature are the nodal variables. These elements have also been used by several researchers [MAD00, BÄK02, BÄK03].

CPE4RT are solid elements used for complex nonlinear analysis involving contact, plasticity and large deformations. Nevertheless, these linearly reduced-integration elements under certain loading conditions can experience a pattern of non-physical deformations, called hourglassing. To reduce its effects and to get physical results either a very fine mesh should be defined and/or artificial damping and/or stiffness must be applied. But there is a limit on refining the mesh; as smaller is the element length, smaller will be the time step and analysis will end very costly. Simultaneously, a very fine mesh can lead to strain localisation [BAR05, CAL08]. For CPE4RT elements ABAQUS[®] proposes two types of hourglass treatment approaches:

- the “combined stiffness and damping” method which is based on the combination of stiffness, acting to maintain nominal resistance throughout the simulation, and damping, generating additional resistance under dynamic loading conditions.
- the “relax stiffness” method generating more resistance to hourglass forces early in the analysis step where sudden dynamic is more probable.

Barge et al. [BAR05] have performed a sensitivity analysis for these two approaches according to different mesh densities. They have emphasized on consistent use of hourglass treatment for physical results. They have concluded that “Relax stiffness” is the most efficient method to prevent hourglass modes since its influence on the results is less dependent on the mesh density. For that, the present study therefore incorporates “Relax stiffness” approach to minimize the hourglass.

Whatever is the type of elements, mesh density plays a vital role to get physical results from a FEM based analysis and is usually defined on the nature of the problem. Indeed, coarse mesh is sufficient for steady state elastic problems, while complex plasticity problems leading to damage and crack require the finest mesh to capture localized phenomenon. However, very fine mesh keeps its limitations as it was said previously.

In the literature dealing with FEM cutting simulation, there is no defined criterion for an optimized mesh density. Barge et al. [BAR05] have shown in their numerical work that the coarser the meshes, the higher are the cutting force oscillations. Otherwise, refined meshes lead to a flattened cutting force curve.

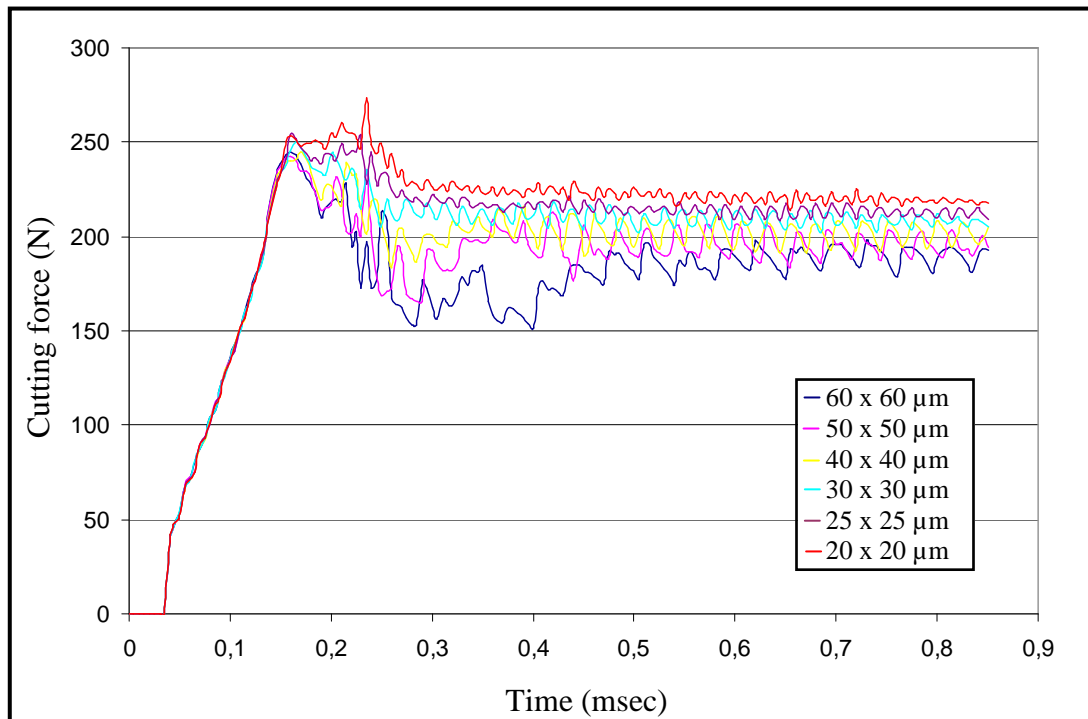


Fig. 2.5 Cutting force plots for various mesh element densities for ($f = 0.4$ mm/rev and $V_C = 100$ m/min).

After their work, a mesh sensitivity test for six different mesh densities has been performed on the geometrical model defined in Fig. 2.2, for $f = 0.4$ mm/rev and $V_C = 100$ m/min. It can be seen in Fig. 2.5 that cutting force curves oscillate for coarse mesh densities (60x60, 50x50 and 40x40 μm). Elements of 30x30 μm size seem to be appropriate for the conceived model (Fig. 2.2), as a further reduction to 25x25 μm and 20x20 μm mesh sizes, don't influence too much on cutting force plot. However, to ascertain that this mesh size is sufficient, average cutting force (averaging of Fig. 2.5 for the time from (0.6 - 0.9 msec) versus the element size was plotted. It is obvious from the Fig. 2.6 that an asymptotic value around 27x27 μm is achieved. This confirms that the opted mesh density (30x30 μm) is sufficient. Further, with this mesh size hourglass energy was found $\approx 3.5\%$ of the total internal energy of the system.

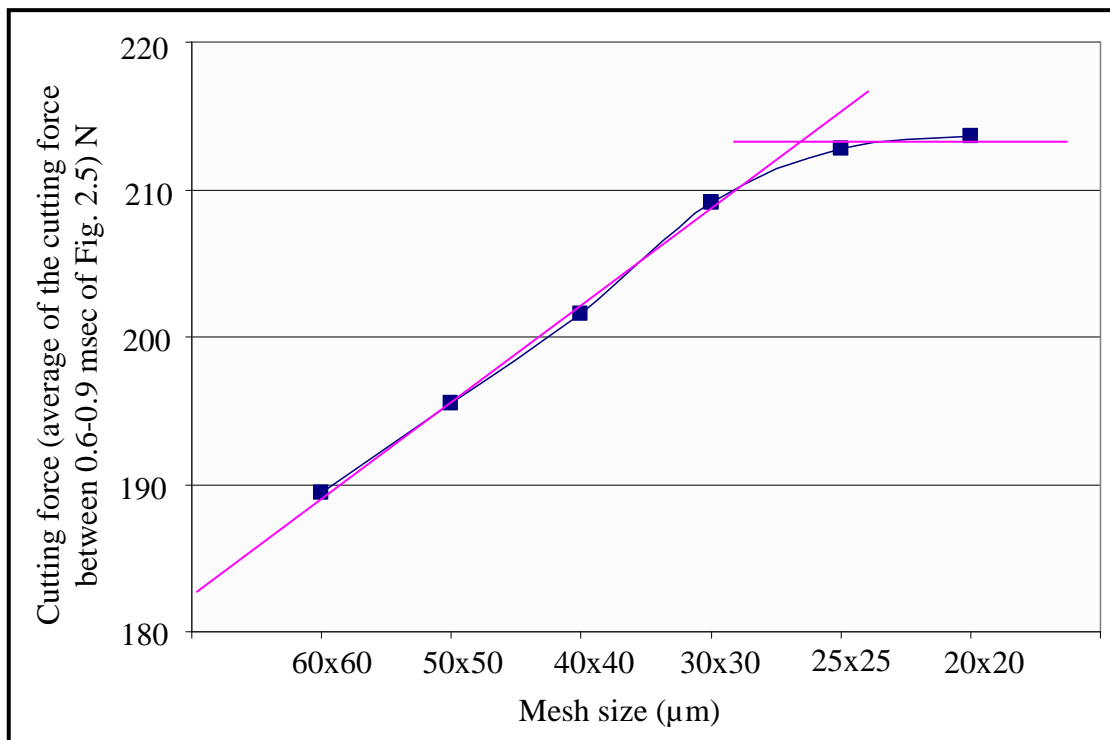


Fig. 2.6 Average cutting force versus mesh element densities for ($f = 0.4$ mm/rev and $V_C = 100$ m/min).

2.3.4 Material behaviour model and chip separation criteria

Johnson and Cook model [JOH85] which provides a good description of metal material behaviour undertaking large strains, high strain-rates and temperature dependent viscoplasticity has been adopted for the present study. This model is presented by the expression of the equivalent flow stress (Eq. 2.6).

$$\bar{\sigma} = \underbrace{(A + B\bar{\epsilon}^n)}_{\text{Elasto-plastic term}} \underbrace{\left[1 + C \ln \left(\frac{\dot{\bar{\epsilon}}}{\dot{\bar{\epsilon}}_0} \right) \right]}_{\text{Viscosity term}} \underbrace{\left[1 - \left(\frac{T - T_{room}}{T_{melt} - T_{room}} \right)^m \right]}_{\text{Softening term}} \quad (2.6)$$

Where $\bar{\sigma}$ is equivalent stress, $\bar{\epsilon}$ equivalent plastic strain, $\dot{\bar{\epsilon}}$ plastic strain rate, $\dot{\bar{\epsilon}}_0$ reference strain rate (10^{-3} s^{-1}), T_{room} room temperature, T_{melt} melting temperature and T is current temperature. A is the initial yield stress, B is the hardening modulus, n is the work-hardening exponent, C is the strain rate dependency coefficient and m is the thermal softening coefficient. The equivalent plastic strain $\bar{\epsilon}$ is determined by von Mises criterion (Eq. 2.7).

$$\bar{\epsilon} = \int_0^t \sqrt{2/3 (\dot{\epsilon}^p : \dot{\epsilon}^p)} \quad (2.7)$$

The Johnson–Cook parameter values adopted to simulate the behaviour of the A2024-T351 workpiece are specified in Table 2.1 [TEN06], whereas the physical properties of the workpiece and the cutting tool are mentioned in Table 2.2 [KNO07].

| A (MPa) | B (MPa) | n | C | m | $D1$ | $D2$ | $D3$ | $D4$ | $D5$ |
|-----------|-----------|------|--------|-----|------|------|------|-------|------|
| 352 | 440 | 0.42 | 0.0083 | 1 | 0.13 | 0.13 | -1.5 | 0.011 | 0 |

Table 2.1 Johnson-Cook parameter used to simulate the behaviour of A2024-T351 [TEN06]

| Physical parameter | Workpiece (A2024T351) | Tool (Tungsten carbide insert) |
|---|---|-----------------------------------|
| Density, ρ (Kg/m^3) | 2700 | 11900 |
| Elastic modulus, E (GPa) | 73 | 534 |
| Poisson's ratio, ν | 0.33 | 0.22 |
| Specific heat, C_p ($\text{Jkg}^{-1}\text{°C}^{-1}$) | $C_p = 0.557 T + 877.6$ | 400 |
| Thermal conductivity, λ ($\text{W m}^{-1}\text{C}^{-1}$) | $25 \leq T \leq 300: \lambda = 0.247T + 114.4$ $300 \leq T \leq T_{melt}: \lambda = -0.125T + 226.0$ | 50 |
| Expansion, α_d ($\mu\text{m.m}^{-1}\text{°C}^{-1}$) | $\alpha_d = 8.910^{-3}T + 22.2$ | × |
| T_{melt} , (°C) | 520 | × |
| T_{room} , (°C) | 25 | 25 |

Table 2.2 Workpiece and tool physical parameters [KNO07]

For chip formation simulation, a failure damage model has been exploited. In order to have an idea on the damage state evolution a typical uniaxial stress–strain response of a ductile metal is illustrated in Fig. 2.7. Indeed, the ductile material response is initially linear elastic (a–b) followed by plastic yielding with strain hardening (b–c). Beyond point c there is a marked reduction of load-carrying capacity until fracture (c–d). The deformation during this last phase is localized in a neck region of the specimen. Point c identifies the material state at the onset of damage, which is referred to as the damage initiation criterion. Beyond this point, the stress–strain response (c–d) is governed by the evolution of the stiffness degradation in the region of strain localization. In the context of damage mechanics, (c–d) can be viewed as the degraded response of the curve (c–d') that the material would have following the absence of damage. The chip formation, by ductile failure phenomenon, occurs in two steps. The first one concerns the damage initiation whereas the second step concerns damage evolution based on the fracture energy approach.

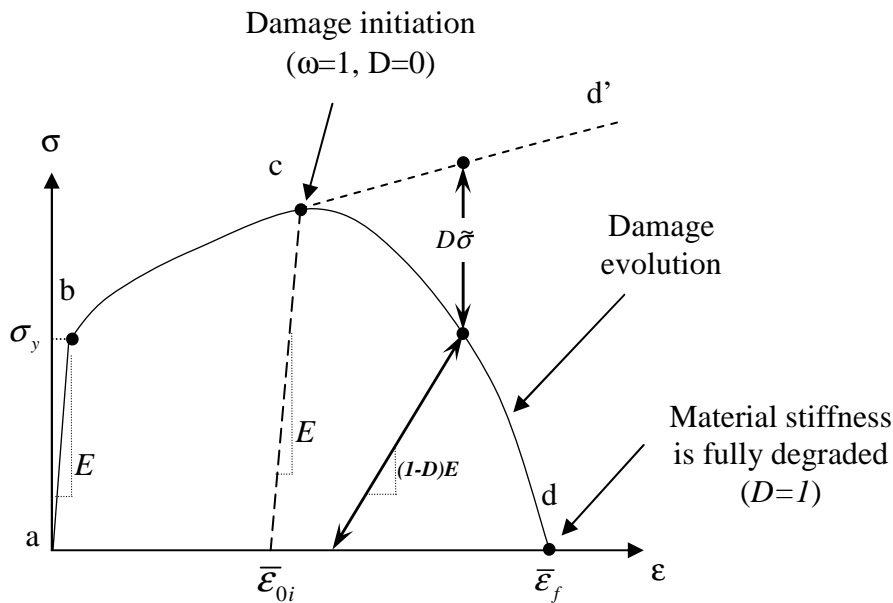


Fig. 2.7 Typical uniaxial stress-strain response of a metal specimen [ABQ07]

1st Step: Damage initiation

The Johnson-Cook shear failure model was used as a damage initiation criterion (Eq. 2.8). This model contains five failure parameters, which must be specified ($D1...D5$). The parameter values of A2024-T351 are given by Table 2.1 [TEN06].

$$\bar{\epsilon}_{0i} = \left[D_1 + D_2 \exp\left(D_3 \frac{P}{\bar{\sigma}}\right) \right] \times \left[1 + D_4 \ln\left(\frac{\dot{\bar{\epsilon}}}{\dot{\bar{\epsilon}}_0}\right) \right] \left[1 + D_5 \left(\frac{T - T_{room}}{T_{melt} - T_{room}}\right) \right] \quad (2.8)$$

In a finite element the damage is initiated when a scalar damage parameter ω exceeds 1. This parameter is based on a cumulative law defined as:

$$\omega = \sum \frac{\Delta \bar{\epsilon}}{\bar{\epsilon}_{0i}} \quad (2.9)$$

It can be noted for the case of the Aluminium alloy Al2024–T351 (Table 2.1) that the coefficient D5 is null. This means that the temperature has no effect on the damage initiation during the cutting operation. Only, stress triaxiality ($P/\bar{\sigma}$) and strain rate effects can induce this initiation. So, as stress triaxiality and strain rate increase, the propensity for fracture increases [LEM05].

2nd Step: Damage evolution

It is noted that when ductile material damage occurs, the stress–strain relationship no longer accurately represents the material behaviour. Continuing to use the stress–strain relation introduces a strong mesh dependency based on strain localization, such that the energy dissipated decreases, as the mesh becomes smaller. Hillerborg et al. fracture energy proposal [HIL76] was exploited to reduce mesh dependency by creating a stress–displacement response after damage initiation. Hillerborg et al. define the energy required to open a unit area of crack G_f as a material parameter. With this approach, the softening response after damage initiation is characterized by a stress–displacement response rather than a stress–strain response. The fracture energy is then given as:

$$G_f = \int_{\bar{\epsilon}_{0i}}^{\bar{\epsilon}_f} L \sigma_y d\bar{\epsilon} = \int_0^{\bar{u}_f} \sigma_y d\bar{u} \quad (2.10)$$

This expression of G_f introduces the definition of the equivalent plastic displacement \bar{u} , as the fracture work conjugate of the yield stress after the onset of damage (work per unit area of the crack). The implementation of this stress–displacement concept in a finite element model requires the definition of a characteristic length L associated with an integration point. The length L is based on the element geometry, which is in the present study a 2D planar strain temperature dependent element (CPERT). For that, L is assumed to be the square root of the integration point element area. This definition of the characteristic length L is used because the direction in which fracture occurs is not known in advance (or a-priori). Therefore, elements with large aspect ratios will have rather different behaviour depending on the direction in which they crack: some mesh sensitivity remains because of this effect, and elements that have aspect ratios close to unity are recommended [ABQ07].

The damage evolution law can be specified in terms of equivalent plastic displacement or in terms of fracture energy dissipation G_f . Both these options take into account the characteristic length of the element to alleviate mesh dependency of the results. Before damage initiation, the equivalent plastic displacement is $\bar{u} = 0$. Once a particular initiation criterion is satisfied, the material stiffness is degraded according to the specified damage evolution law, and the equivalent plastic displacement becomes $\bar{u} = L\bar{\epsilon}$. This damage evolution law (Eqs. 2.11 and 2.13) describes the degradation rate of the material stiffness once the corresponding initiation criterion has been reached. It can be expressed in the linear or the exponential form. A linear damage parameter (used for tool–tip passage zone) evolves according to Eq. 2.11.

$$D = \frac{L\bar{\epsilon}}{\bar{u}_f} = \frac{\bar{u}}{\bar{u}_f} \quad (2.11)$$

Where the equivalent plastic displacement at failure \bar{u}_f , is computed as:

$$\bar{u}_f = \frac{2G_f}{\sigma_y} \quad (2.12)$$

Whereas an exponential damage parameter (used for chip) evolves according to Eq. 2.13.

$$D = 1 - \exp\left(-\int_0^{\bar{u}} \frac{\bar{\sigma}}{G_f} d\bar{u}\right) \quad (2.13)$$

The formulation of the model ensures that the energy dissipated during the damage evolution process is equal to G_f . In theory, the damage variable D reaches a value of one only asymptotically at an infinite equivalent plastic displacement. In ABAQUS®/EXPLICIT software, the overall damage variable D never equals its maximum value (one) and is enforced to be less than or equal to 0.99 when the dissipated energy reaches a value of 0.99 G_f . This ensures that the elements will remain active in the simulation, with a residual stiffness of at least 1% of original stiffness [ABQ07]. It means that no crack surfaces will be generated in the chip (Fig. 2.2, part 2); hence no chip element penetration within the chip body occurs. At any given time during the analysis, the plastic equivalent stress in the material is given by:

$$\sigma = (1 - D)\tilde{\sigma} \quad (2.14)$$

Where $\tilde{\sigma}$ is the effective (or undamaged) stress computed in the current increment. It represents the stress that would exist in the material without damage (Fig. 2.7).

In this study, G_f is provided as an input parameter and theoretically is a function of fracture toughness K_C , Young's modulus E and Poisson's ratio ν . Also, it is important to recognize that the fracture toughness parameter has different values when measured under plane stress

and plane strain assumptions. Based on fracture mechanics [WIL00], it can be assumed that in the case of the orthogonal cutting process, the two fracture modes (modes I and II) can coexist (Fig. 2.8). Mode I is a tensile mode (opening mode normal to the plane of the fracture) and concerns part 3 defined in Fig. 2.2, whereas mode II is a shearing one (sliding mode acting parallel to the plane of the fracture) and concerns part 2 (Fig. 2.2). Consequently, G_f is given in the case of plane strain by Eq. 2.15.

$$(G_f)_{I,II} = \left(\frac{1-\nu^2}{E} \right) (K_C^2)_{I,II} \quad (\text{Plane strain}) \quad (2.15)$$

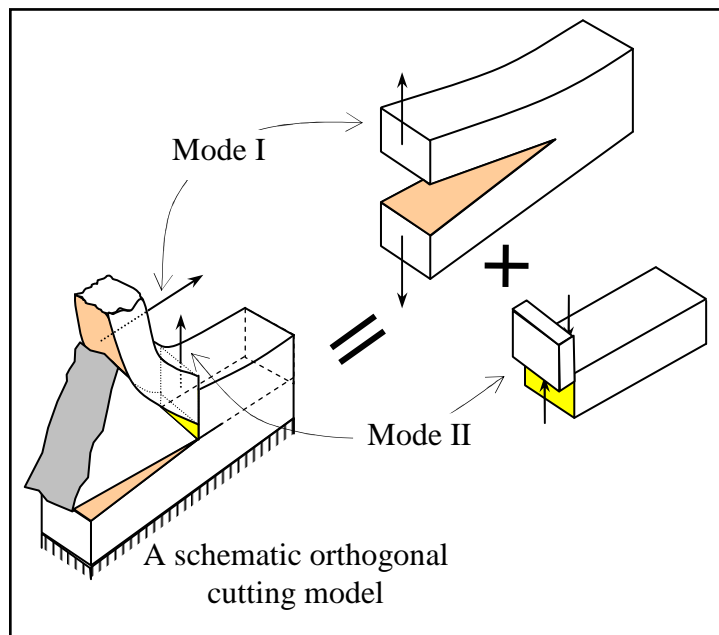


Fig. 2.8 Schematic representation of chip formation under mixed loading modes I and II

| ν | E (GPa) | K_{IC} (MPa \sqrt{m}) | K_{IIC} (MPa \sqrt{m}) |
|-------|--------------|-------------------------------|--------------------------------|
| 0.33 | 73 | 26 | 37 |

Table 2.3 Fracture toughness properties of A2024-T351 [MAT07]

Two different values of fracture energy were used as input data in ABAQUS[®]/EXPLICIT: $(G_f)_I$ for part 3 and $(G_f)_{II}$ for part 2. The subscripts I and II arise because of the different ways of loading. They refer to loading via modes I and II, respectively. The numerical values of fracture toughness according to the two modes are given by Table 2.3 [MAT07].

Hillerborg et al. fracture energy approach [HIL76] and its coupling with material damage model for machining simulation needs more explanation. In this regard elementary computing

tests dealing with a single element under simple shear loading, for different element sizes (20x20, 30x30, 50x50 and 100x100 μm) have been performed. Fig. 2.9 and Fig. 2.10 show the von Mises stress versus equivalent plastic strain and von Mises stress versus equivalent plastic displacement \bar{u} curves respectively, for different element sizes.

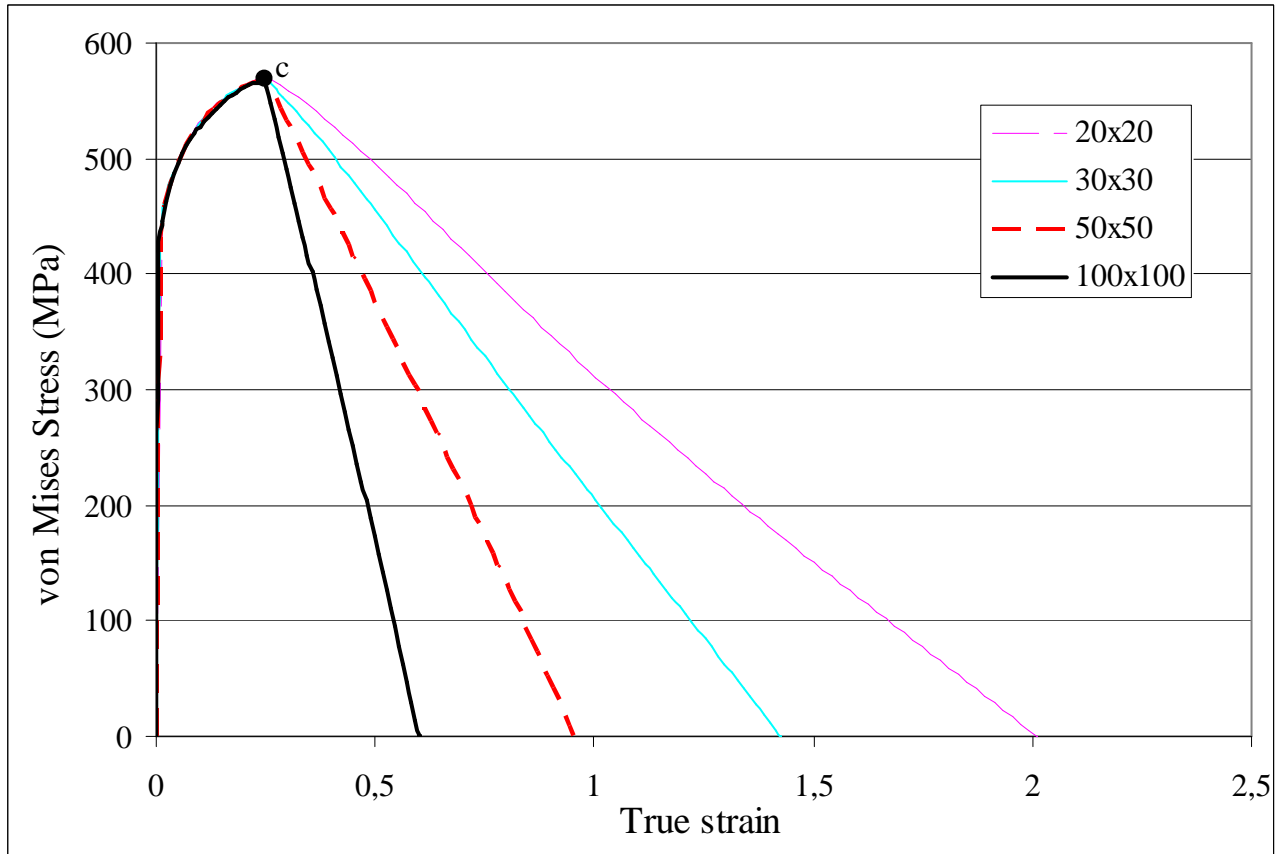


Fig. 2.9 von Mises stress vs equivalent plastic strain plot with linear damage evolution for various element sizes (μm)

Fig. 2.9 shows that stress-strain curves (for different element sizes) superimpose until damage initiation point c . However, during damage evolution phase curves for various elements sizes can be distinguished; higher is the strain as the mesh becomes smaller and vice versa. This depicts the importance of mesh dependency on the result. Nevertheless, the fracture energy proposal of Hillerborg allows reducing mesh dependency by creating a stress–displacement response after damage initiation; as explained earlier. Fig. 2.10 shows stress–displacement curves for various element sizes for the same G_f (given as input property). All curves superimpose during damage evolution phase, in contrast to stress–strain curves (Fig. 2.9).

During damage evolution step a similar dissipation of energy (G_f) for all mesh sizes is required. The element characteristic length L and the equivalent plastic strain $\bar{\epsilon}$ are the only changeable parameters (as stress doesn't change until damage initiation (point c). This means that the stiffness of a coarse element (with higher characteristic length L) can be degraded just by lowering G_f value (Eq. 2.11 to 2.14). In machining simulations this helps to capture the localised deformation zones (for example shear zones leading to segmented chip).

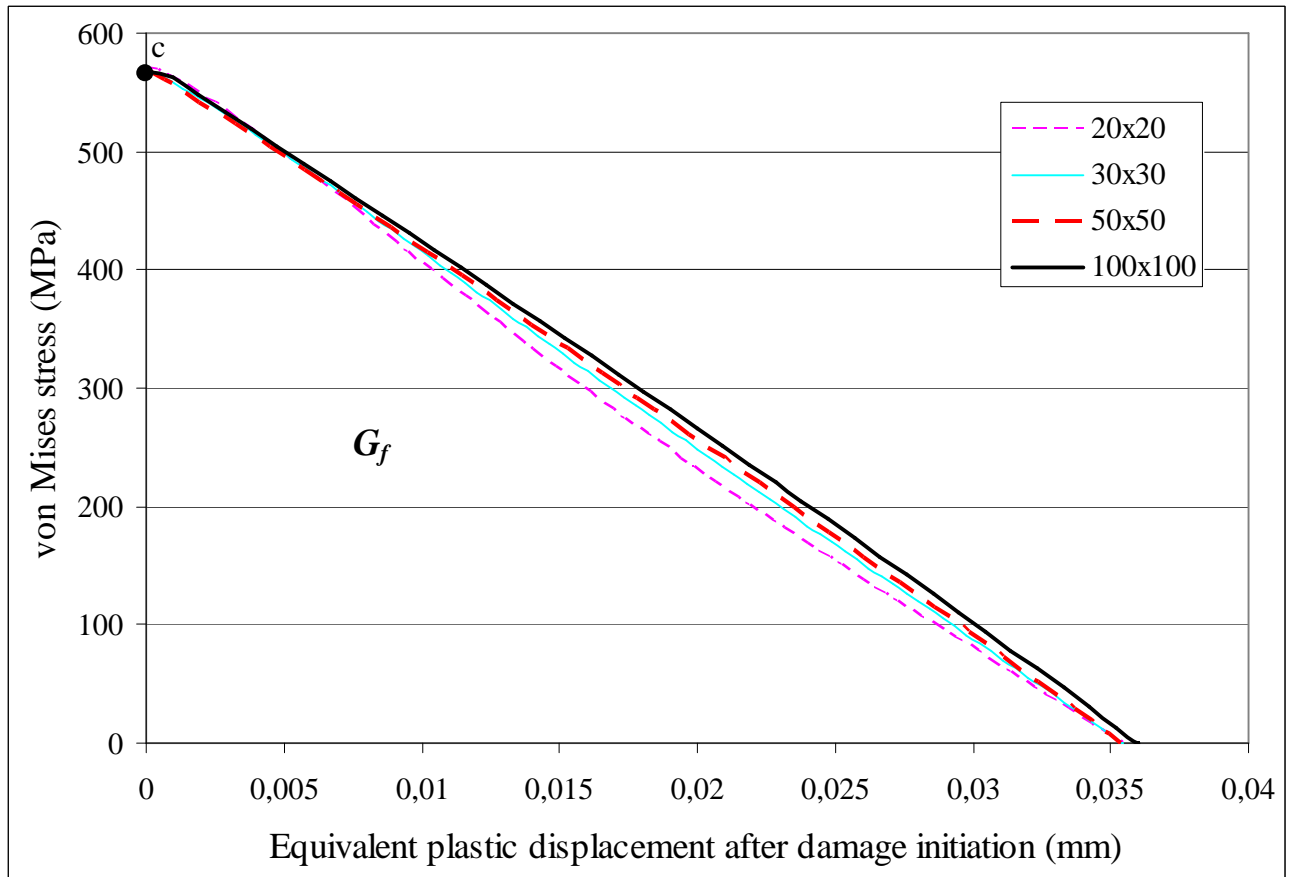


Fig. 2.10 von Mises stress vs equivalent displacement plot with linear damage evolution for various element sizes (μm)

2.3.5 Heat transfer modelling

In machining, substantial amounts of heat may be generated due to both plastic deformation and friction at the tool-chip interface. The temperature attained can be quite higher and has a considerable influence on the mechanical properties of the material. The heat generation due to plastic deformation and friction is modelled as a volume heat flux. Heat conduction is assumed as the primary mode of heat transfer, which occurs within the workpiece material and at the tool-chip interface.

If a local temperature rise of ΔT_p (due to inelastic work) in the workpiece during a period of time Δt , the heat generation rate \dot{q}_p due to inelastic work, added to the thermal energy balance, is given by Eq. 2.16.

$$\dot{q}_p = \eta_p \bar{\sigma} \cdot \dot{\bar{\epsilon}} \quad (2.16)$$

Where η_p is the inelastic heat fraction, also called the Taylor–Quinney empirical constant usually taken equal to 0.9 [LEM88 and ABQ07].

The heat generated by friction forces induces a rise in temperature ΔT_f during a period of time of Δt . The fraction of dissipated energy η_f caused by friction is assumed equal to 1. From the fraction η_f , an amount of heat J remains in chip and $(1-J)$ is conducted to the insert. For the present model a default value of $J = 0.5$ is used. The volumetric heat flux \dot{q}_f corresponding to friction state is calculated according to Eq. 2.17:

$$\dot{q}_f = \rho C_p \frac{\Delta T_f}{\Delta t} = \eta_f J \tau_f \dot{\gamma} \quad (2.17)$$

The shear stress τ_f is given by Coulomb's law and $\dot{\gamma}$ is the slip strain rate.

2.4 Experiment for orthogonal turning

To carry-out the experimental investigations, two working parameters were considered. The cutting speed $V_C = (200-400-800)$ m/min and the feed rate $f = (0.3-0.4-0.5)$ mm/rev, whereas the cutting depth was kept constant ($a_p = 4$ mm). These values were chosen from the range of tool manufacturer's data [SAN07] for the material studied. A geometrical analysis of the chip was performed by polishing and etching. Videos were filmed to analyse and calculate the fragmentation frequencies. Moreover, measurements at high-frequency sampling of cutting force signal were achieved.

2.4.1 Experimental device

In order to perform straight turning operations, the workpiece was prepared with coaxial cylindrical grooves (Fig. 2.11). The cutting tool was composed of an uncoated carbide insert (rake angel 17.5° , clearance angel 7°) referenced CCGX 12 04 08-AL H10, which was fixed on an insert holder SCLCR 2020 K 12. To reproduce orthogonal cutting conditions, the insert cutting edge was orthogonal with feed rate and cutting speed (Entering angle $K_r = 90^\circ$ and inclination angle $\lambda_s = 0^\circ$). Both the insert and the holder were from Sandvik. The machining

was carried out on a universal lathe Gallic 20. The measuring equipment was composed of a standard dynamometer (Kistler 9257B), charge amplifiers (Kistler 5015A) and a high-frequency data acquisition device (National Instrument NI 4472). The signal acquisition was gathered with LabView[®] software, and data treatment was developed with Matlab[®] [GIR10]. Videos were filmed with a high-speed camera (Motion Scope 8000 Redlake).

2.4.2 Geometrical analysis

For each trial, chips were embedded in an allylic resin, polished and etched with an alcoholic solution of 4% nitric acid (Fig. 2.12). After that, chip fragments were photographed using a microscope. The saw-tooth shapes can be recognized on them (Fig. 2.13). In the literature, this morphology is known as segmentation whereas the fragmentation corresponds to chip fracture. In Fig. 2.13 it can be seen that the chip extremities are characterized by sharper segments than in its middle when observed along its length. This shows that in the case of the specified working parameters, the sharpest segments induce fragmentation. This typical morphology will again be pointed out during the presentation of the numerical results in section 2.5. In Fig. 2.13b the sharpest segments were localized along the chip length due to the cutting speed increase, which often has been noticed in the literature. In order to quantify the segmentation and fragmentation frequencies a bespoke software was developed [KAL07]. Wavelengths were measured by analysing pixels of chip pictures. After that, frequencies were calculated with a cutting speed and incompressible material assumptions [BEL05]. The results are presented in Fig. 2.14.

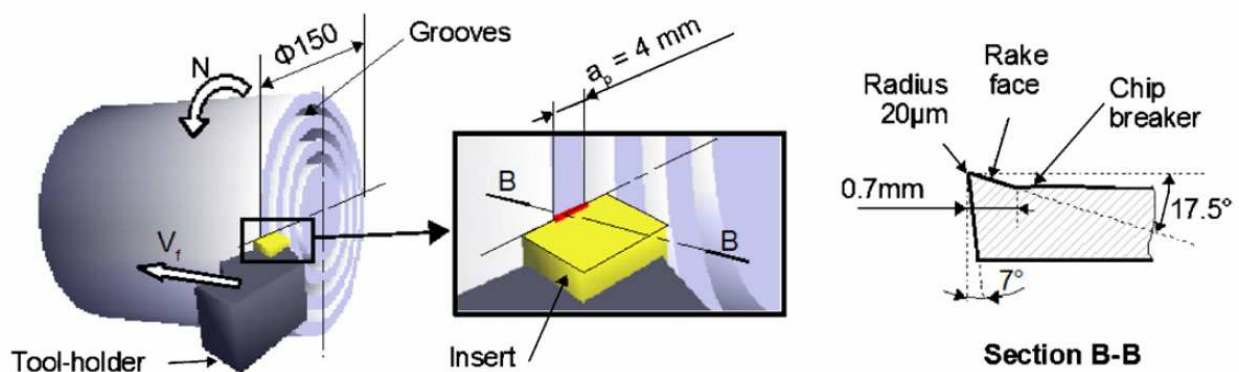


Fig. 2.11 Workpiece preparation and tool geometry



Fig. 2.12 Chips embedded in resin ($f = 0.4$ mm/rev, $V_C = 200, 400$ and 800 m/min)

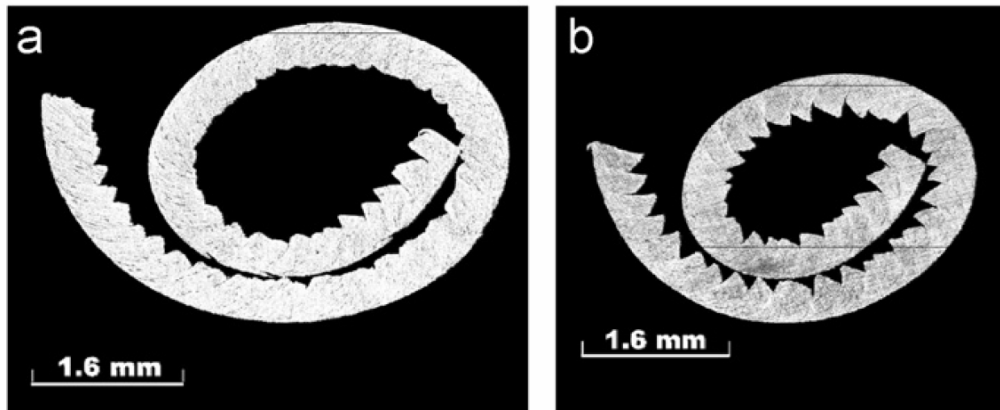


Fig. 2.13 Chip morphology for $f = 0.4$ mm/rev a) $V_C = 200$ m/min and b) $V_C = 800$ m/min

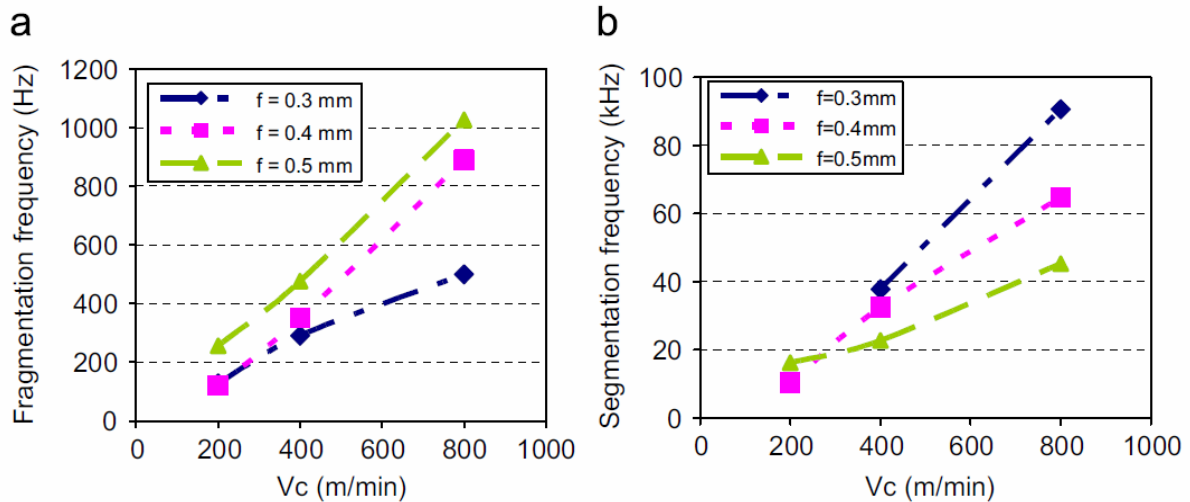


Fig. 2.14 a) Fragmentation and b) segmentation frequencies according to cutting speed variation for different feed rate values

2.4.3 Video acquisition results

The acquisition with the high-speed camera was limited to 4000 fps (frames per second). This sampling frequency (4 kHz) restricts detection of the chip segmentation phenomenon,

characterized by frequencies higher than 10 kHz. Therefore, chip fragmentation was observed, and its frequency (about 100 Hz for $V_C = 200$ m/min) was precisely measured. This chip fragmentation is illustrated in Fig. 2.15.

Even if the highest sampling speed had been used for a better accuracy in the calculated frequency values, the presented pictures are not of high quality. Nevertheless, the tool rake face and the curled chip can be seen on them. Fig. 2.15a corresponds to a given time in which a chip with a curled-up shape can be observed. It can also be noted that this chip is in contact with the workpiece. This can induce high bending loads on the chip. Consequently, chip fracture occurs and will be repeated periodically near and just above the rake face (Fig. 2.15b). Moreover, geometrical analysis had shown that fragmentation occurs in the highest segmented zone. Thus, this segmentation may depend on chip–workpiece contact. By measuring and counting 20 periods corresponding to the chip fracture during video sequences for $f = 0.4$ mm/rev and $V_C = 200$ m/min, the mean value of fragmentation frequency is 111 Hz. This result is close to the value deduced by geometrical analysis (Fig. 2.14a).

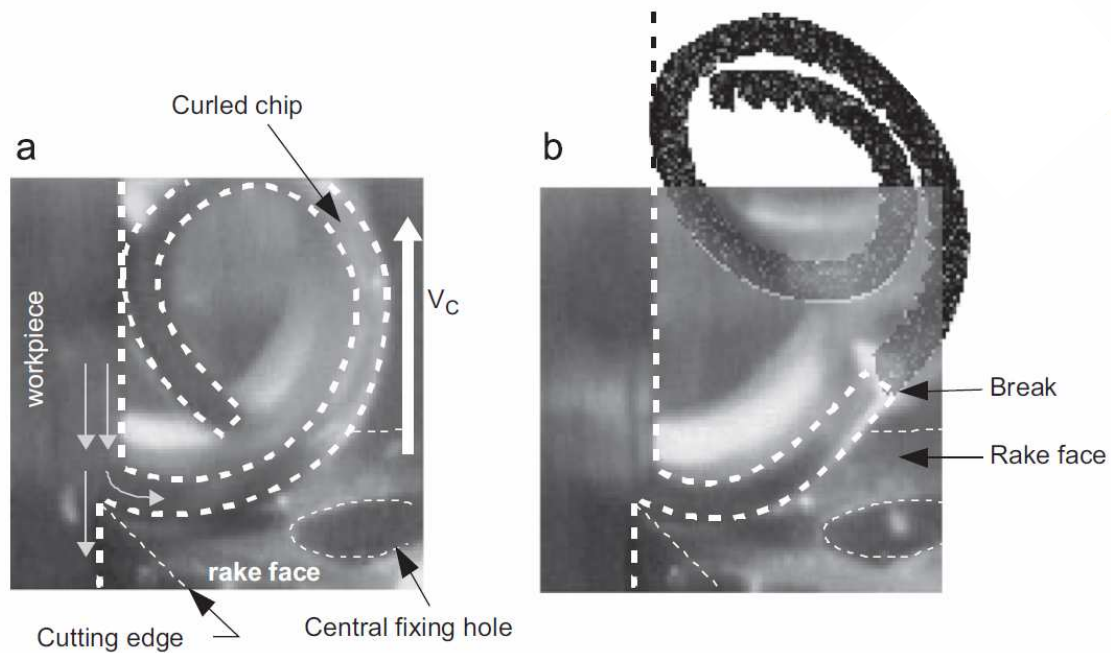


Fig. 2.15 Fragmentation phenomenon observed with video acquisition for $V_C = 200$ m/min and $f = 0.4$ mm/rev.

2.4.4 Cutting force measurement

The temporal signal presented in Fig. 2.16a corresponds to the cutting force evolution with respect to time. Only the central zone between 0.25 and 1.10 s, corresponding to an established cutting regime, was analysed. Based on Fast Fourier Transform algorithm (FFT), the frequency spectrum shown in Fig. 2.16b has been computed [GIR10].

The first peak was attributed to the fragmentation because its frequency value varies with cutting speed and feed rate. For the cutting parameters of this presentation in Fig. 2.16 ($V_C = 200$ m/min, $f = 0.4$ mm/rev) the fragmentation frequency was localized between 98 and 110 Hz. Another frequency peak is centred at 350 Hz and presented on all trial diagrams with different cutting speeds and feed rates. So, it can be said that this peak may correspond to a natural vibration mode of an element of the cutting system and not to physical phenomena accompanying chip formation. The force average values of exploited zones were calculated, and the results are given in Fig. 2.17.

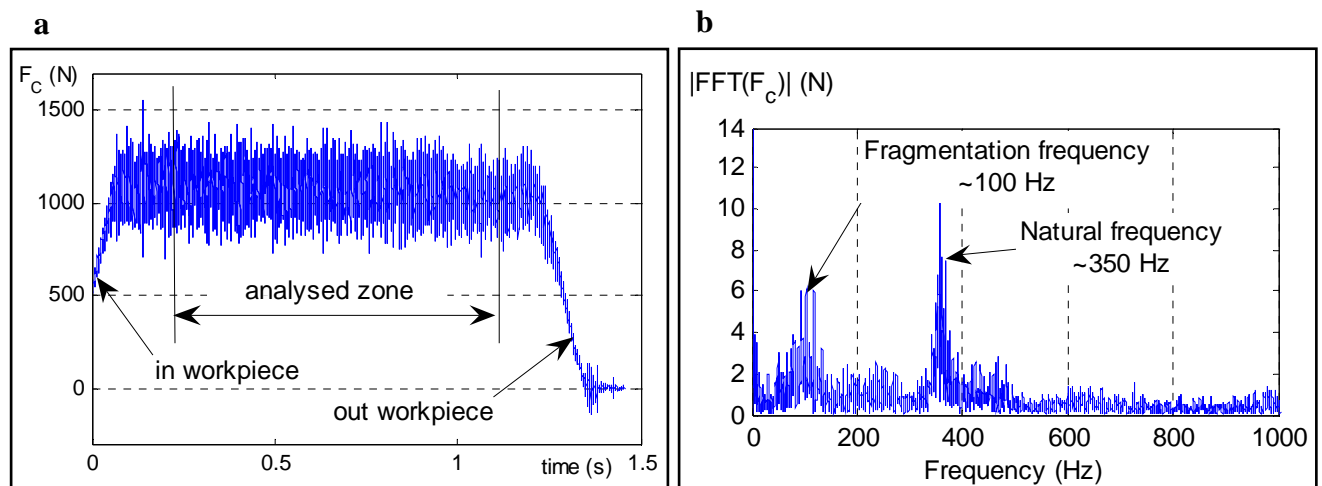


Fig. 2.16 Cutting force evolution versus time and (b) its frequency spectrum ($V_C = 200$ m/min, $f = 0.4$ mm/rev)

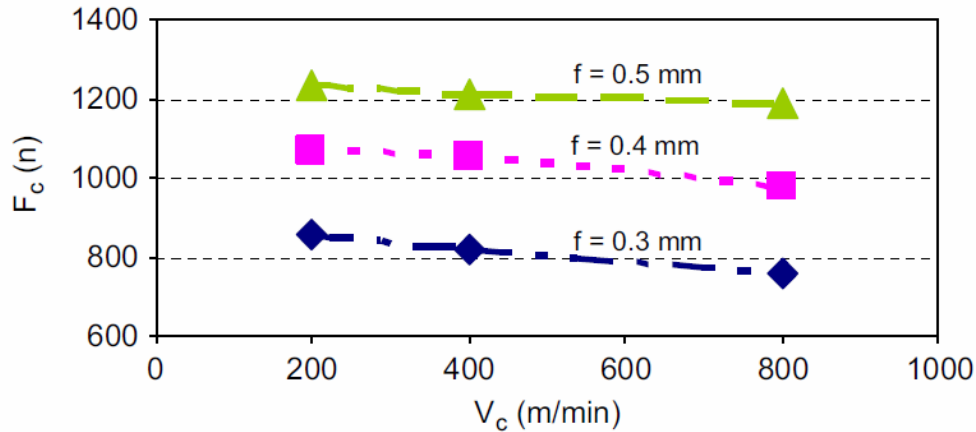


Fig. 2.17 Evolution of cutting force according to cutting speed variation for various feed rate values

2.5 Results and discussion on orthogonal turning operation

In the present section numerical results concerning the orthogonal turning operation of Aluminium alloy A2024-T351 are discussed. A comparison between chip morphology, segmentation and fragmentation obtained experimentally and numerically is presented. Moreover, the evolution of cutting force is treated according to cutting speed variations. Finally, the physical mechanisms governing chip tooth shape genesis and their effects on machined surface are studied.

Fig. 2.18 shows the distribution of damage D corresponding to material degradation stiffness for a complete chip formation at the cutting time $t_c = 770 \mu\text{s}$. The working parameters considered are $V_c = 800 \text{ m/min}$ and $f = 0.4 \text{ mm/rev}$. It is remarked that this damage is localized mainly in the shearing zones and in the locations related to tool–workpiece interaction. The inner zone of the chip obtained numerically shows narrower segments especially in the zones where the chip presents small curvature radii. This result is qualitatively similar to that obtained experimentally (Fig. 2.13b). In fact, as the chip is even rolled up (or curled up), the segments are closed again.

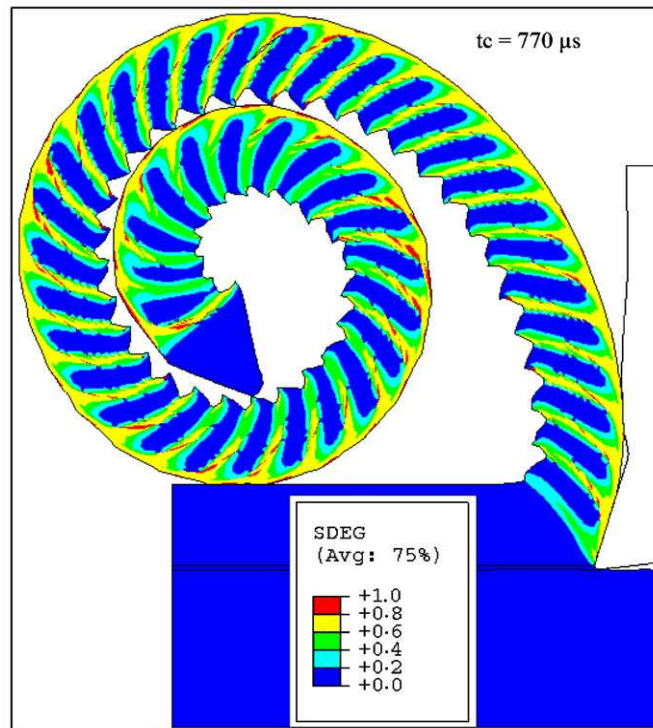


Fig. 2.18 Computed damage evolution ($f = 0.4$ mm/rev, $V_C = 800$ m/min)

In the objective to improve comprehension of chip genesis, attention is focused on the steps characterizing the formation of one chip segment. Figs. 2.19–2.21, give the distributions of equivalent von Mises stresses, temperature and equivalent plastic strain during a chip segment genesis, respectively.

In Fig. 2.19, an increase in equivalent von Mises plastic stresses is to be noted in the primary shear zone with a decrease in stresses near the tool tip due to a loss in material stiffness. Consequently, the equivalent plastic strain (Fig. 2.20) and temperature (Fig. 2.21) increase near the tool tip and evolve towards the chip-free side.

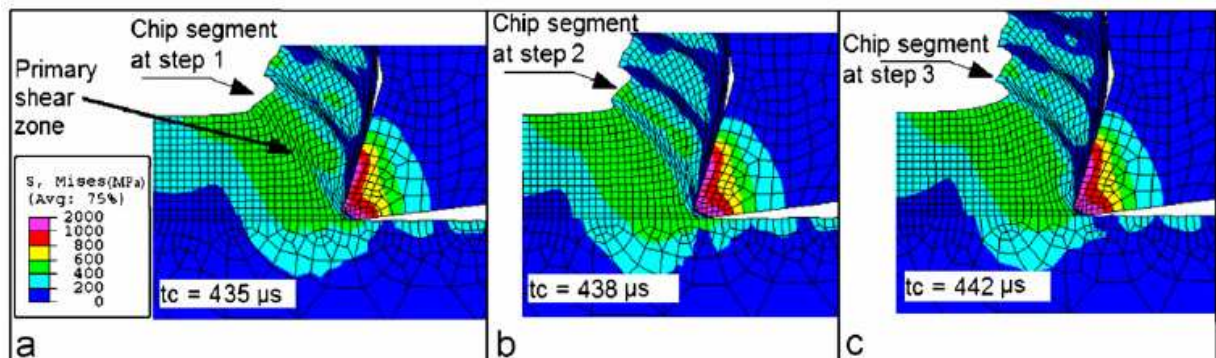


Fig. 2.19 Distribution of von Mises equivalent stresses during steady cutting regime ($f = 0.4$ mm/rev and $V_C = 800$ m/min)

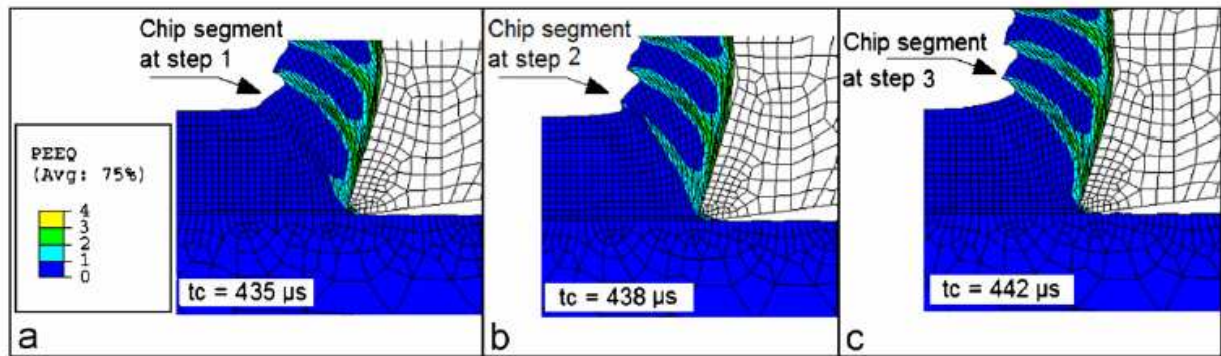


Fig. 2.20 Distribution of equivalent plastic strain during steady cutting regime ($f = 0.4$ mm/rev and $V_C = 800$ m/min)

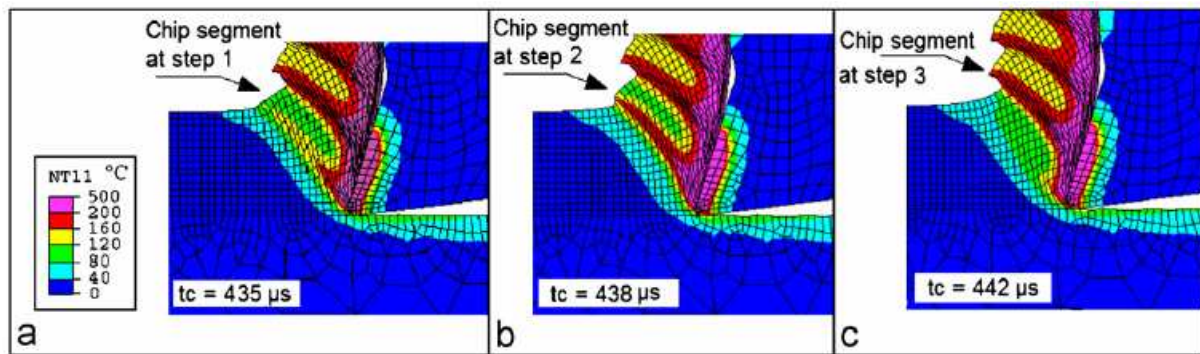


Fig. 2.21 Distribution of temperature during steady cutting regime ($f = 0.4$ mm/rev and $V_C = 800$ m/min)

The damage occurring near the tool tip will extend in the second stage. So, the stresses fall and the equivalent plastic strain increases. Moreover, localized damage takes place on the chip-free surface. In the final stage the damage is extended along the primary shear zone due to the excessive compression state. As shown by Figs. 2.19 to 2.21 and the previous study on AISI4340 steel [MAB06], that the segmentation is the result of a softening state during tool–workpiece interaction. Nevertheless, this is not the only phenomenon yielding to the chip segmentation; other phenomena can participate in the formation of the saw-tooth chip shape such as pre-existing micro-cracks, machine tool vibrations or chip–workpiece contact. Although the later remark is not noticed in previous cutting parameters, it can be demonstrated by Fig. 2.22, where the damage variable D for $V_C = 200$ m/min and $f = 0.4$ mm/rev is shown.

In this figure the absence of chip segmentation is observed at the beginning of its formation (except the segment due to chamfer, Fig. 2.22a). When the chip begins to curl up and for its

first self-contact on its free side at the time $t_c = 864 \mu\text{s}$, the segment genesis begins near the chip root (Fig. 2.22b). After that, the segmentation phenomenon is initiated (Fig. 2.22c), which is mainly due to the increase in shear stresses in the shearing primary zones. After a certain cutting time, the curled-up chip is subjected to high loads: those due to its contact with the workpiece and those caused by the tool advancement. These will provoke a bending state on the chip and consequently induce chip fragmentation as it is shown by the photo capture (Fig. 2.22d) taken experimentally and the computed values of chip damage shown by Fig. 2.22e. Therefore, this numerical result is in concordance with those about the fragmentation presented in section 2.4.3.

The evolution of the numerical values of damage D computed with reference to initial chip-free sides is also shown in Fig. 2.23. Three thresholds can be observed corresponding to Fig. 2.22a, b and e. The global damage curve oscillates according to segmentation phenomenon and does not attain unity and hence there is no inter-penetration in chip elements.

The evolution of mean cutting force deduced by numerical simulations regarding cutting speed for a feed rate of 0.4 mm/rev is presented in Table 2.4. It is remarked that, for given similar cutting conditions, the numerical results are close to experimental ones with a deviation less than 10%.

The chip morphology study in itself is not the final aim, but the main objective remains the understanding of its effect on tool wear, machined surface integrity, etc. The exploitation of the presented model had allowed the prediction of the effect of saw-tooth chip morphology on the machined surface.

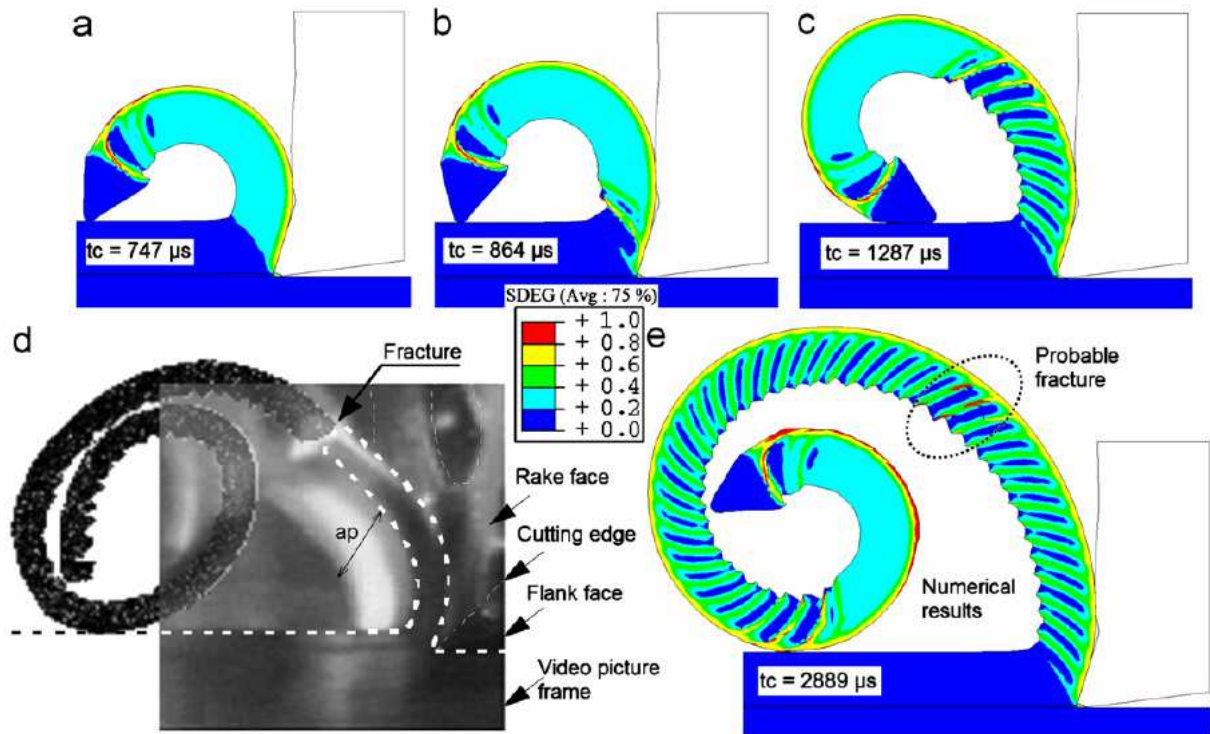


Fig. 2.22 Chip morphology evolution ($V_C = 200$ m/min and $f = 0.4$ mm/rev) regarding damage variable D (SDEG) and experimental comparison

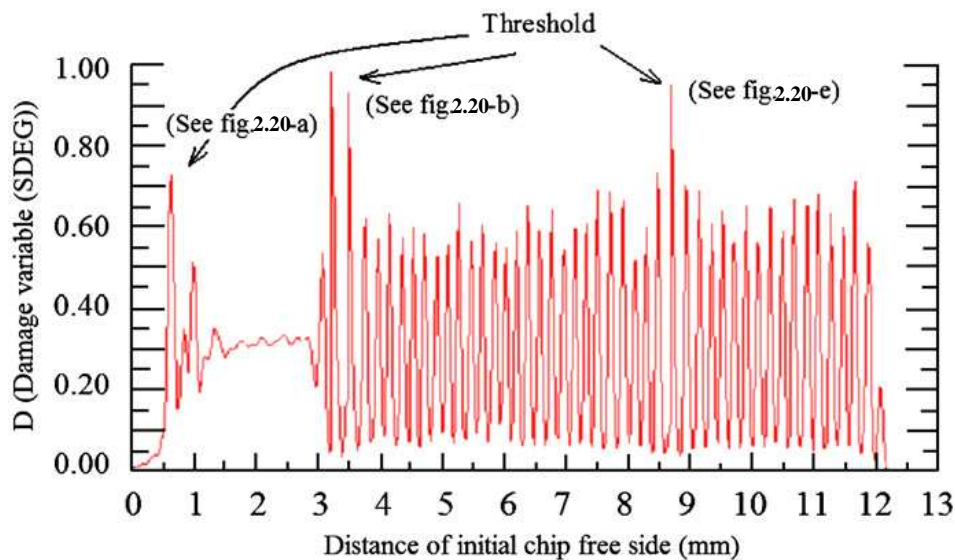


Fig. 2.23 Computed damage variable D (SDEG) according to the distance of initial chip free side

Fig. 2.24 represents the distribution of the von Mises stresses on the workpiece after the passage of the cutting tool ($V_C = 800$ m/min, $f = 0.4$ mm/rev). A waved (or rippled) geometry

yielding to a residual strain state on the morphology is noted. This morphology has a profile with valley and peak shaped locations as shown in detail (a) in Fig. 2.24, representing an anamorphic profile of the machined surface.

| $f = 0.4 \text{ mm/rev}$ | | | |
|-------------------------------|-----|-----|-----|
| $V_C \text{ (m/min)}$ | 200 | 400 | 800 |
| $F_C \text{ (N) computed}$ | 898 | 994 | 901 |
| Deviation with experiment (%) | 4 | 6 | 8 |

Table 2.4 Cutting force deduced by numerical simulations regarding cutting speed variation

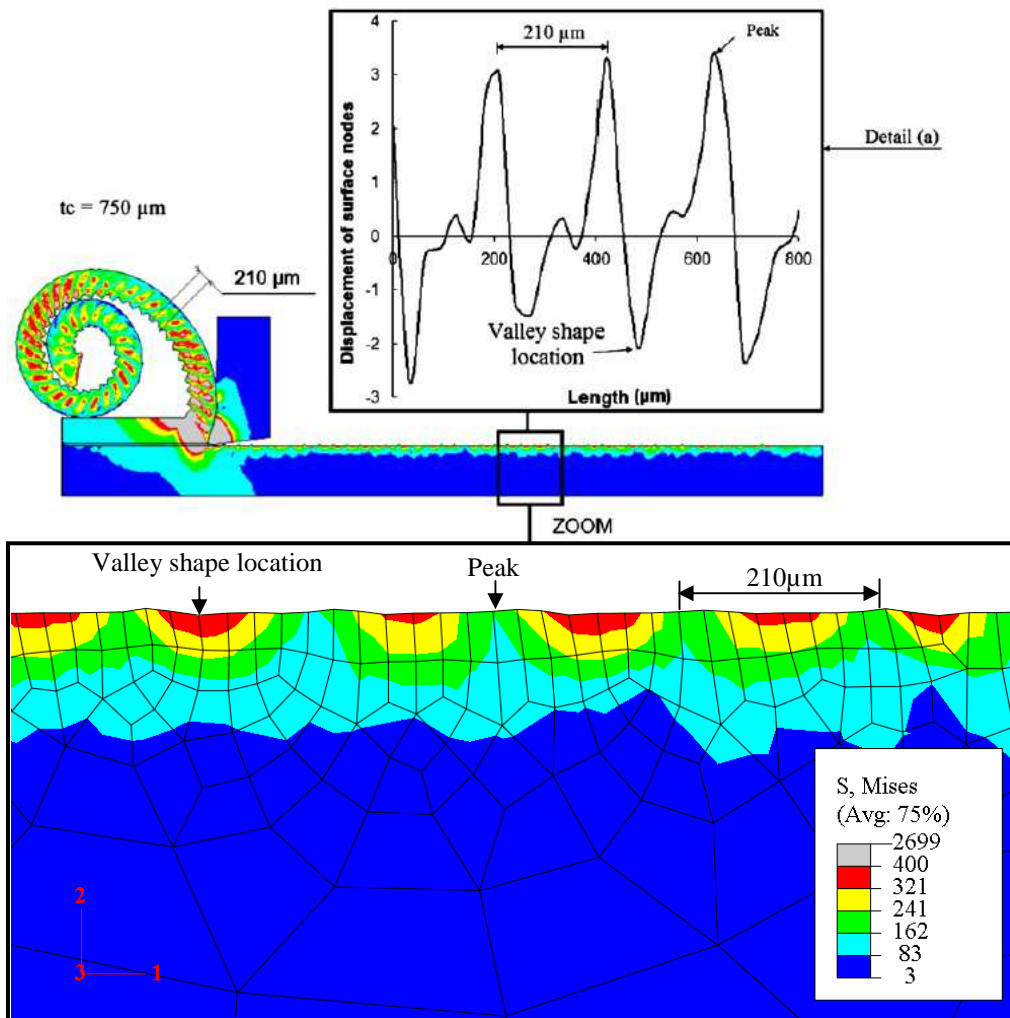


Fig. 2.24 Equivalent von Mises plastic stresses on the machined surface ($V_C = 800 \text{ m/min}$ and $f = 0.4 \text{ mm/rev}$)

Moreover, a high stress magnitude (up to 400 MPa) on the valley-shaped location distributed periodically between one or two grid elements (one element 30x30 mm, approximately) is remarked. This can cause local material deformation. Consequently, it is interesting to detect the evolution of both the residual stresses σ_{11} (in the cutting direction) and σ_{22} (workpiece depth direction) in the valley-shaped locations and peaked zones (Fig. 2.25). It can be seen in Fig. 2.25 that σ_{11} stress in tension; acting on the peaked zones locations up to a depth of 30 mm, becomes a compressive one up to 300 mm workpiece depth, while the σ_{22} stress remained compressive one. On the valley-shaped locations both the σ_{11} and σ_{22} stresses are positive. This can explain the periodicity of ripples on the machined surface.

In addition, it is important to underline that comprehension of residual stress distributions after machining operations is of great interest to the industry because their values and orientations can affect the functional mode of the whole machined part in a global given mechanical system.

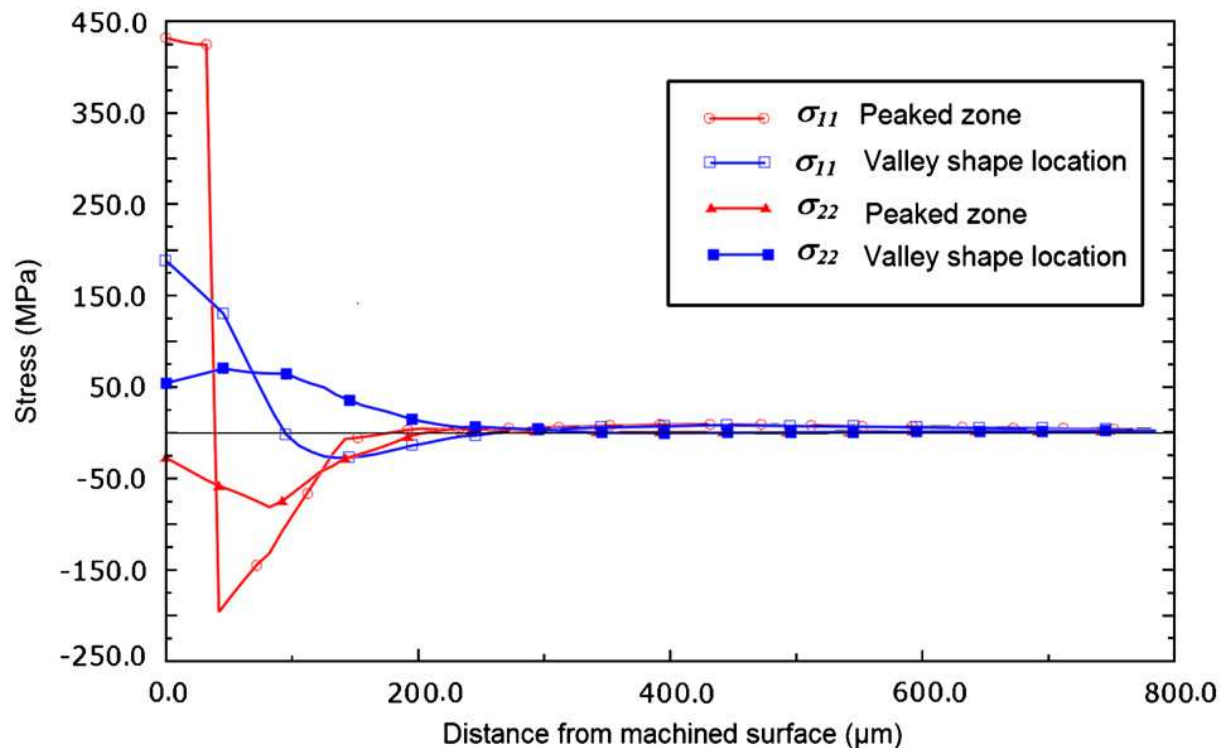


Fig. 2.25 Distribution of residual stresses under the machined surface ($V_C = 800$ m/min and $f = 0.4$ mm/rev)

2.6 Modelling of an orthogonal peripheral down-cut milling case

2.6.1 Geometrical and material models

Once the numerical model for orthogonal turning was established and validated experimentally, it was exploited for the case of orthogonal milling process. The objective is to study the evolution of chip morphology during milling process and its eventual effects on surface integrity. Sensitivity of fracture energy G_f on chip morphology has also been studied.

In the numerical model conceived for milling the tool/cutter is considered as a rigid body, which by definition is a collection of nodes, elements, and/or surfaces whose motion is governed by the motion of a single node, called the rigid body reference node. Rigid bodies are usually used to model very stiff components, either fixed or undergoing large motions. For example, rigid bodies are ideally suited for modelling tooling like punch, die, blank holder, roller, tool inserts etc. The principal advantage to represent features of a model with rigid bodies rather than deformable body is essentially the computational efficiency.

As tool is modelled as rigid body, so all the boundary conditions has been applied to its reference point (tool centre of rotation is selected as rigid body reference point for this study). Tool can advance with feed velocity V_f in negative x-axis direction and can rotate anti-clockwise with angular velocity ω_r , which dictates its cutting velocity. Rest degrees of freedom are blocked for tool motion. The simulations were run for a tool diameter 25 mm, feed rate 0.4 mm/rev and cutting speeds of 200, 300, 400 m/min.

As the tool rotates and advances simultaneously, so the cutter traces the trochoidal path in ideal case i.e. if vibration characteristics of tool are ignored [MON91]. This produces a chip of variable section. Trochoidal path set of equation (Eq. 2.18) was used to model the milling cutter path zone (chip separation zone with thickness of $30\mu\text{m}$, which is greater than $R_n=20\mu\text{m}$ [SUB08]) and chip section geometry.

$$\left. \begin{aligned} x_i(t) &= V_f \cdot t + \frac{D_T}{2} \cdot \cos\left(\frac{2 \cdot i \cdot \pi}{z} + \omega_r \cdot t\right) \\ y_i(t) &= \frac{D_T}{2} \cdot \sin\left(\frac{2 \cdot i \cdot \pi}{z} + \omega_r \cdot t\right) \end{aligned} \right\} \quad (2.18)$$

Where x_i and y_i are the coordinates of the i^{th} tooth of the milling tool ($i=1, 2, \dots, z$, where z is total number of teeth of the tool), D_T tool diameter and t is cutting time. The trochoidal paths traced by two cutter teeth are shown in Fig. 2.26. Only the half portion of crescent moon like chip; for down-cut milling is modelled in the present study. The milling model thus conceived

is shown in Fig. 2.27. Material behaviour modelling, chip separation criteria are the same as has been used in case of orthogonal turning model case (section 2.3.4).

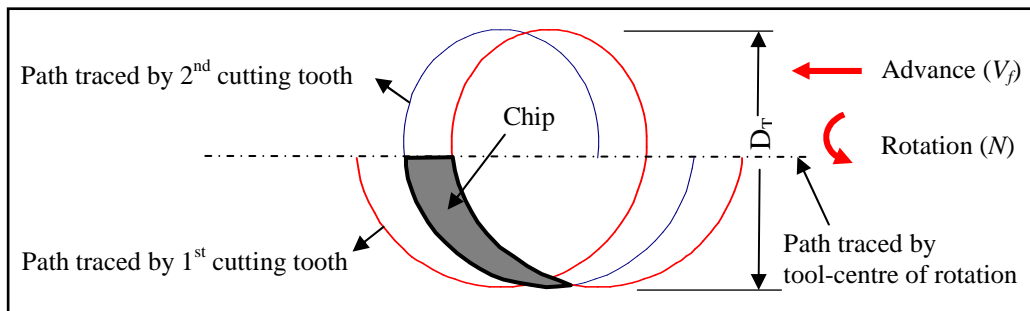


Fig. 2.26 Trochoidal paths traced by two cutter teeth

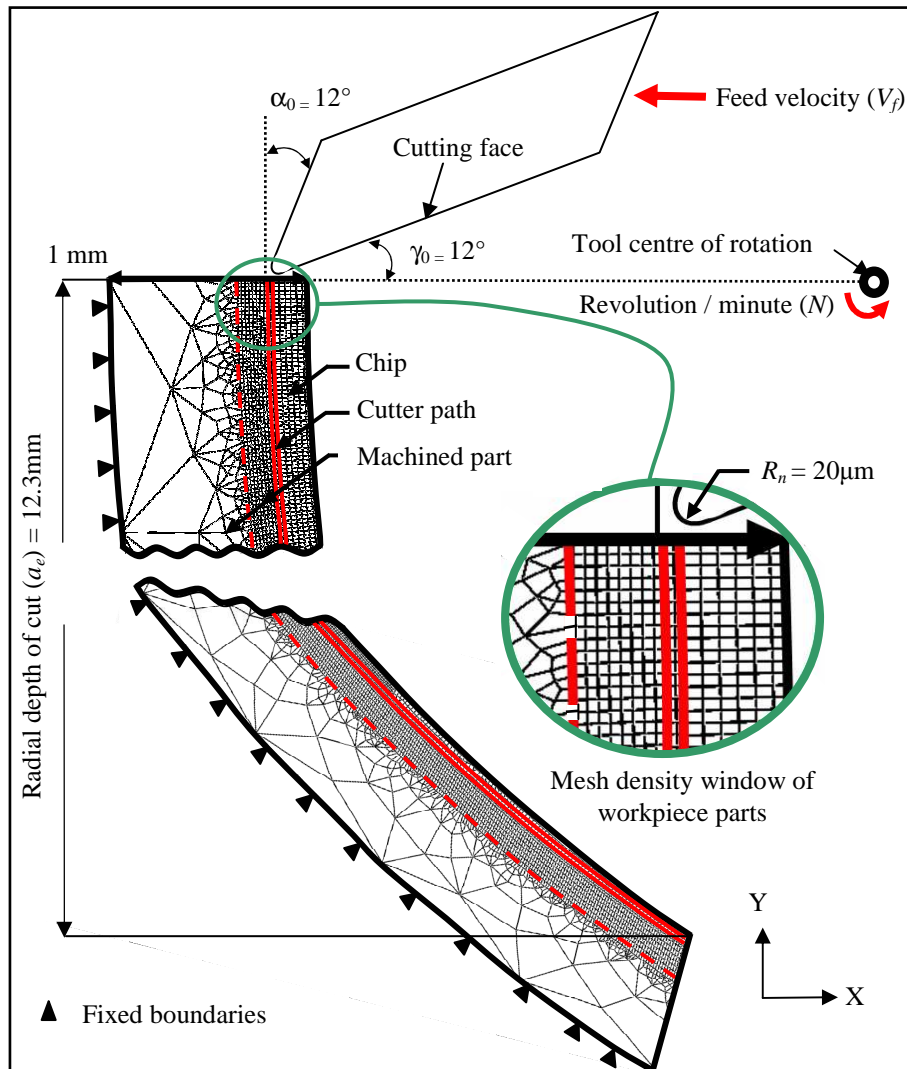


Fig. 2.27 Tool workpiece geometrical model and boundary conditions for 2D down-cut milling

2.6.2 Meshing and interactions

For the workpiece, the same element type; that has been used for straight turning modelling previously, were used to model the orthogonal peripheral down-cut milling case, whereas the cutter is meshed using 2- node 2D linear rigid link elements.

After mesh sensitivity tests (as described in section 2.3.3) different mesh densities have been conceived in different parts of workpiece. Mesh densities were increased in the regions of interest; for example tool path zone, chip section and 80-100 μm of machined part (in radial direction) to observe residual stresses and surface topology due to machining. Table 2.5 shows the mesh sizes realized for the present model. Tool-workpiece interactions and friction model are the same as have been used in the case of orthogonal turning model (section 2.3.2).

| Workpiece Parts | Element Dimension (μm) | |
|------------------|---------------------------------------|--------------------------------------|
| | Maximum | Minimum |
| Chip | 28 x 20 (7 rectangular mesh elements) | 3 x 20 (7 rectangular mesh elements) |
| Cutter Path Zone | 15 x 20 | 15 x 20 |
| Machined part | 40 x 30 | 20 x 20 |

Table 2.5 Workpiece mesh density for 2D milling model

2.7 Results and discussion on orthogonal down-cut milling

In the present section numerical results concerning the orthogonal milling process of Aluminium alloy A2024-T351 are discussed. The evolution of chip morphology during down-cut milling process and its eventual affects on machined surface profile and residual stresses are analysed. Sensitivity of fracture energy G_f value on chip morphology has also been discussed. Simulations have been performed for cutting velocities: 200, 300 and 400 m/min and considering a fixed feed rate of 0.4 mm/rev. The chip morphology obtained by computation is compared with the experimental one.

Fig. 2.28 shows temperature distribution on chip and workpiece parts. Maximum temperatures are localised on chip inner surface. Nevertheless, numerical chip morphology is less comparable with the experimental one (Fig. 2.29), where the presence of some sharp teeth (segmented chip morphology) can be noticed.

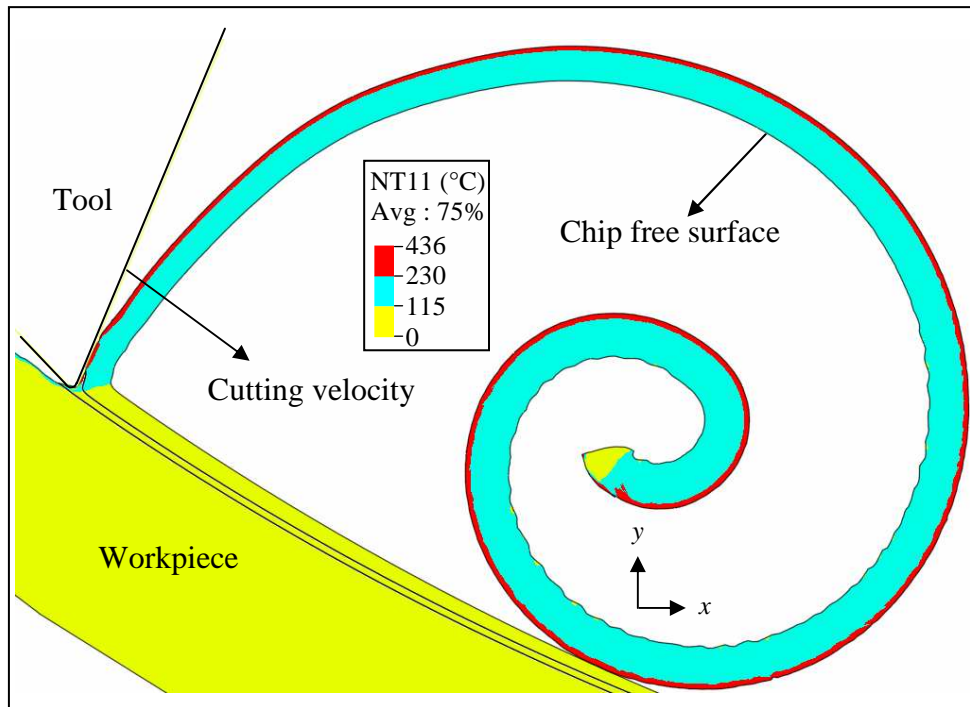


Fig. 2.28 Temperature evolution and chip morphology ($G_f = 18 \text{ N/mm}$, $V_C = 200 \text{ m/min}$)

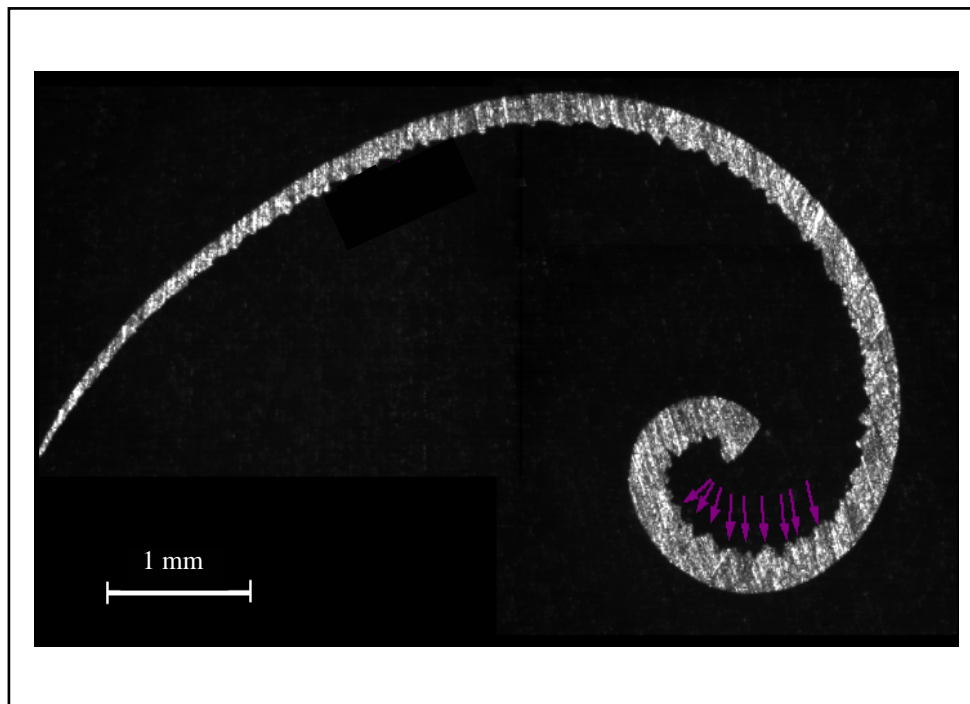


Fig. 2.29 Experimental chip for A2024-T351 ($V_C = 200 \text{ m/min}$, $a_P = 4 \text{ mm}$, $f = 0.4 \text{ mm/rev}$)

This shows that the existing mesh is unable to capture the localised deformation phenomena leading to segmented chip morphology. Therefore, either the mesh density should be

increased [BAR05, CAL08] or material fracture energy G_f (input material parameter) must be decreased (Hillerborg fracture energy proposal [HIL76], detailed in section 2.3.4). A lower fracture energy value enhances the material tendency to deform easily or lose its stiffness. This results in high strain values, leading to an increase in temperature and hence thermal softening. This enhances the generation of shear-localized deformation regions, producing segmented chip morphology during machining process.

Fig. 2.30 presents the chip morphology for $G_f = 16$ N/mm, which initially was given as $G_f = 18$ N/mm (Fig. 2.28). It can be observed that initially sharp teeth are observed. These disappear as UCT decreases and approaches to micro level dimensions (this is due size effect phenomena usually attributed to define the increase in material strength, when UCT decreases to a few microns. This phenomenon is detailed in chapter 3). The chip morphology is comparable with experimental one (Fig. 2.29).

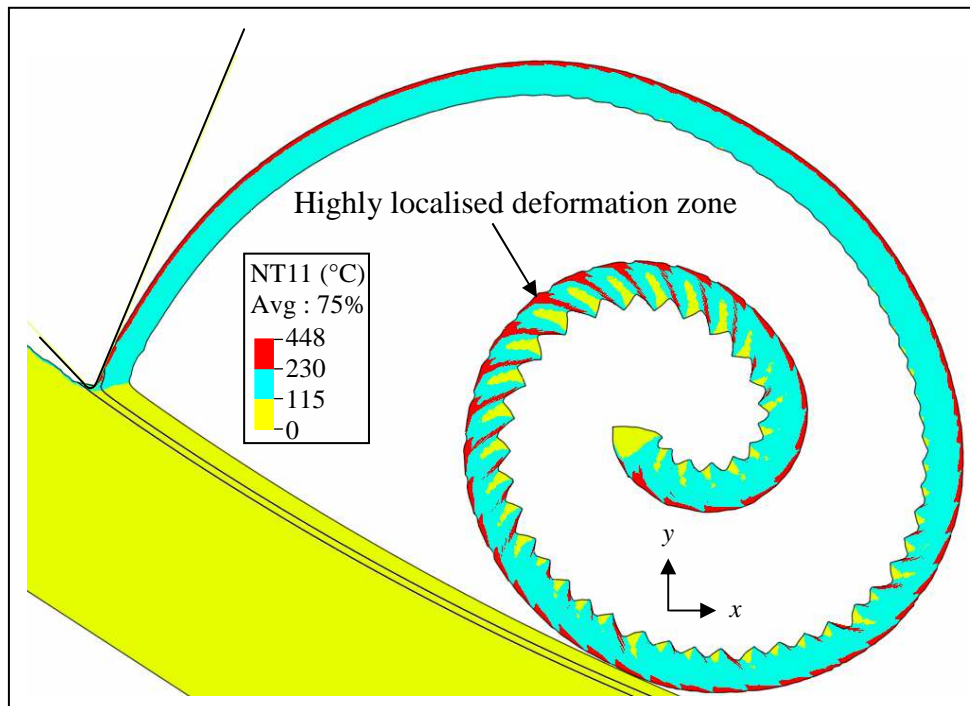


Fig. 2.30 Temperature evolution and chip morphology ($G_f = 16$ N/mm, $V_C = 200$ m/min)

Similar trend in chip morphologies for comparatively higher cutting speeds of 300 and 400 m/min was observed as shown in Fig. 2.31 and Fig. 2.32, respectively. By decreasing G_f , segmented chip morphologies with highly localised deformations zones were obtained.

Fig. 2.33 shows the von Mises stress distribution on the machined workpiece for $V_C = 400$ m/min. It can be seen that machined workpiece (Fig. 2.33 A) is under high stress field and plastic deformation of the machined material is apparent (especially on machined surface).

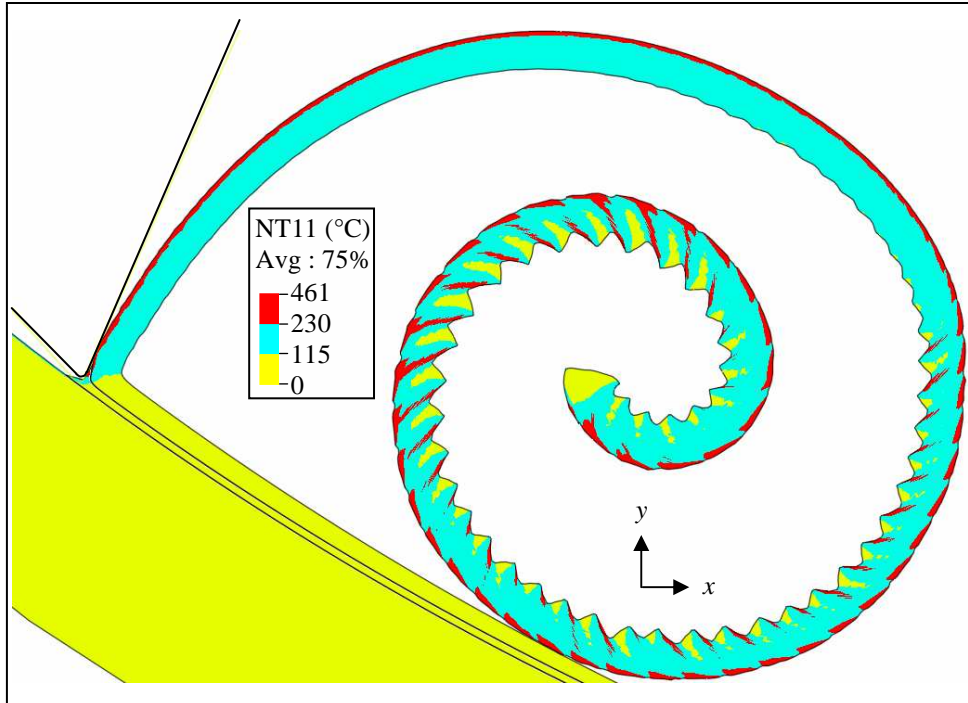


Fig. 2.31 Temperature evolution and chip morphology ($G_f = 16$ N/mm, $V_C = 300$ m/min)

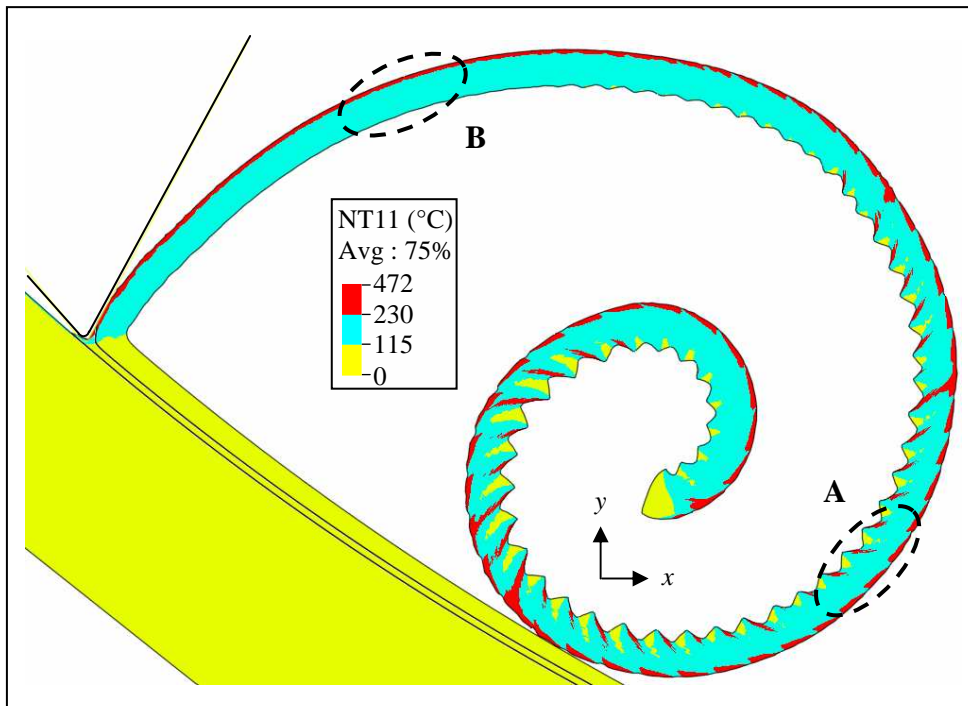


Fig. 2.32 Temperature evolution and chip morphology ($G_f = 16$ N/mm, $V_C = 400$ m/min)

This may evoke possibility of micro crack generation. An undulated surface topology; with clearly marked peak (P) and valley (V) nodes is obtained. This portion of machined workpiece corresponds to segmented chip portion (Fig. 2.32 detail A). While stresses were well below the yield limit in machined workpiece portion corresponding to detail B of Fig. 2.33. A non undulated surface profile was obtained in this case.

Fig. 2.34 presents the residual stress pattern on different patches (corresponding to chip morphology, Fig. 2.32 A and B) of machined workpiece. Intensity of residual stresses in tool advance direction (S_{11}) and perpendicular to tool advance (S_{22}) are different on these peak and valley nodes. Figure depicts, that stresses are generally compressive in nature, and are below yield strength of material, except at some nodes. These could evoke material failure (initiation of small surface cracks).

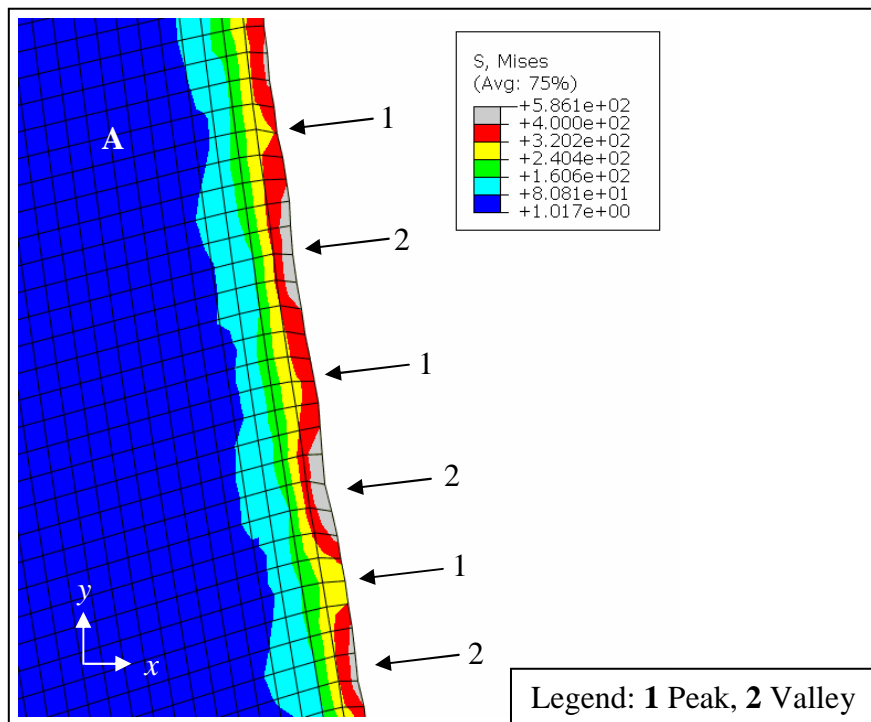


Fig. 2.33 von Mises stress distribution on machined surface corresponding to segmented chip morphology obtained at $V_C = 400$ m/min

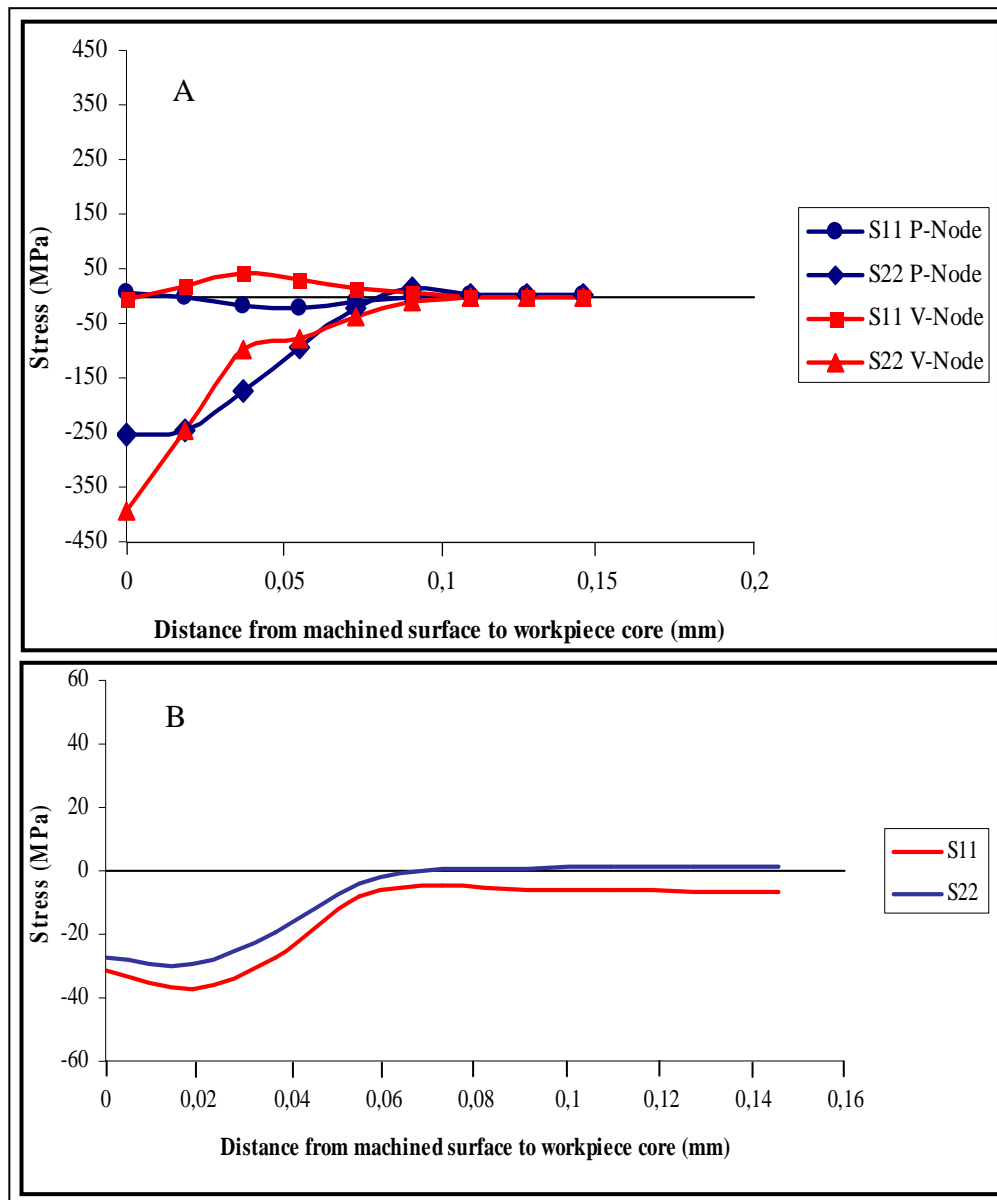


Fig. 2.34 Residual stress distribution from machined surface to workpiece core corresponding to chip morphology obtained at $V_C = 400$ m/min

2.8 Conclusions

In this chapter we have presented a study which concerns the comprehension of physical phenomena accompanying chip formation process. The cases of orthogonal turning and down cut milling have been discussed. The material studied is an aeronautic Aluminium alloy referenced as A2024-T351. The main objective of the work was to introduce a finite-element-based methodology, which explains an original approach concerning the coupling between

material damage and its fracture energy. To validate this numerical approach, an experimental procedure had also been established (in orthogonal turning case). The experimental results show that the higher the cutting speed, the more marked the segmentation geometry. This can imply chip fragmentation in the chip zones where the segments are deeper.

The chip visualizations demonstrate that fragmentation occurs just after the chip evacuation and not at the tool tip as it can be intuitively assumed. The numerical results explain that this fragmentation, happening in the sharpest teeth zone, is the result of the bending loads caused by the effect of tool advance and chip–workpiece contact, simultaneously. Indeed, when the chip curled up, the inner zone of the chip obtained numerically shows narrower segments especially in the zones where the chip presents small curvature radii. This result is qualitatively similar to that obtained experimentally. Therefore, as the chip is even rolled up, the segments are closed again. From the industrial point of view, chip fragmentation is a phenomenon sought to avoid the rolling-up of this chip on a machined surface and to avoid consequently additional micro geometrical defects. A comparison between computed and measured cutting force for given similar cutting conditions shows that the numerical results are close to experimental ones.

It is also noted, on the one hand for a fixed cutting speed, the higher the feed rate, the higher the cutting force. On the other hand, for a fixed value of feed rate, the higher the cutting speed, the fairly constant the cutting force value. The numerical simulation shows clearly the manner in which the damage is propagated during tool–workpiece interaction. In the numerical simulations, it can also be underlined that the segmentation periodicity induces a waved machined surface and non uniform residual stress intensity on the machined surface. These directly dictate the structural and surface integrity of the machined workpiece.

Once the numerical model for orthogonal turning was established and validated experimentally, it was exploited for the case of orthogonal milling process. The objective was to study the evolution of chip morphology during milling process and its eventual effects on surface integrity. Sensitivity of fracture energy G_f on chip morphology has also been studied. Globally, it has been found that a fairly coarse mesh can capture localised deformation phenomena; leading to segmented chip morphology, if an appropriate value of fracture energy G_f is used.

The proposed material damage and fracture energy coupling approach appears to be suitable for cutting simulation. This was proved via the close corroboration obtained between the experimental and numerical results.

3 Concept and Methodology for Micro Cutting Modelling

3.1 Introduction

The present chapter focuses on micro level cutting operations. The objective is to establish a physical based model that is suitable to simulate macro-to-micro scale chip formation process and can efficiently capture the scaling phenomenon (size effect) at micro scale cutting. Following a review on the size effect phenomenon related to micro cutting.

In the domain of micro cutting processes, precious scientific researches have been made in the past for the physical comprehension of the size effect phenomenon. The term “size effect” is usually attributed to define the nonlinear increase in the specific cutting energy (SCE) when UCT decreases from macro scale to few microns. Numerous experimental and numerical studies have been dedicated to explain this scaling phenomenon. Indeed, the investigations have shown that there are multiple factors that can increase material strength and contribute to the size effect in micro machining operations. From the material point of view, Backer et al. [BAC52] had attributed the reason of size effect to the reduction in material imperfections when deformation takes place on small volume. While, Larsen-Basse and Oxley [LAR73] had highlighted the importance of the increase in strain rate in primary shear zone with decrease in UCT, as the principal cause in increasing material strength. Dinesh et al. [DIN01] explain the increase in hardness of metallic materials with decrease in deformation depth, as the consequence of the strong dependence of flow stress on strain gradient in the deformation zone. Based on their work Joshi and Melkote [JOS04] had presented the analytical model for orthogonal cutting incorporating strain gradient effects in material constitutive law. This model was afterwards used by Xinmin et al. [XIN08] in their finite elements model for micro cutting simulations.

It has also been reported in previous researches that the cutting tool edge radius is the major cause of size effect [NAK68, KIM99a, YEN04]. In this regard Nakayama and Tamura [NAK68] believe that, as UCT is reduced to micron level, tool edge radius become comparable or many times greater than chip thickness. Under these conditions, shear plane angle becomes very small leading to greater energy dissipations with plastic flow in the workpiece subsurface. Liu and Melkote [LIU07] has recently shown in their numerical work that plastic shear zones are more expanded and widened when cutting with a sharp tool. This in turn requires higher energy dissipation, contributing to size effect. Other researches believe in the existence of ploughing forces associated with the frictional rubbing and ploughing mechanism as the main reason of the increase in SCE with decrease in the UCT [WU88, END95, WAL96]. Some researches had attributed the size effect to the increase in shear strength of the workpiece material due to a decrease in tool-chip interface temperature as UCT decreases [KIM99b, MAR01, LIU06]. In this context, Liu and Melkote [LIU06] has shown in their recent micro cutting simulation work that the decrease in secondary deformation zone temperature contributes dominantly to considering the size effect as UCT decreases.

In this regard, the present chapter put forwards, a numerical study based on a finite element modelling approach that has been validated experimentally for orthogonal turning process [ASA08, MAB08]. The work highlights the dominance of strain rate hardening characteristics of a strain rate dependent material, in increasing material strength, as UCT decreases from macro to micro level dimensions, during down-cut milling process. Further, to study the contribution of strain gradient (known as a major contributing phenomenon in material strengthening in micro cutting operations) on size effect under high cutting speeds, a modified Johnson-cook constitutive model including strain gradient plasticity [XIN08] are formulated in ABAQUS[®]/EXPLICIT via the elaboration of a user subroutine VUMAT. In addition, milling experiments have been performed to compare the results of SCE evolutions and chip morphology.

3.2 Modelling methodology

3.2.1 Geometrical model and hypothesis

To improve physical comprehension of chip formation process during the milling of an Aluminium alloy A2024-T351, the capabilities of ABAQUS[®] software (version 6.7.1) in its explicit approach were exploited. For accurate measurement of cutting forces, 3D complex

milling insert geometry needs to be taken into account. However, for 2D numerical simulation of milling process, it is a bit difficult to take all factors into account, simultaneously. To simplify the process to a 2D case many factors might be ignored and assumptions could be made. For the present study, following assumptions were made:

- Helix angle for the used insert is small, $\lambda_s = 9^\circ$. This angle does not affect too much F_z (force component along tool axis of rotation). For all cutting speeds, F_z was noted less than 10% of F_{tot} , and can be ignored. Therefore, axial depth of cut (workpiece thickness, $a_p = 4$ mm) may be assumed as constant. This simplifies 3D complicated milling process to a 2D case.
- The diameter of milling tool ($D_T = 22$ mm) and workpiece dimensions are considered greater than the deformation area (chip and tool path zone). Therefore, the deformed area can be assumed as a kind of orthogonal machining process (Fig. 3.1).

In the present case of down cut milling, the conceived FE model was based on quadrilateral continuum elements CPE4RT (with an optimal mesh (15–40) μm in various parts of workpiece) with which it was possible to perform a coupled temperature–displacement calculations. A relatively lower value of feed rate f , when compared with the axial cutting depth a_p , had allowed to adopt plane strain assumptions.

The contact algorithm between tool and workpiece used is the same as been explained in chapter 2 (section 2.3.2). For the present numerical study the macro milling tool is exactly the same as that used in experimentation (shown later in section 3.3) with rake angle of 30° and flank (or clearance) angle of 11° . Tool is modelled as a rigid body and all the boundary conditions are applied to its reference point represented by its centre of rotation. So, that it can advance with a feed velocity V_f in the negative x-axis direction and rotates in anti-clockwise direction with instantaneous angular velocity ω_r . The rest of degrees of freedom are blocked for tool motion. In the present work cutting speeds 200, 400, 600 and 800 m/min have been used for a fixed feed rate of 0.2 mm/teeth. As the tool rotates and advances, simultaneously, the cutter traces a trochoidal path. This produces a variable section chip. Trochoidal path set of equations (chapter 2) was used to model the milling-cutter path zone (chip separation zone) and chip section geometry.

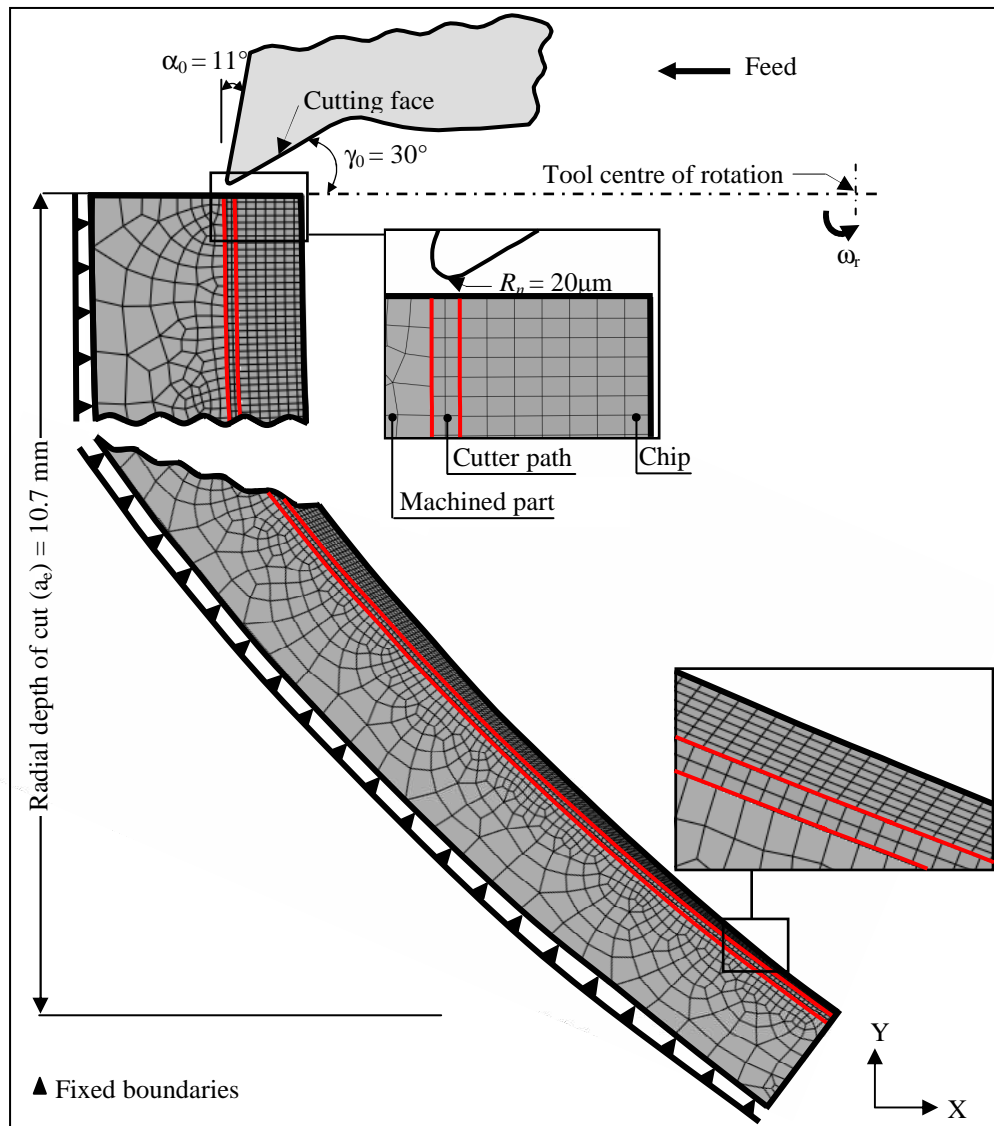


Fig. 3.1 Tool workpiece geometrical model and boundary conditions for down-cut milling

3.2.2 Material behaviour law

The constitutive material and damage models (Johnson-Cook ductile shear failure model) without considering micro-cutting size effect are those presented in chapter 2. While in order to take into account the pre-cited effect, our model for micro machining case is based on Xinmin et al. [XIN08] work. The authors believe that as conventional FE analysis is a non-dimensional, where flow stress is independent from the scale variable. Therefore, it cannot be used to describe the size effect occurring at micro scales. For that, these researchers have developed a constitutive model for orthogonal machining case, considering size effect by introducing a size variable L_p into the conventional material model (JC model).

The framework of their proposed constitutive equation is expressed as:

$$\sigma = f(\sigma_{ref}, \eta) \quad (3.1)$$

Where σ_{ref} is identical to σ_{JC} in the present study and η is the effective plastic strain gradient; a function of the length of the primary shear zone, L_P (for orthogonal machining case). In fact it is the size variable. When L_P reaches a macro level stress flow σ will be identical to σ_{JC} .

The pre-cited formulation aims to establish a relationship between the size variable L_P and the flow stress, and keep the characteristics of JC model as well. Xinmin et al. [XIN08] new constitutive material model for orthogonal machining is mainly based on the Taylor dislocation density model [TAY34]. He was the first physicist who realized that plastic deformation could be explained in terms of the theory of dislocations. His model is the basis of mechanism-based strain gradient plasticity theories e.g. Gao et al [GAO99] and Huang et al [HUA04]. For a polycrystalline material, the Taylor dislocation model gives the shear flow τ in terms of the total dislocation density ρ_T by:

$$\tau = \alpha G b \sqrt{\rho_T} \quad (3.2)$$

Where G is the shear modulus, b is the magnitude of Burgers vector and α is an empirical coefficient varying between 0.3 and 0.5 [ASH70, KOC03]. The total dislocation density ρ_T characterising the material hardening is the sum of two densities as flows:

$$\rho_T = \rho_s + \rho_g \quad (3.3)$$

Where ρ_s characterises the Statistically Stored Dislocations (SSD), which is determined by the material test in the absence of strain gradient consideration according to the following equation:

$$\rho_s = \left(\frac{\sigma_{ref}}{M_t \alpha G b} \right)^2 \quad (3.4)$$

The tensile flow stress σ is related to the shear flow stress τ by:

$$\sigma = M_t \tau \quad (3.5)$$

Where M_t is the Taylor factor which acts as an isotropic interpretation of the crystalline anisotropy at the continuum level. For FCC as well as for BCC metals that slip on $\{110\}$ planes M is taken as 3.06 [BIS51, KOC70] and $\sqrt{3}$ for an isotropic solid [LIU05].

Whereas, ρ_g concerns the Geometrically Necessary Dislocations (GND), which are required for compatible deformation of various parts of the non-uniformly deformed material [FLE94]. Indeed, when heterogeneities of different plastic resistance are introduced into a smooth

dislocation flux, as may occur with alloys containing non-deformable precipitates or particles, or when grains of different relative orientation must deform together compatibly as in polycrystals, local “turbulences” occur. Such occurrences are ubiquitous in all cases other than unconstrained single crystals subjected to uniform shear flow. The additional local deformations that are required for compatibility make important changes in the plastic resistance and strain-hardening rate in such heterogeneous materials. Now, the plastic resistance and the hardening rate depend on a local material length scale characterizing the range of the perturbation in the flow, such as the particle size, particle mean spacing, or grain size. Ashby [ASH70] pioneered the consideration of such problems in crystal plasticity, where the nature of the basic constitutive relation is altered beyond mere considerations of the volume fractions of components of different resistance as would be the case in macroscopic composites. The central concept from which such phenomena is started is the disruption of smooth dislocation fluxes by local, more or less intense, strain gradients imposed by the heterogeneities, where the displacement incompatibilities must be accommodated locally by GNDs, which in turn, interact in various ways with the otherwise smooth dislocation flux [ARG08]. It is these GNDs and their effects on the flow stress that are considered in the present study. The tensile flow stress σ in terms of dislocation densities can be expressed as:

$$\sigma = M_t \alpha G b \sqrt{\rho_s + \rho_g} \quad (3.6)$$

According to Ashby [ASH70] the total density of dislocations ρ_T , which is given by the sum of statistically stored and geometrically necessary dislocations, is a special case of the following equation:

$$\rho_T^\chi = \rho_s^\chi + \rho_g^\chi \text{ for } \chi = 1 \quad (3.7)$$

To properly estimate ρ_T , Ashby has proposed that the exponent χ should be less than or equal to 1. Joshi and Melkote [JOS04] believe that, due to large strain gradients commonly met in machining, a lower value of χ is reasonable to introduce in Eq. 3.7. So, in the general case the material flow stress can be given by:

$$\sigma = M_t \alpha G b \sqrt{\rho_s^\chi + \rho_g^\chi} \quad (3.8)$$

Substituting Eq. 3.4 into Eq. 3.8, the flow stress can be written as:

$$\sigma = \sigma_{ref} \sqrt{1 + \left(\frac{\rho_g}{\rho_s} \right)^\chi} \quad (3.9)$$

The density of geometrically necessary dislocations ρ_g is related to the gradient of plastic strain by [ASH70, NIX98, HUA00]:

$$\rho_g = \bar{r} \frac{\eta}{b} \quad (3.10)$$

Where \bar{r} is the Nye factor introduced by Arsenlis and Parks [ARS99] to reflect the effect of crystallography on the distribution of GNDs, and \bar{r} is around 1.90 for FCC polycrystals, 1.85 and 1.93 for bending and torsion, respectively [SHI04]. Joshi and Melkote [JOS04] has totally ignored this effect while calculating the density of GNDs for the case of orthogonal machining. In their model they had considered the existence of geometrically necessary edge dislocations only, while ignoring geometrically necessary screw dislocations (necessary to avoid splitting of elements in a row). Xinmin et al. [XIN08] have considered its value as 2 for the case of machining.

For $M_t = 3.06$ and $\bar{r} = 2$, the constitutive equation turns to be as follows:

$$\sigma = \sigma_{ref} \sqrt{1 + \left(\frac{18\alpha^2 G^2 b \eta}{\sigma_{ref}^2} \right)^\chi} \quad (3.11)$$

As discussed above that σ_{JC} is selected to be σ_{ref} , and then equivalent stress can be written as:

$$\sigma = \sigma_{JC} \sqrt{1 + \left(\frac{18\alpha^2 G^2 b \eta}{\sigma_{JC}^2} \right)^\chi} \quad (3.12)$$

From the works of Joshi and Melkote [JOS04], the strain gradient (SG) is obtained through the dislocation analysis of primary shear zone (while ignoring the existence of GNDs in secondary shear zone) for micro scale machining, as follows:

$$\eta = 1/L_p \quad (3.13)$$

So, the constitutive equation can be expressed as:

$$\sigma = \sigma_{JC} \sqrt{1 + \left(\frac{18\alpha^2 G^2 b}{\sigma_{JC}^2 L_p} \right)^\chi} \quad (3.14)$$

Material parameters used for SG-plasticity model (Eq. 3.14) are given in Table 3.1.

| α | G (GPa) | b (nm) | χ |
|----------|---------|--------|-------------|
| 0.5 | 28 | 0.283 | 0.3 [JOS04] |

Table 3.1 Material properties used for SG-plasticity based model [XUE02]

To calculate the length of primary shear zone L_p in micro-scale machining, minimum chip thickness h_{min} has significant impact, especially when the UCT is close to micro cutter edge radius. On these occasions, the machining process can be divided into two situations: chip formation and no chip formation. Kim [KIM04a] studied this phenomenon using molecular dynamic (MD) simulation, as shown in Fig. 3.2.

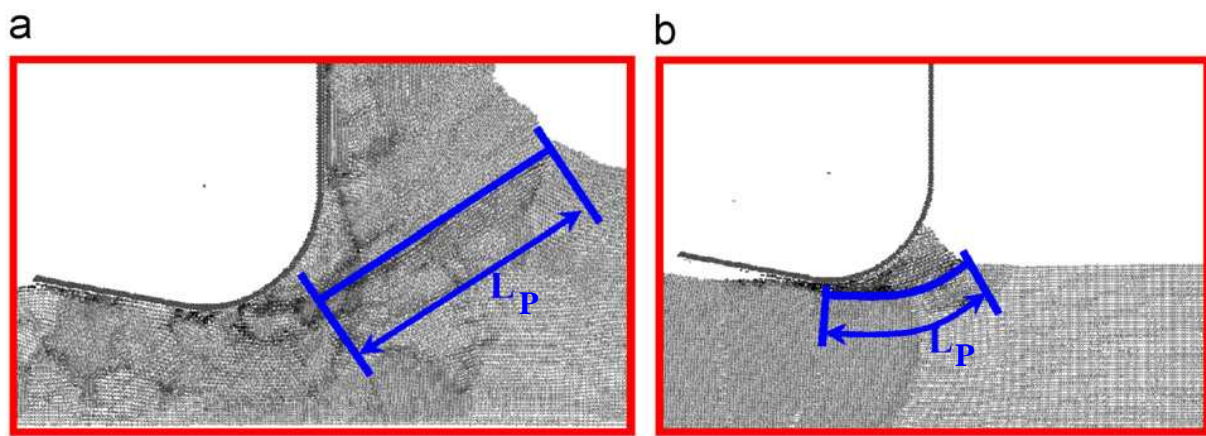


Fig. 3.2 Chip formation with regard of cutter edge radius (a) Chip formed (b) no chip formed [KIM04a]

Xinmin et al. [XIN08] and Vogler et al. [VOG04] had reported in their work that, h_{min} for OFHC copper is 0.25-0.35 R_n (cutter edge radius). For the situation that chip forms when $h \geq h_{min}$, as shown in Fig. 3.2a, the length of shear zone can be obtained by the cutting principles [SHA84]:

$$L_p = \frac{h}{\sin \phi} \quad (3.15)$$

For the case of milling as h varies with time t , Eq. 3.15 can be rewritten as:

$$L_p = \frac{h(t)}{\sin \phi} \quad (3.16)$$

Where

$$\phi = \pi/4 + \left(\frac{\gamma - \beta}{2} \right), \beta = \tan^{-1} \mu \quad (3.17)$$

For the situation when no chip formation as shown in Fig. 3.2b, when $h < h_{min}$, the shear angle becomes very small and chip thickness does not exist. Therefore, Eq. 3.15 is not applicable any more. Through the analysis of shear zone, the arc length of contact part is proposed to be the length of primary shear zone.

$$L_p = \frac{\arccos\left(\frac{R_n - h}{R_n}\right) \pi R_n}{180} \quad (3.18)$$

Hence, the constitutive equation can be expressed as follows:

$$\sigma = \sigma(\varepsilon, \dot{\varepsilon}, T, L_p, h_{min}) = \sigma_{JC} \sqrt{1 + \left(\frac{18\alpha^2 G^2 b}{\sigma_{JC}^2 L_p}\right)^\chi} \quad (3.19)$$

For aforementioned formulation, the scale variable is expressed as the shear zone length L_p . Since strain gradient η is the inverse of L_p , it will decrease with the increase of uncut chip thickness. Therefore, the GND will disappear for the large test piece and macro scale machining process. This fully satisfies the constraint condition, that the flow stress is equal to the results by JC model when size variable reaches to macro level (Eq. 3.1).

This physical constitutive model is implemented by exploiting the user subroutine VUMAT of ABAQUS[®]/EXPLICIT. The flow chart of ABAQUS[®]/EXPLICIT user routine VUMAT is shown in Fig. 3.3.

3.2.3 Model validation by numerical elementary tests

Proper functioning of the numerical model with material modelling performed in auxiliary subroutine (VUMAT) needs to be ensured. For this purpose, standard elementary tests on single element must be carried out in order to exploit properly the developed numerical model for the actual cutting simulation. Therefore, we have initially written VUMAT subroutine for JC reference model (Eq. 2.6), with damage initiation and its evolution (Eq. 2.8, 9, 11-14). Elementary tests (extension and simple shear) on CPE4RT elements, for coupled temperature displacement calculations were performed.

Results concerning von Mises stress, equivalent strain, nodal displacement, damage initiation ω and damage evolution parameters D , were compared with those obtained by ABAQUS[®]/EXPLICIT inbuilt constitutive models. Once the VUMAT model is established and validated for the JC material reference model, the constitutive equation including SG (Eq. 3.19) was included.

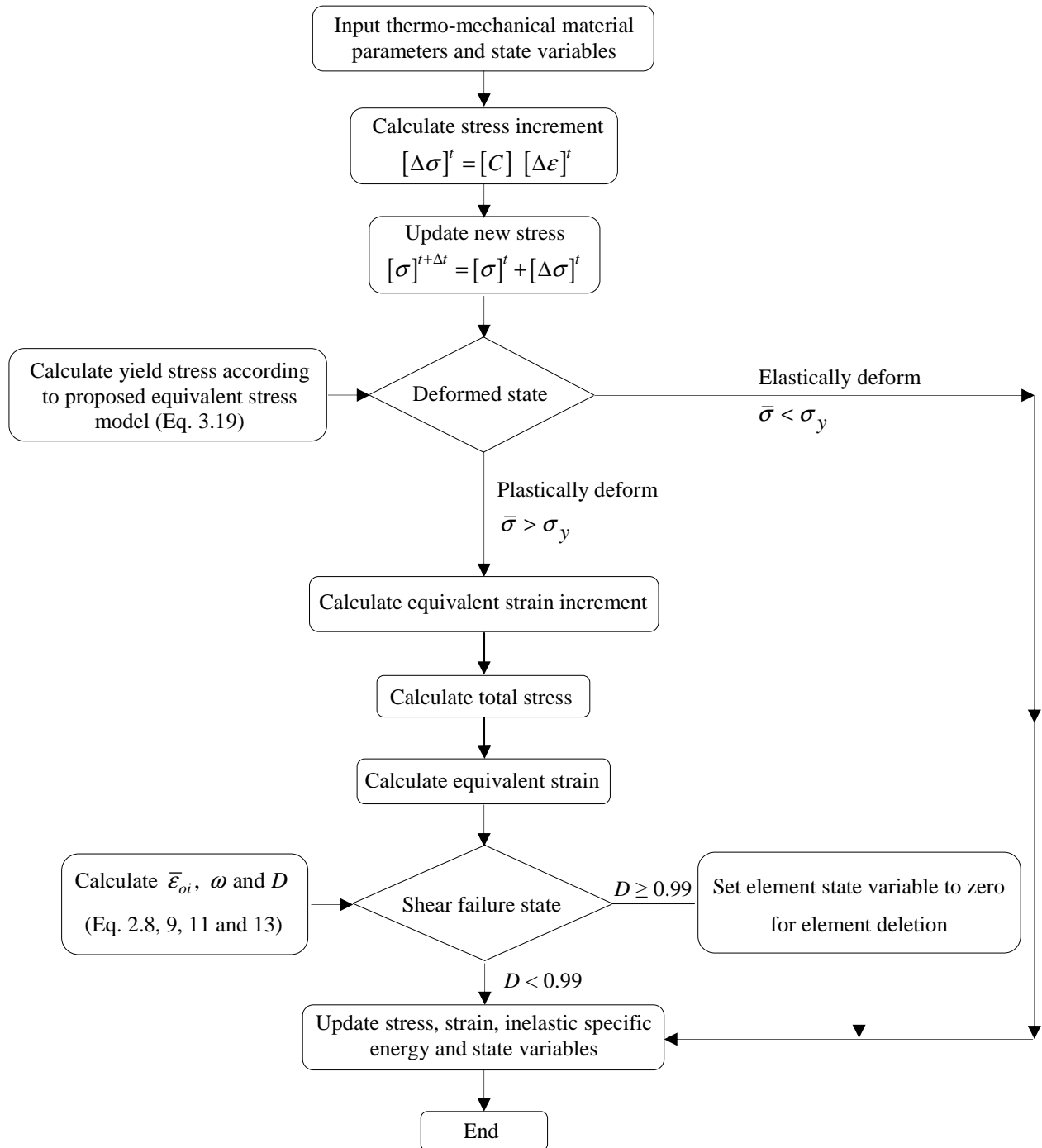


Fig. 3.3 ABAQUS®/EXPLICIT VUMAT programme flow chart developed for the present study

In both, extension and simple shear tests a loading velocity of 1 mm/msec for 1 msec simulation time was performed. Figs. 3.4-3.6 present displacement, von Mises stress and temperature plots for, extension test using VUMAT model (without considering SG-plasticity) and ABAQUS®/EXPLICIT built-in model for JC- material reference model.

Figs. 3.7-3.11 present displacement, von Mises stress, temperature and Scalar damage evolution parameter (exponential and linear) plots for simple shear displacement using VUMAT model (without considering SG-plasticity) and ABAQUS[®]/EXPLICIT built-in model for JC- material model.

Elementary tests show a good agreement (with less than 0.01 % error) between ABAQUS[®]/EXPLICIT built-in model and the elaborated VUMAT user model results. Consequently, the proper functionality of user subroutine VUMAT ABAQUS[®]/EXPLICIT for JC model (Eq. 2.6) is perfectly validated. Afterwards, the modified JC model considering SG (Eq. 3.19) was implemented in the subroutine.

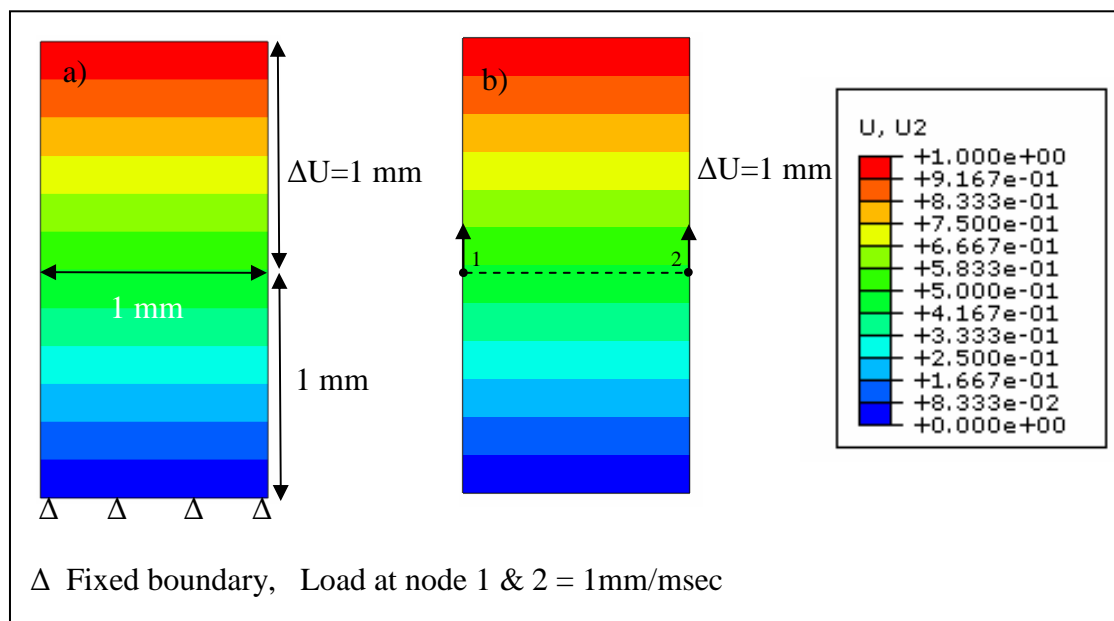


Fig. 3.4 Uni-axial displacement (along y-axis) plot at time = 1 msec a) ABAQUS model b) VUMAT model

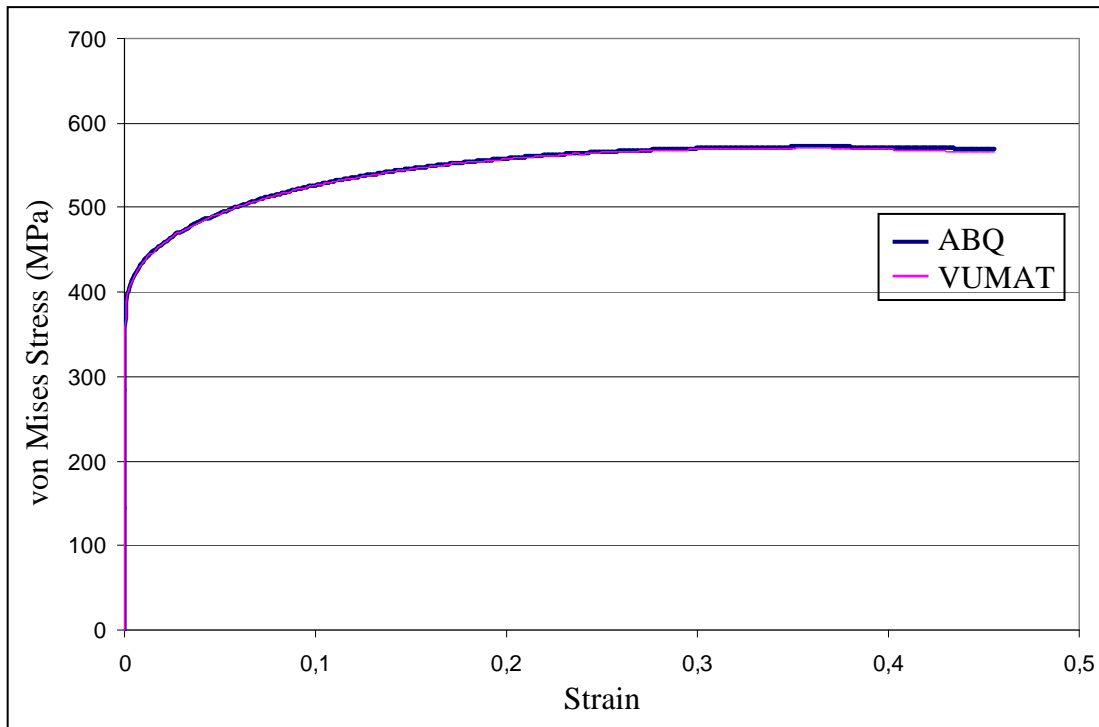


Fig. 3.5 von Mises stress vs equivalent plastic strain curves without damage model (at nodes 1 and 2, shown in Fig. 3.4)

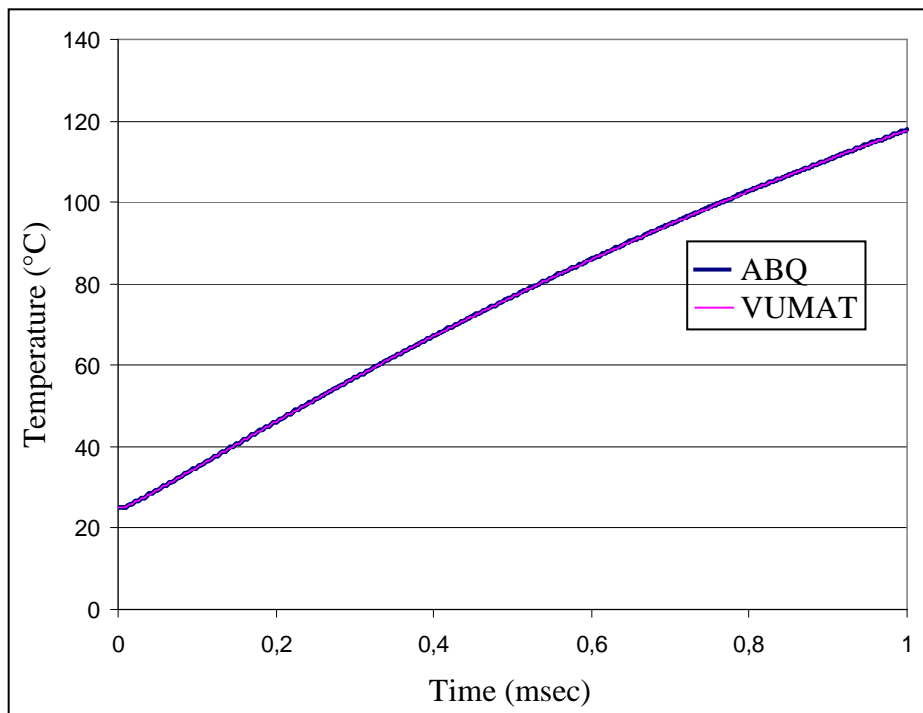


Fig. 3.6 Temperature curves (at nodes 1 and 2, shown in Fig. 3.4)

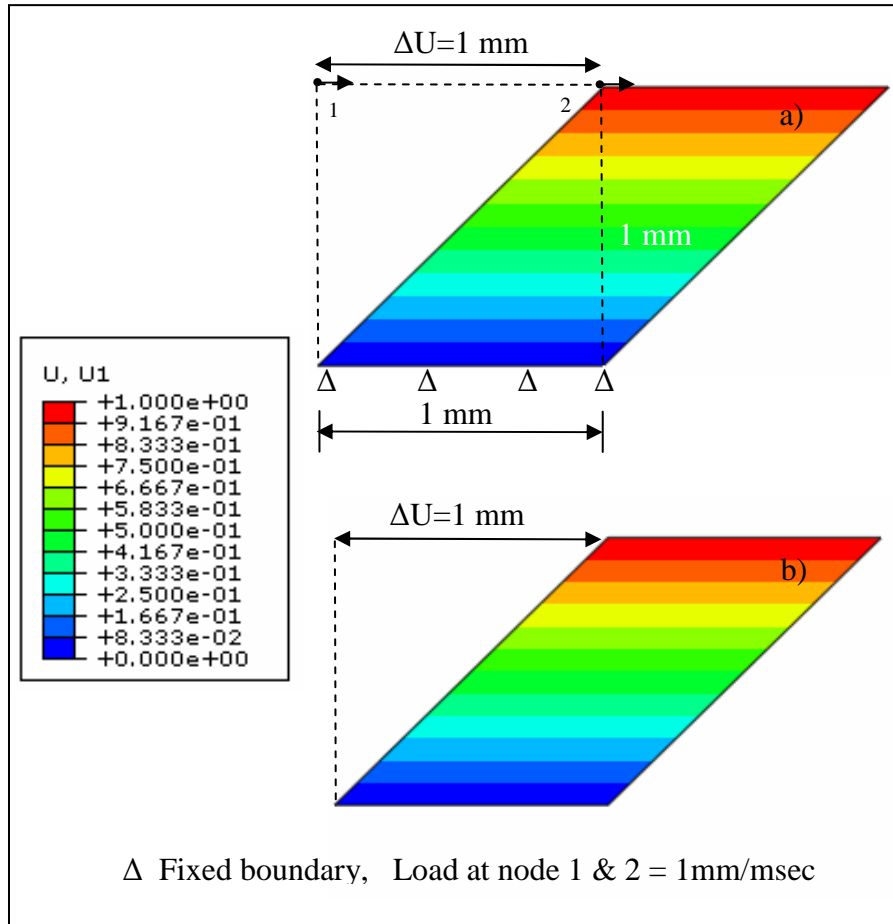


Fig. 3.7 Shear displacement plot at time = 1msec a) ABAQUS model b) VUMAT model

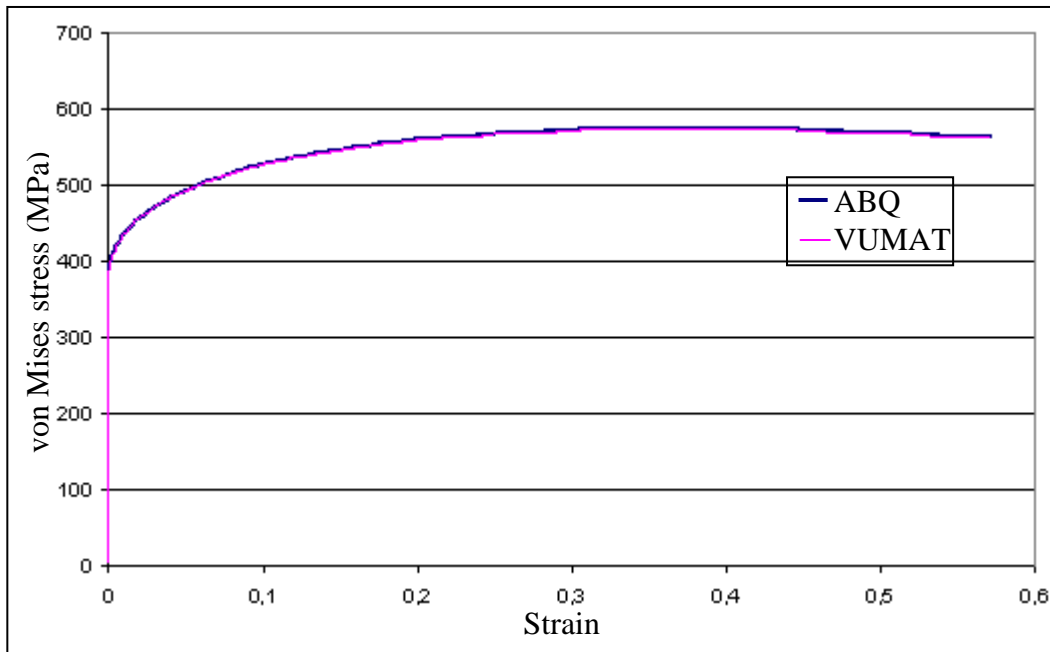


Fig. 3.8 von Mises stress vs equivalent plastic strain curves without damage model (at node 2, shown in Fig. 3.7)

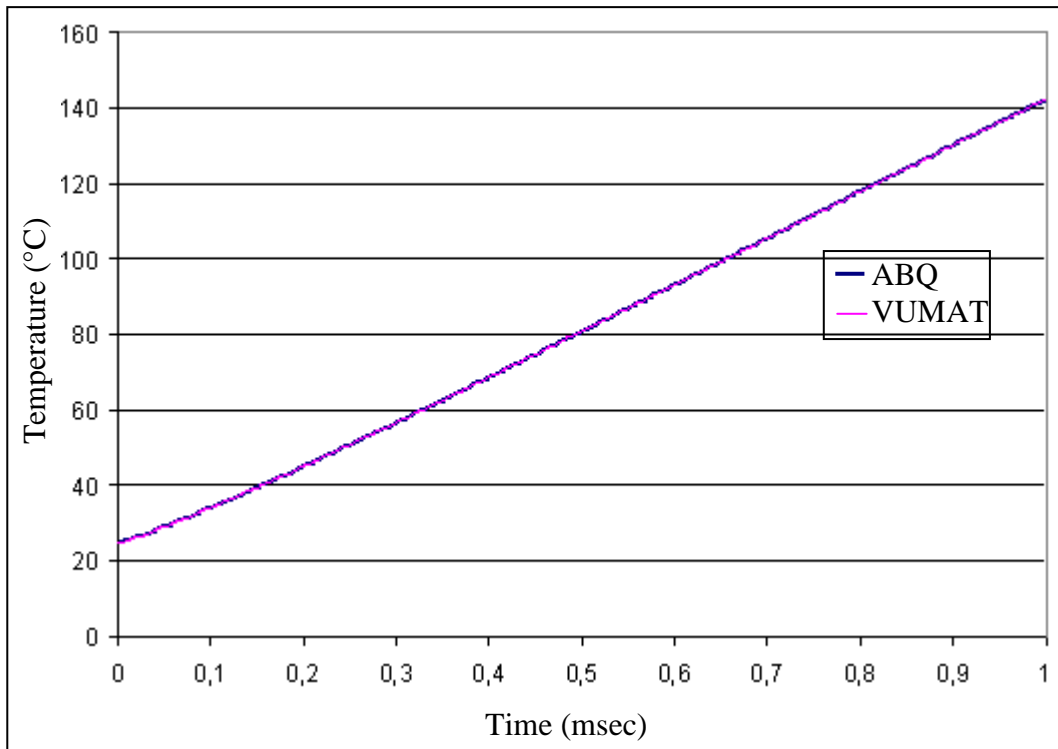


Fig. 3.9 Temperature curves (at node 2, shown in Fig. 3.7)

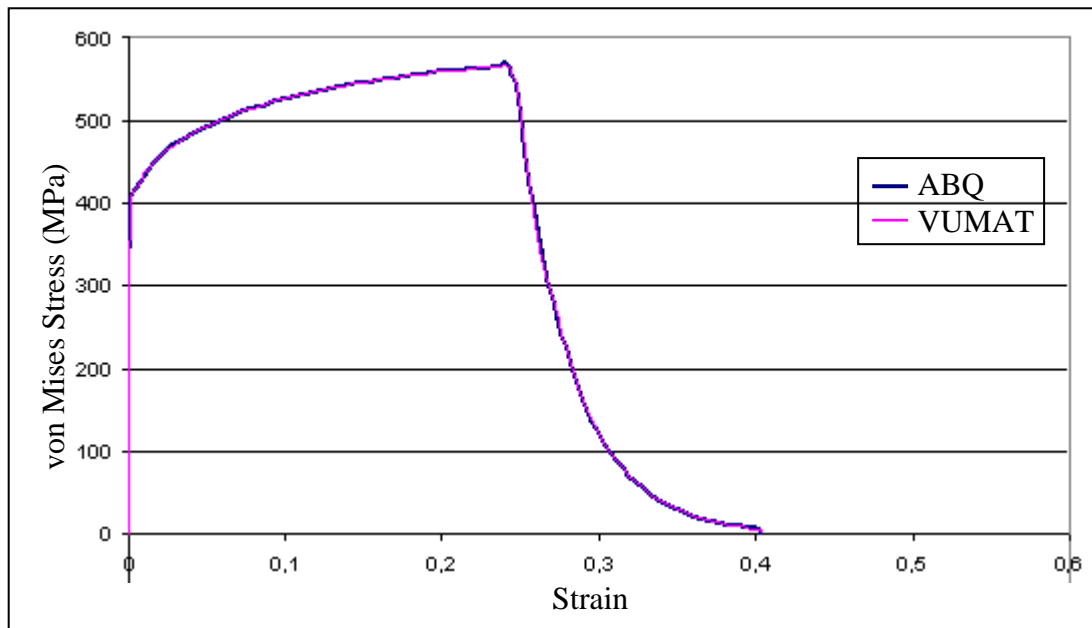


Fig. 3.10 von Mises stress vs equivalent plastic strain curves with exponential damage evolution model for $G_f = 20$ N/mm (at node 2, shown in Fig. 3.7)

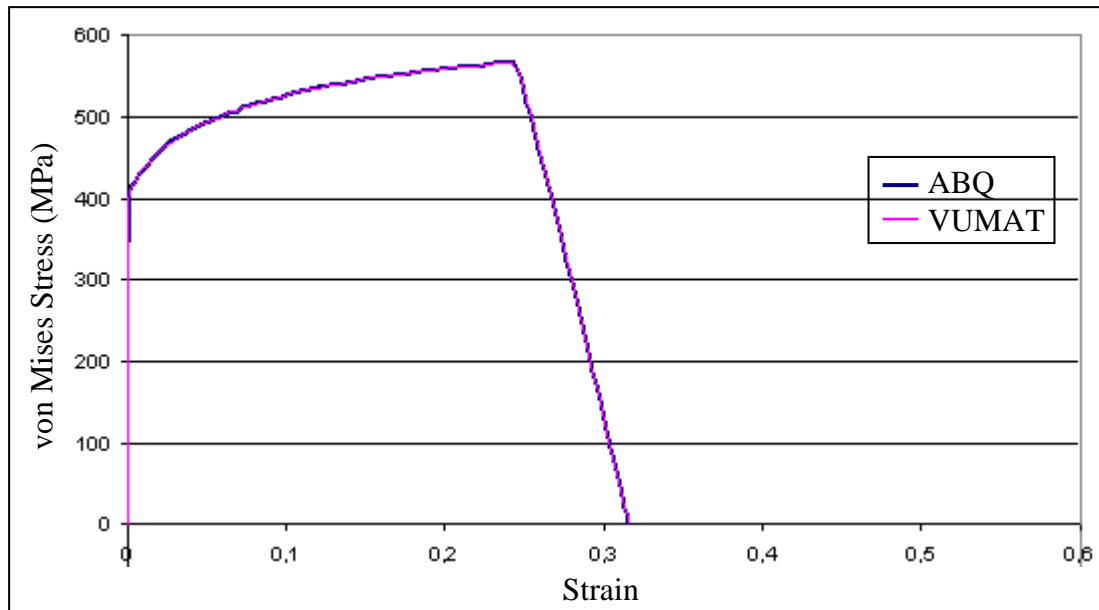


Fig. 3.11 von Mises stress vs equivalent plastic strain curves with linear damage evolution model for $G_f = 20$ N/mm (at node 2, shown in Fig. 3.7)

3.3 Down-cut peripheral milling experiments

Experimental tests were carried out on DMG-3AXIS machining centre. The working parameters adopted concern different cutting speeds: 200, 400 and 600 m/min for a fixed feed rate of 0.2 mm/tooth. A Mitsubishi[®] milling tool of diameter ($D_T = 22$ mm), referenced 223WA20SA, with coated carbide insert referenced AOMT123608PEER-M was used. The insert geometry (Fig. 3.12a) was measured by an optical measuring device. This has helped to generate a 2D geometry of the insert (Fig. 3.12b). This insert profile was afterwards used in the FE milling model (Fig. 3.1).

The machined workpiece is an Aluminium alloy plate A2024-T351 with a thickness of 4 mm fixed on a standard dynamometer Kistler[®] 9257A (Fig. 3.13). The force measuring equipment was composed of the dynamometer, charge amplifiers (Kistler 5015A) and a high-frequency data acquisition device (National Instrument NI 4472). LabView[®] software was used for synchronous signal acquisition on three different channels corresponding to the three orthogonal directions of the dynamometer.

Data treatment developed with Matlab[®] was used to correct dynamic effects in milling case [GIR10]. Finally, cutting forces were transposed in an appropriate base in order to compute the SCE. Experimental setup is resumed in Fig. 3.14. Since the tool had many teeth with little geometric defects, corresponding cutting forces are not exactly similar. Cutting forces

exploited in the following are the mean of efforts according to the three teeth, and uncertainties observed correspond to the differences with extreme values.

Fig. 3.15 shows the force diagram for orthogonal down-cut milling case. From the decomposition of forces, cutting force F_c acting tangentially (similarly to cutting speed) can be calculated by Eq. 3.20.

$$\left. \begin{aligned} \vec{F}_{tot} &= F_x \cdot \vec{x} + F_y \cdot \vec{y} = F_c \cdot \vec{c} + F_r \cdot \vec{r} \\ \vec{F}_{tot} &= (F_x \cdot \sin\theta + F_y \cdot \cos\theta) \cdot \vec{c} + (F_x \cdot \cos\theta - F_y \cdot \sin\theta) \cdot \vec{r} \\ F_c &= F_x \cdot \sin\theta + F_y \cdot \cos\theta \end{aligned} \right\} \quad (3.20)$$

For the calculation of the SCE at various (UCT) (presented here by a value h) values and cutting speeds, Eq. 3.21 can be used. Afterwards experimental results were compared with the corresponding numerical ones.

$$SCE = \frac{F_c}{h \cdot a_p} \quad (3.21)$$

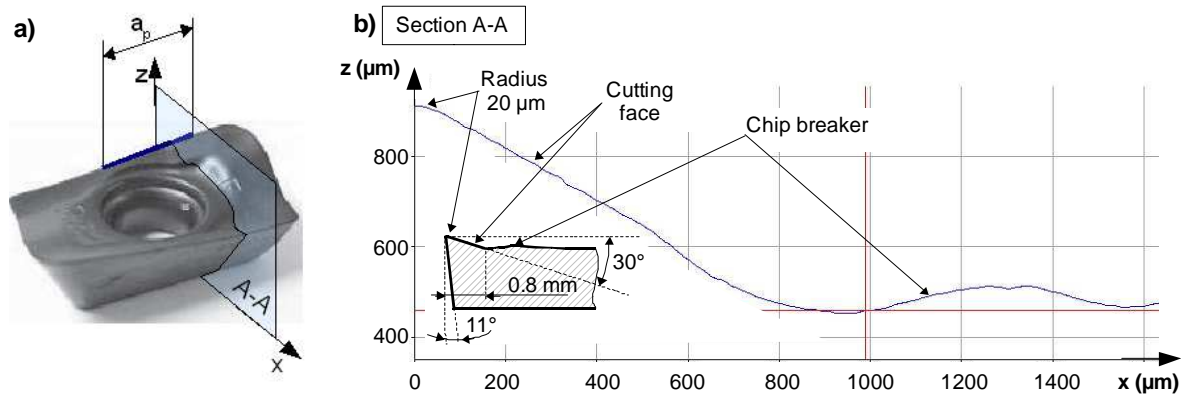


Fig. 3.12 Coated carbide insert referenced AOMT123608PEER-M a) 3D view b) Optical device generated 2D profile

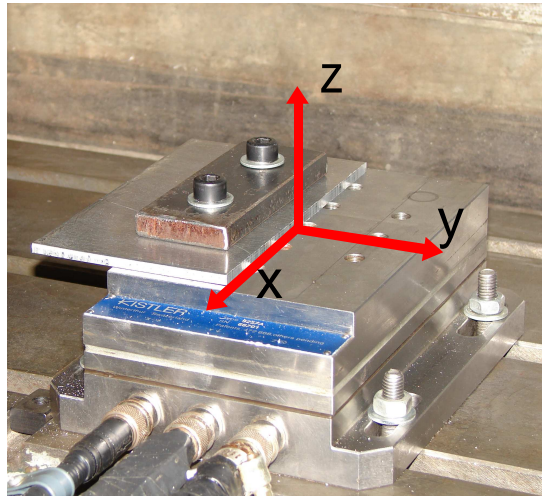


Fig. 3.13 Workpiece mounted on dynamometer

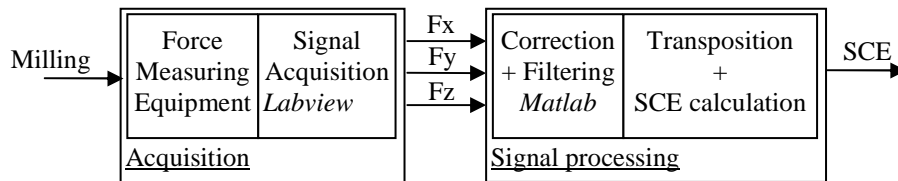


Fig. 3.14 Schematic representation of the experimental set up

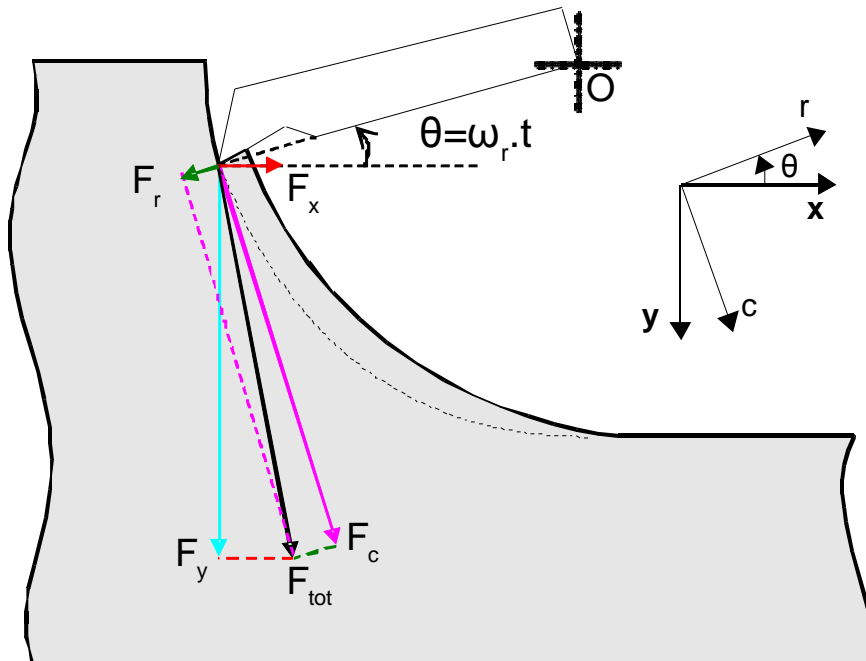


Fig. 3.15 Orthogonal down-cut milling force diagram

3.4 Results and analysis

This section discusses the contribution of various material strengthening factors in capturing size effect for orthogonal down-cut milling process. Numerical simulations at different cutting speeds (200, 400, 600, and 800 m/min) and a fixed feed rate value of 0.2 mm/tooth have been performed.

3.4.1 Temperature effect on material strengthening

To reveal the influence of temperature on size effect, the maximum temperature evolution at the secondary shear zone is calculated at various uncut chip thickness, h (without considering SG) for various cutting speeds (Fig. 3.16). It can be seen that, the lower the UCT, the lower the temperature at the secondary shear zone. However, for a given cutting speed; during the decrease from macro to micro dimensions, the temperature decrease (≈ 35 °C) is not significant enough to cause any considerable contribution in increasing material strength and influencing size effect.

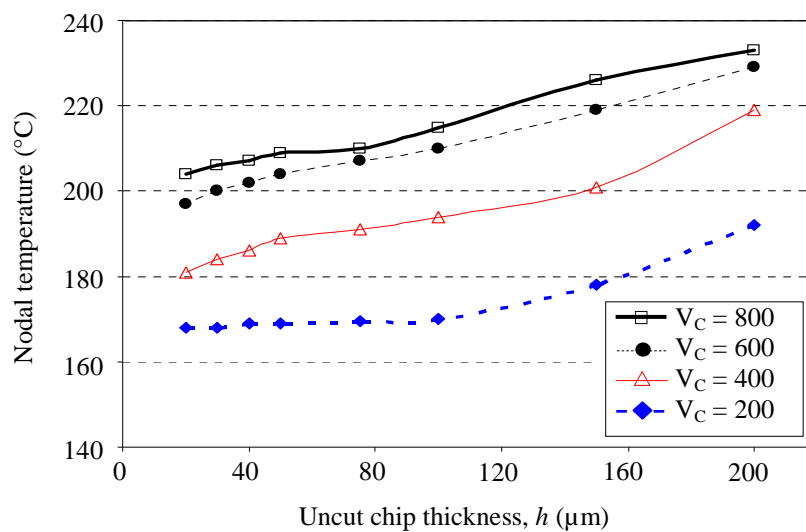


Fig. 3.16 Maximum secondary shear zone temperatures vs uncut chip thickness h for various cutting speeds (w/o SG)

3.4.2 Strain rate effect on material strengthening

Fig. 3.17 shows the plots of SCE for various h values at different cutting speeds without considering SG. The partial capture of size effect observed along the curves traced for all

cutting speeds is apparent. In addition, by increasing the cutting speed up to 800 m/min a relatively higher capture of size effect can be observed.

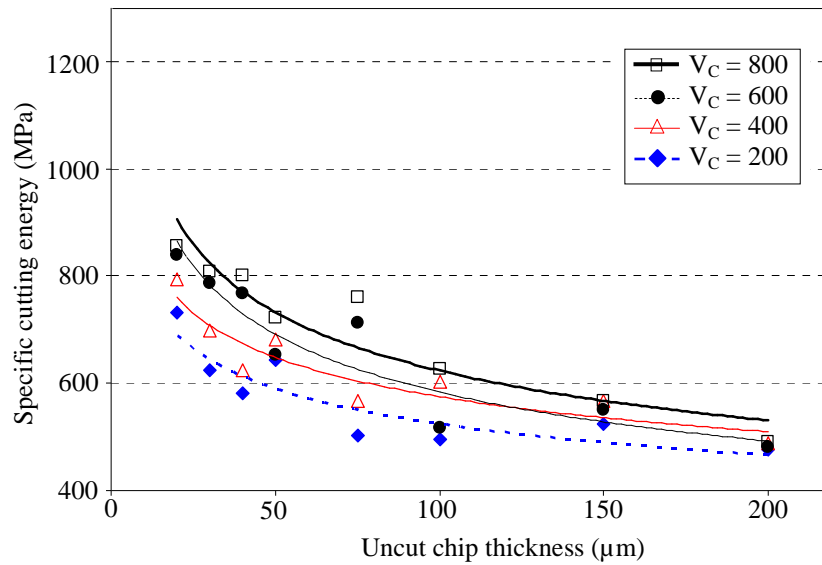


Fig. 3.17 Specific cutting energy evolution at various uncut chip thickness values (w/o SG)

This allows to further investigate the possible existence of a material strengthening mechanism other than SG-strengthening, tool edge radius effect (kept constant in this study) and temperature strengthening effects (not significant for the studied material as shown in subsection 3.4.1). Therefore, numerical results without considering SG concerning chip morphology were closely analysed at tool-chip interface for various h values.

Fig. 3.18 represents the simulated rake face-chip contact length L_C evolution at $V_C = 200$ m/min. Initially, it can be seen that the lower the UCT values, the lower the L_C ones. Afterwards, L_C starts to increase as h value further decreases toward micron level. A similar trend was observed when numerical simulations were performed for higher cutting speeds as shown in Fig. 3.19. In fact shear angle decreases as UCT decreases [ATK03], further because of strain rate hardening, material strengthens. Under these conditions chip has tendency to straighten up rather than bend, so L_C increases.

Nevertheless, chip contact length values were higher at analogous UCT values for higher cutting speed. This nonlinear increase in contact lengths at small h values implies that a higher energy is dissipated during frictional interaction at tool-workpiece interface, which yields to higher SCE. This provides an explanation for the partial capture of size effect even without considering SG-strengthening as it was demonstrated in Fig. 3.17. This trend of increase in rake face-chip contact lengths is consistent with the results of Liu and Melkote

[LIU07], when a sharp tool is replaced by an edge radius tool. As, tool edge radius was unchanged for all cutting simulations, therefore this increase in tool-chip contact lengths at smaller h values, resulting in higher SCE can be attributed to highly strain rate dependent properties of the studied material.

Simultaneously, it is noticeable that length scale (in term of uncut chip thickness) at which L_C starts to increase; for lower h values, varies with cutting speeds. Indeed, when V_C evolves from 200 to (400, 600 and 800) m/min, h value increases from 44 to (46, 48 and 60) μm , respectively. In his research work, Kountanya [KOU02] has noted this length value (value at which curvature of SCE curve is maximum) as 42.1 μm for $V_C = 56.4$ m/min on the same material studied in the present work.

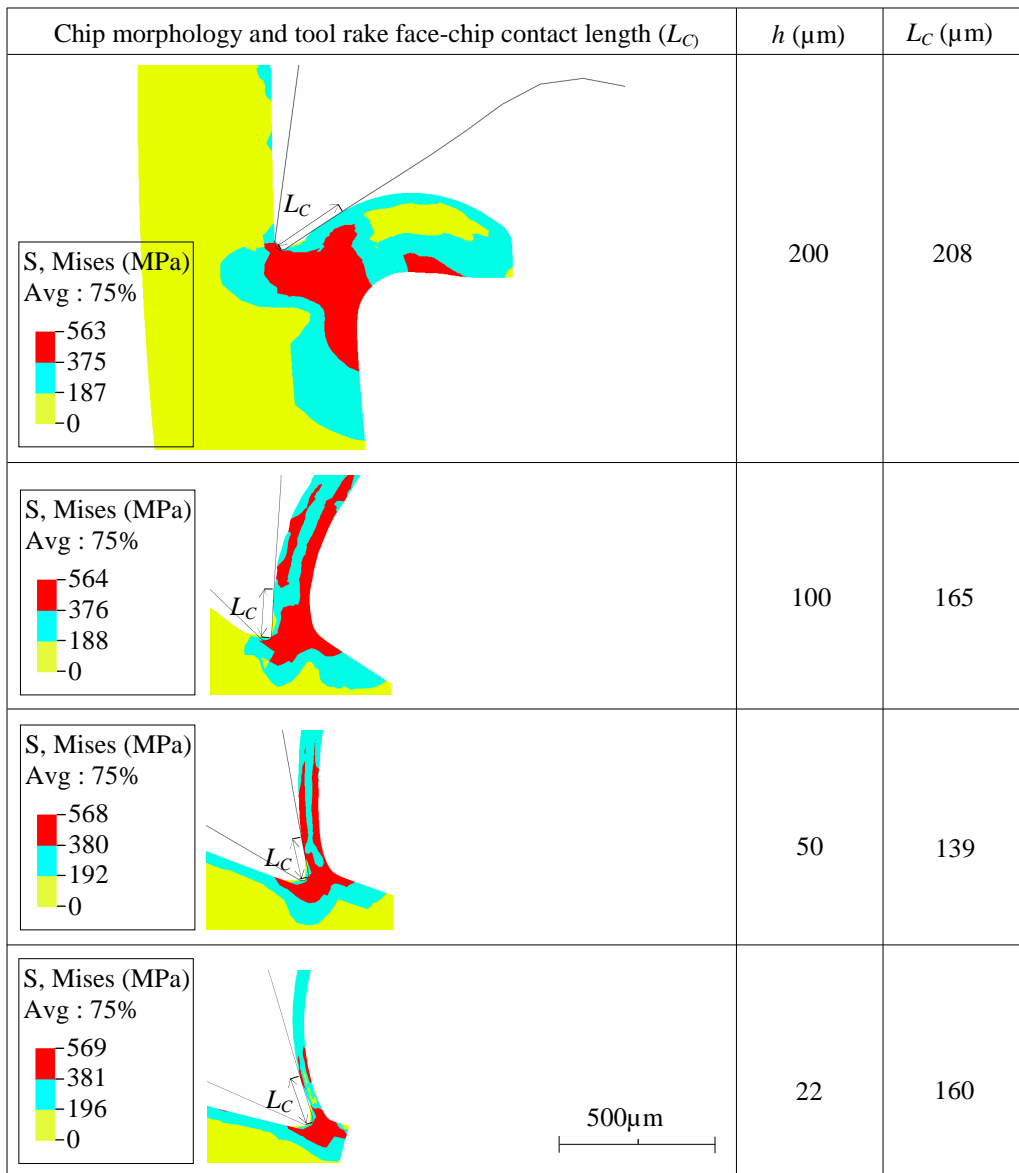


Fig. 3.18 Simulated tool rake face-chip contact length (μm) for $V_C = 200$ m/min (w/o SG)

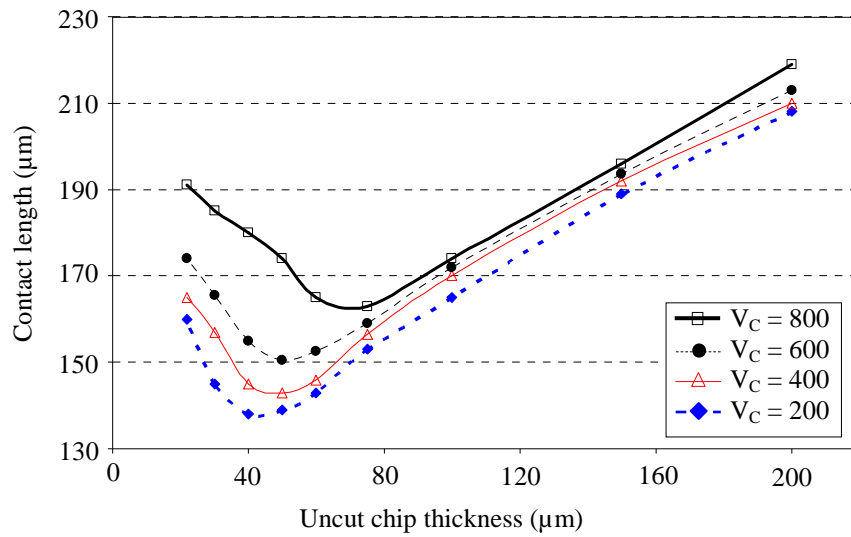


Fig. 3.19 Simulated tool rake face-chip contact lengths (w/o SG) at various uncut chip thickness for various cutting speeds

An insight analysis of both Fig. 3.19 and the result of Kountanya [KOU02] show that the length scale increases with cutting speed, however this increase is remarkable for higher cutting speeds (≥ 800 m/min). This is consistent with the findings of Liu and Melkote [LIU07], though they have attributed the increase in the length scale to the temperature drop in secondary shear zone for a strain rate insensitive Aluminium alloy Al5083-H116.

It can be deduced from above discussion that, independent of material properties the higher the cutting speed, the higher the nonlinear length scale (in term of uncut chip thickness). Though the reasons of this increase could be different; either temperature drop in secondary shear zone for a strain rate insensitive material [LIU07] or strain hardening properties of a strain rate sensitive material.

3.4.3 Strain gradient effect on material strengthening

Further, to study the contribution of SG-strengthening on size effect for strain rate sensitive material, cutting simulations considering SG-model (Eq. 3.19) were performed for various cutting speeds.

Fig. 3.20 presents the SCE plots with and without considering SG-effects for various h values at different cutting speeds. It can be noted that the SCE values computed in the case of a simulation considering SG are closer to experimental ones than that calculated without considering SG. This proves that the modified JC law (Eq. 3.19) based on Taylor model

allows a good estimation of the cutting force during the variation of the UCT from macro to micro level. Moreover, for lower uncut chip thickness, the modified JC law permits to capture the nonlinear increase in SCE whose evolution is more pronounced than that calculated without considering SG.

However, it is interesting to remark that the difference of results in Fig. 3.20 even at large UCT values (200 μm) with and without using strain gradient model is still very large. However, this difference (at UCT = 200 μm) becomes negligible if compared with the one obtained at very small values of UCT (where specific cutting energy increases exponentially [XIN08, LIU06]) around $0.25R_n = 5\mu\text{m}$ or even lesser, while in present study simulations are run up to 22 μm . This helps to infer that physical significance of this model mainly starts at UCT values of the order of R_n (tool edge radius) and below.

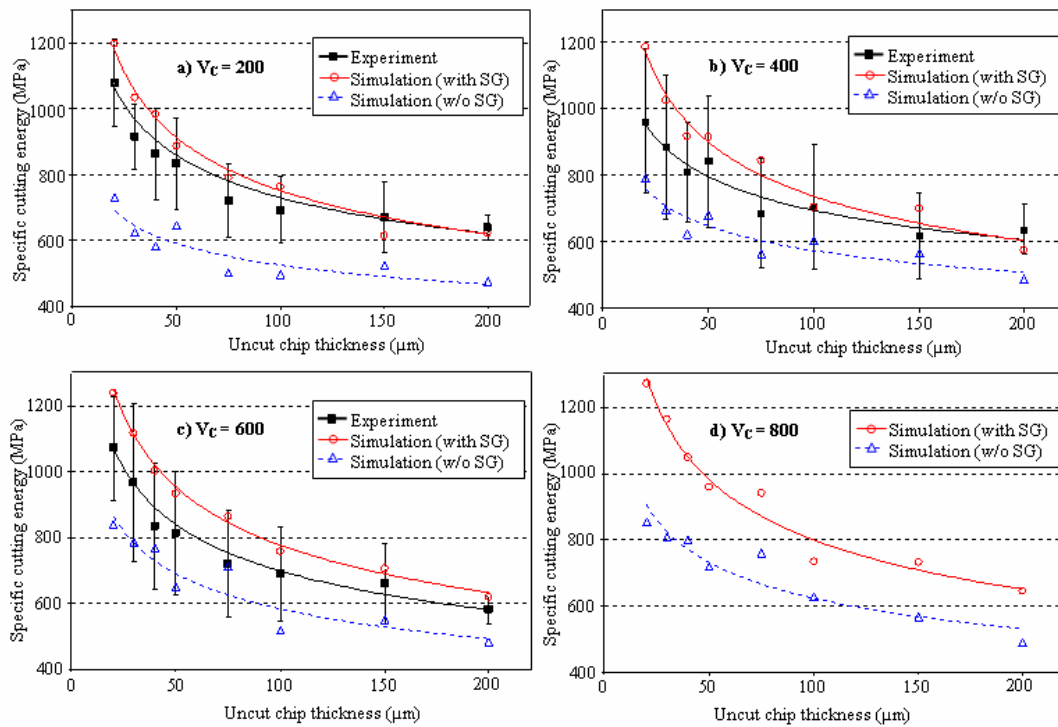


Fig. 3.20 Specific cutting energy evolution for various uncut chip thickness values at different cutting speeds (at $V_C = 800$ m/min forces were not registered)

Fig. 3.21 shows the von Mises stress plot for cutting speed of 200 m/min. Globally, the chip morphologies with and without considering SG-strengthening effects present a certain similarity and are comparable with the experimental one (Fig. 3.22).

From stress point of view, it can be observed that by introducing SG-effects in the material model, and when the cutting speed is equal to 200 m/min, the maximum von Mises stresses

have been increased from 569 MPa to 610 MPa. Whereas, for a higher cutting speed of 800 m/min (Fig. 3.23) maximum stresses were increased from 586 MPa to 653 MPa. The increments in stress magnitude for both cutting speeds are comparable, approximately.

Consequently, this suggests that strain gradient hardening is the dominant phenomenon for material strengthening at high cutting speeds and lower h values for a strain rate dependant material. To fully capture the size effect for micro cutting operations, SG-based strengthening mechanism is inevitable.

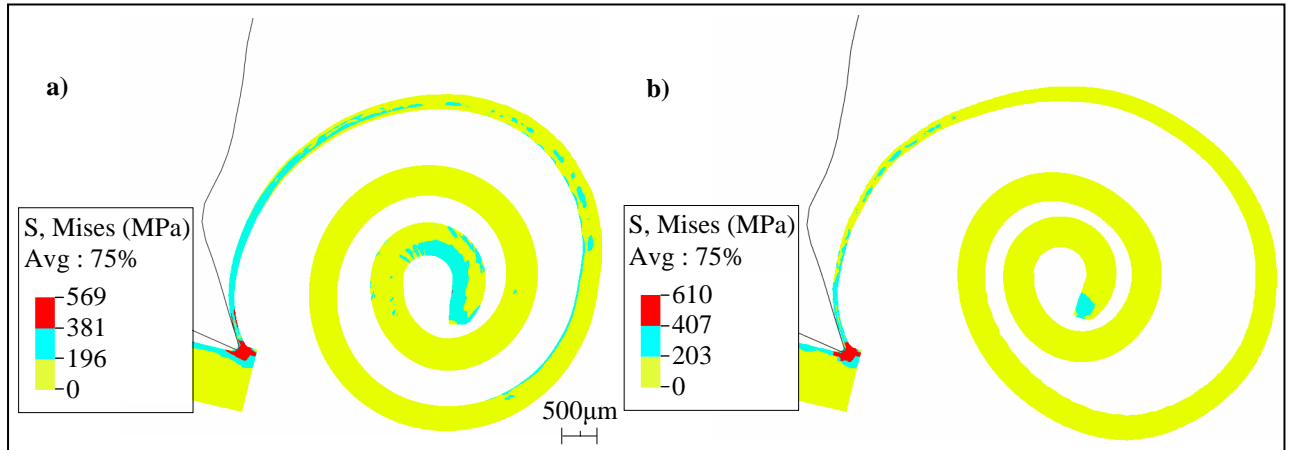


Fig. 3.21 von Mises stress plot at uncut chip thickness value of $22 \mu\text{m}$ at $V_C = 200 \text{ m/min}$
a)w/o SG b) with SG

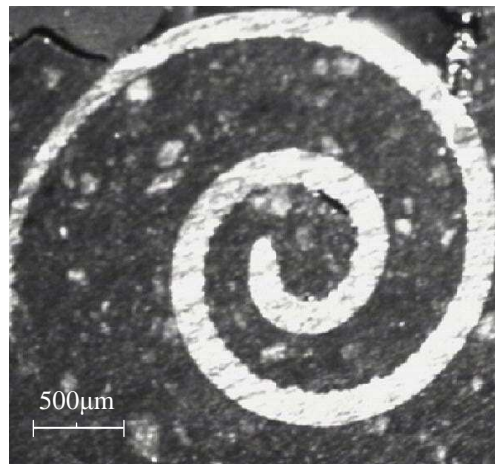


Fig. 3.22 Experimental chip, $V_C = 200 \text{ m/min}$

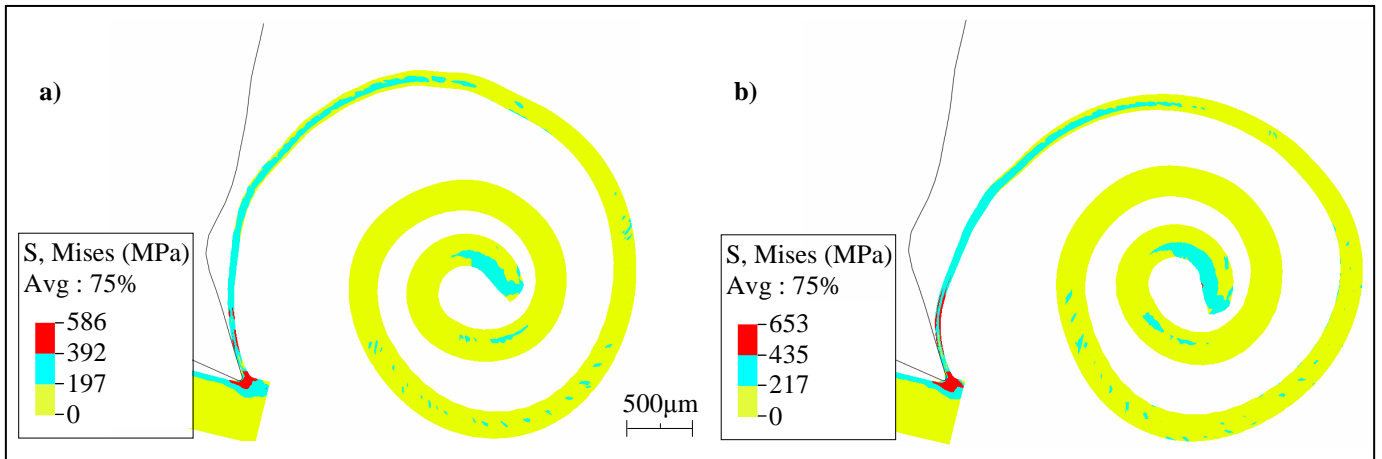


Fig. 3.23 von Mises stress plot at uncut chip thickness value of $22 \mu\text{m}$ at $V_C = 800 \text{ m/min}$
a)w/o SG b) with SG

3.5 Conclusions

The study proposes a phenomenological comprehension of material strengthening factors that contribute to size effect analysis in micro-cutting operations. Orthogonal down-cut milling case for a strain rate sensitive Aluminium alloy material A2024-T351 has been investigated. The important conclusions of this study could be underlined that:

- The implementation of a modified Johnson-cook material model via a user subroutine VUMAT in the commercial software ABAQUS[®]/EXPLICIT has allowed to analyze the contribution of the strain gradient-based hardening on size effect phenomenon at micro cutting level.
- During down-cut milling, tool-chip contact length decreases with the reduction of uncut chip thickness until it reaches a certain value. After that, it increases as uncut chip thickness decreases to micro dimensions. The latter state implies that the well-known minimum cutting chip thickness is reached and a higher energy is dissipated during frictional interaction at tool-chip interface, resulting in higher SCE.
- Similar trend concerning tool-chip contact length variation regarding uncut chip thickness was observed for all studied cutting speeds. Nevertheless, in the micro-level the length scale at which the rake-face/chip contact lengths start to increase proportionally to cutting speed. The higher the cutting speeds, the higher the length scales.

- The increments in the maximum von Mises stress magnitudes using strain gradient-based plasticity model, for various cutting speeds, are more or less the same. This suggests that strain gradient hardening is the dominant phenomenon for material strengthening at high cutting speeds and lower uncut chip thickness for the studied material.
- Specific cutting energy values obtained by numerical simulations using strain gradient –based plasticity model were quite close to the experimental ones. This shows that, to fully capture the size effect during micro cutting operations, strain gradient-strengthening mechanism can not be ignored even at high cutting speeds and for strain rate dependent materials.

Finally, this model permits to a close multi-scale physical understanding of the role of various strengthening factors contributing to size effect. It is with no doubt that strain gradient plasticity can bring more precisely comprehension to strengthening phenomena during cutting operation. Potentially, this will allow improving the existing cutting models and help to capture events happening at micro-levels.

4 Hybrid Dynamic Cutting (HDC) Model for Milling

4.1 Introduction

Precious scientific investigations have been made to improve the machining processes by increasing productivity and controlling surface quality. Nevertheless, many limitations have been noted during the production efficiency improvement. For example, inextricable cutting process vibrations and their detrimental effects on surface integrity accelerate tool wear and possibly breakage of cutting insert and machine tool [ORH07]. Numerous methods have been proposed to analyze and control these devastating process vibrations [RAS08, TAT08, JIA08]. These methods include both the control of process parameters and structural modifications to improve the dynamic effects of the elastic structure of the machining system.

In this context, the present work put forwards, an original numerical approach to analyze milling tool vibrations effects on chip morphology and cut surface profile. For that, a hybrid numerical dynamic cutting model (HDC-model) is proposed. It represents an association between a discrete approach; at macroscopic level, characterising the high speed milling spindle system (tool, tool holder and rotor) and a continuous approach; at mesoscopic level, characterising the machined workpiece.

The case of an orthogonal down-cut milling process for Aluminium alloy A2024-T351 is studied. In the present work, the macroscopic level which considers milling spindle system stiffness is assumed to be characterised by two or three-degrees of freedom and have been coupled with the mesoscopic-level. For various realistic values of stiffness and damping, HDC-model results have been compared with those corresponding to a perfectly rigid spindle system. The modelling of milling considering latter case is recognized as a steady state cutting model, named SC-model in this particular research work. It is judicious to take the attention

of the reader that the FEM based numerical model discussed in detail in chapter 2 can be considered as a SC-model.

4.2 Hybrid dynamic cutting model (HDC-Model)

The explicit approach of finite element code ABAQUS[®] had been exploited to build a HDC-model treating the down-cut peripheral milling case. HDC-model combines afore-mentioned discrete approach; applied at macroscopic level and continuous approach; assumed at mesoscopic level detailed as:

- The macroscopic level: represents the elasticity of machine tool system; in terms of stiffness, damping and moment of inertia for a real high speed milling spindle system (tool, tool-holder and rotor).
- The mesoscopic level: represents chip formation process including the tool-workpiece interaction.

A schematic illustration of the HDC-model conceived in ABAQUS[®] is shown in Fig. 4.1.

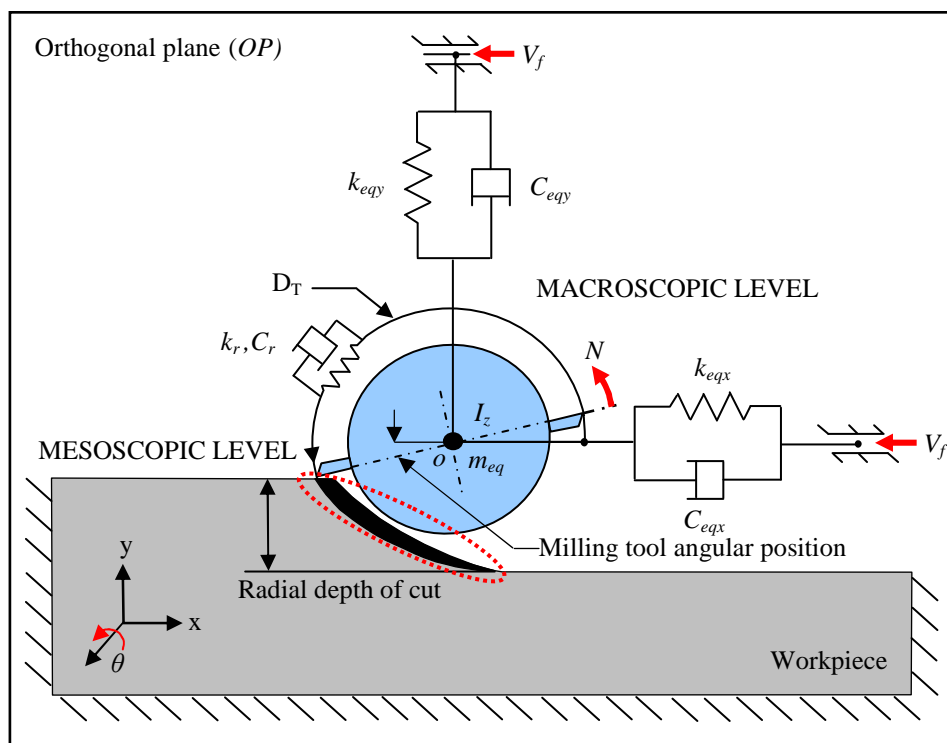


Fig. 4.1 A schematic 2D-representation of the down-cut milling

The geometry of an industrial high speed milling spindle system (Fig. 4.2) with power and rotation frequency of the order of 20 kW and 20,000 rpm was considered [GAG07], respectively.

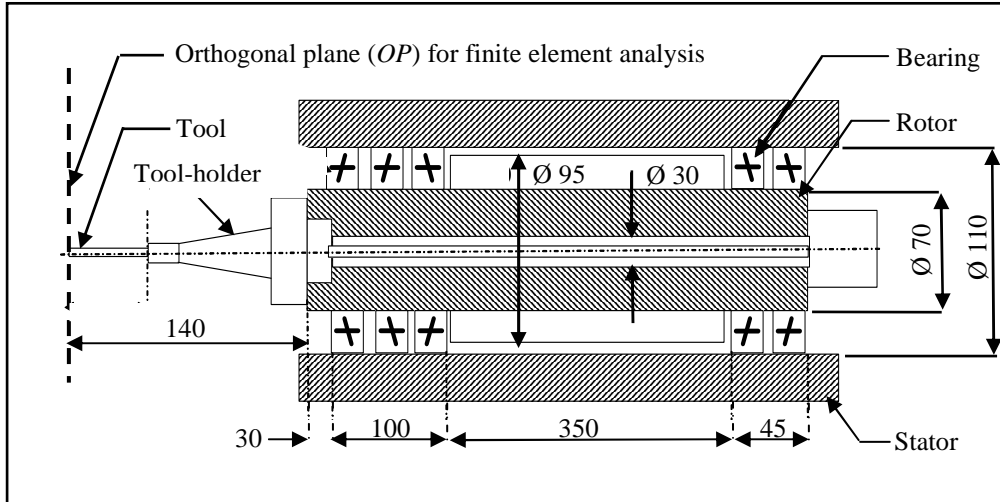


Fig. 4.2 2D-representation of an industrial milling spindle system (mm)

The discrete approach evokes a representation of the spindle system by an equivalent mass, m_{eq} , stiffness k_{eq} and damping C_{eq} . To compute the moment of inertia I_z , assembly of tool, tool-holder and rotor were taken into account.

Milling-tool vibrations; which are essentially depending on the spindle-bearing's wear, tool-workpiece materials, cutting parameters and machine-tool structure, were considered at orthogonal plane OP (Figure 4.2). Since, depending on the type of bearings (roller, ball, hydrodynamic, hydrostatic...) and afore-mentioned factors, the stiffness k_{eq} and damping ratio ζ_{eq} values of the machining system are extremely variable. For example, to study experimentally the stiffness and damping effects on tool-life for CBN (cubic boron nitride) and PCD (polycrystalline diamond) inserts for turning and milling cases Chryssolouris [CHR82] had considered a wide range of tool /tool holder stiffness values (0.35E7 to 0.65E8 N/m), respectively. While, Lalanne and Ferraris [LAL97] have considered stiffness values as high as 4E8 N/m, in their rotor dynamics investigations. A similar variation in damping values has also been noted in the Rivin et al. experimental research work [RIV90, RIV92] on the design of cantilever boring bars. They had used antivibration devices (dampers) with an extremely variable damping ratio (0.07-0.4). Therefore, a wide range of these values was chosen for the proposed parametric study (Table 4.1).

| | |
|------------------------------------|-------------|
| $m_{eq} = m_{eqx} = m_{eqy}$ (Kg) | 0.5 |
| I_z (Kg-m ²) | 0.0065 |
| $k_{eq} = k_{eqx} = k_{eqy}$ (N/m) | 2E7 and 2E8 |
| k_{eqr} (Nm/rad) | 2E8 |
| ζ_{eq} | 0.0 and 0.1 |

Table 4.1 Parameters for macroscopic model

4.2.1 Machining system definition at macroscopic level

Two types of vibration cases treating the down-cut milling were considered. Equations of movement corresponding to each case adopted are given by follows:

Case-1: Discrete system with two degree of freedom: In this case equivalent mass center o (Fig. 4.1) was allowed to vibrate in (x, y) plane. Considering, a constant value of V_f , the set of motion equations for this system is expressed as:

$$\left. \begin{aligned} m_{eqx} \ddot{x} + c_{eqx} \dot{x} + k_{eqx} x &= \sum F_x \\ m_{eqy} \ddot{y} + c_{eqy} \dot{y} + k_{eqy} y &= \sum F_y \end{aligned} \right\} \quad (4.1)$$

Where x, y represent tool and tool-holder vibration positions and m_{eqx} and m_{eqy} their equivalent masses in x and y directions, respectively. (c_{eqx}, k_{eqx}) and (c_{eqy}, k_{eqy}) are equivalent damping and stiffness in x and y directions, respectively.

A linear behaviour of the spring elements in ABAQUS[®] was used. The relative displacement Δu of a spring element; defined between two nodes, is the change in the spring between initial length, l_0 , and spring current length, l . It can be calculated by the following equation:

$$\Delta u = l - l_0 \quad (4.2)$$

Where $l = |x_1 - x_2|$ and x_1 and x_2 are current node positions.

Case-2: Discrete system with three degree of freedom: In this case a rotation degree of freedom along tool-axis of rotation (Z -axis) was included considering constant values of tool feed velocity V_f and spindle rotation frequency, N . The set of motion equations for this system is expressed as (Eq. 4.3).

$$\left. \begin{aligned} m_{eqx} \ddot{x} + c_{eqx} \dot{x} + k_{eqx} x &= \sum F_x \\ m_{eqy} \ddot{y} + c_{eqy} \dot{y} + k_{eqy} y &= \sum F_y \\ I_z \ddot{\theta} + c_{eqr} \dot{\theta} + k_{eqr} \theta &= \sum M \end{aligned} \right\} \quad (4.3)$$

Where I_z is the moment of inertia of the tool, tool-holder and rotor assembly; along tool axis of rotation (Z-axis), k_{eqr} rotational stiffness, θ rotational vibration and c_{eqr} is rotational damping. Springs and dashpots like elastic connector elements were used. It is important to underline that these elements do not control/influence the stable time of increment calculation, in ABAQUS[®] explicit approach [ABQ07].

4.2.2 Workpiece definition at mesoscopic level

The workpiece geometry and its mesh were conceived in ABAQUS[®] for 2D orthogonal down-cut peripheral milling case, considered at mesoscopic level as shown in Fig. 4.3.

As discussed in previous chapters that it was hypothesized that the value of feed rate f is very less than the axial cutting depth, a_p . Therefore, plane strain calculations were performed. Tool was assumed to be a rigid body and boundary conditions were applied at its centre of rotation. It can advance with feed velocity, V_f , in negative x -axis direction and can rotate with N in anti-clockwise direction (Fig. 4.3).

For the present work, a milling tool with two cutters and diameter, D_T of 25 mm was used. As the tool rotates and advances simultaneously, the cutters trace trochoidal paths in ideal case i.e. if vibration characteristics of tool are ignored [MON91]. This produces variable section chip. Trochoidal path set provided in chapter 2 was used to model milling-cutter path zone (chip separation zone) and chip section geometry.

The material model, mesh size, chip separation criteria, size of tool path zone, tool workpiece interaction and material properties are the same as discussed in detail in chapter 2.

During the trochoidal motion of milling tool uncut chip thickness, h , decreases (Fig. 4.3) and approaches to tool hone edge radius R_n dimensions, where it generates wider plastic shear zone, when compared with the one produced by a sharp edge tool [LIU07]. Therefore, material removal requires higher energy dissipation and consequently the cutting force increases. In the present numerical model an edge radius tool ($R_n = 20 \mu\text{m}$) is considered. So that its effects on chip morphology, machined surface topology and cutting force during dynamic cutting could be included.

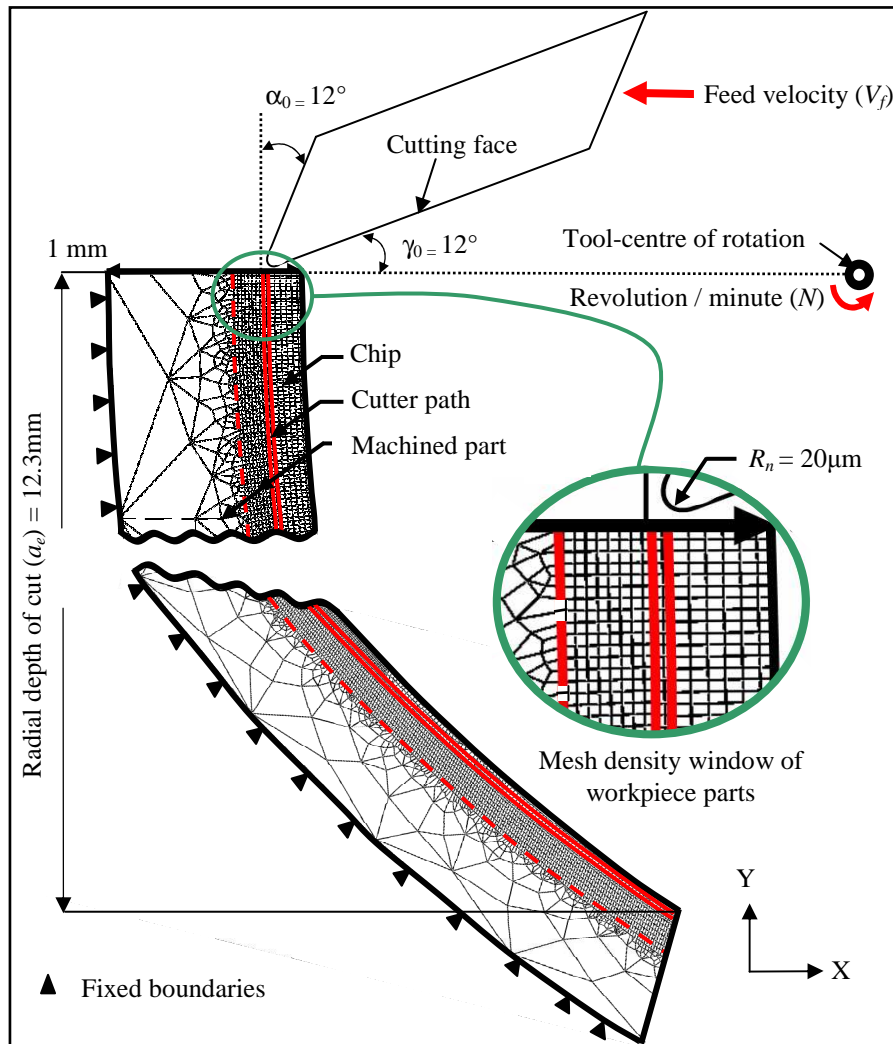


Fig. 4.3 Tool-workpiece geometrical model and boundary conditions

4.3 Results and discussion

The present section deals with the milling tool vibration effects on chip morphology, machined surface profile and cutting force. The orthogonal down-cut milling case of an aeronautic Aluminium alloy A2024-T351 for two cutting speeds; 300 and 800 m/min with a fixed feed rate of 0.4 mm/rev had been treated. Initially, numerical simulations for SC-model were carried out according to each cutting speed. Afterwards, computation was performed for HDC-model with various parametric values (Table 4.1). Results corresponding to nodal temperature at tool-workpiece interface and the surface profile obtained by HDC-model were compared with those obtained by running SC-model simulations, while those corresponding to cutting force and chip morphology are compared to the experimental ones. Moreover, tool-tip-centre (TTC) oscillations were computed and compared with the trochoidal path traced in

SC-model simulation. The dynamic effects on friction and shear angles are also discussed in this section.

4.3.1 Stiffness and damping effects on chip morphology and machined surface topology

To avoid the repetition, some results for $V_C = 300$ m/min are given. However, those considering $V_C = 800$ m/min have been discussed in detail. For SC-model considering $V_C = 800$ m/min, nodal temperature evolution NT on chip and workpiece parts is shown in Fig. 4.4a. Chip morphology evolves from slightly segmented to continuous shape, as UCT decreases. Globally, nodal temperature is lower on chip free surface side and maximum on chip back surface due to the frictional heating at tool-chip interaction interface. Fig. 4.4b presents the experimentally obtained chip in the same pre-cited working parameters. Figure 4.5 presents nodal temperature evolution on workpiece and chip morphology obtained in case of HDC-model for $V_C = 800$ m/min; considering various parametric values as defined in Table 4.1. The Fig. 4.5a and 4.5b concern a case without damping at the level of the discrete system (2 dof) with two stiffness values of $2E7$ N/m, $2E8$ N/m, respectively.

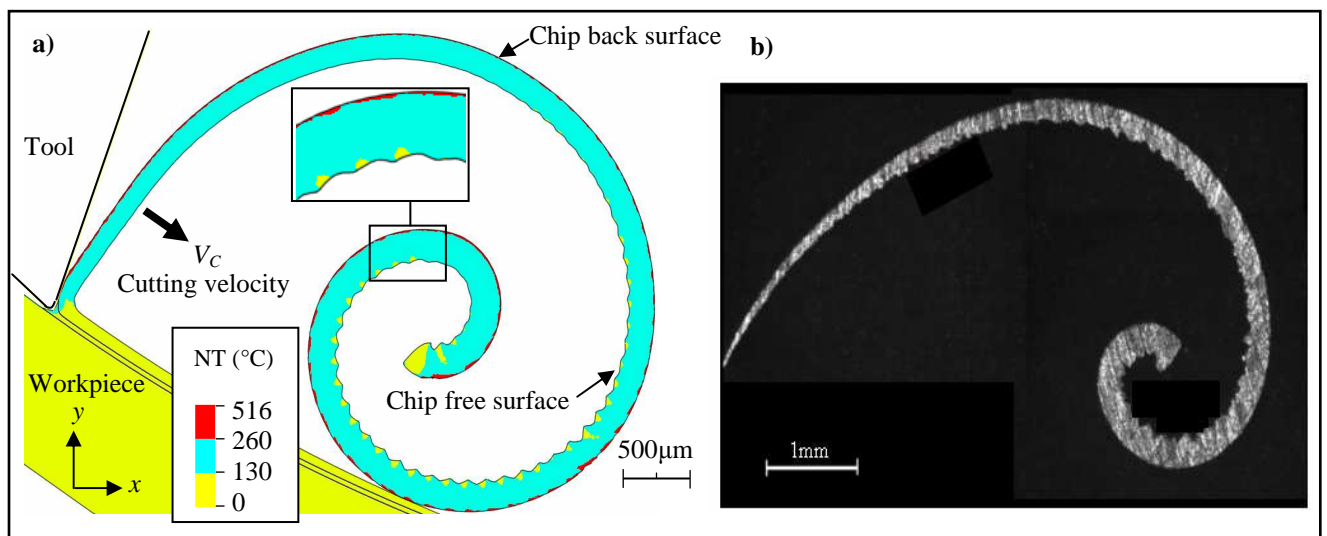


Fig. 4.4 Chip morphology at $V_C = 800$ m/min a) Nodal temperature (NT) distribution on workpiece in the case of (SC-model) b) Experimentally obtained chip

It can be seen that, the system with lower stiffness (Fig. 4.5a) has generated a highly segmented chip with fifteen sharp teeth (from TTC angular position 0° to 22°) with an average segmentation wavelength of $203 \mu\text{m}$. However, number of chip segments and segmentation average wavelength had been reduced to seven and $199 \mu\text{m}$ (Detail A),

respectively; by increasing the system stiffness (Fig. 4.5b). This shows that, the lower the system stiffness, the higher pronounced the chip segmentation. Numerical simulation for lower stiffness $2E7$ N/m (Fig. 4.5a) was stopped earlier (at TTC 22° angular position) due to higher distortion in some of chip mesh element. While the simulation was continued for the system with higher stiffness ($2E8$ N/m) as shown in Fig.4.6 where chip morphology evolves from sharply segmented to continuous shape, as UCT decreases.

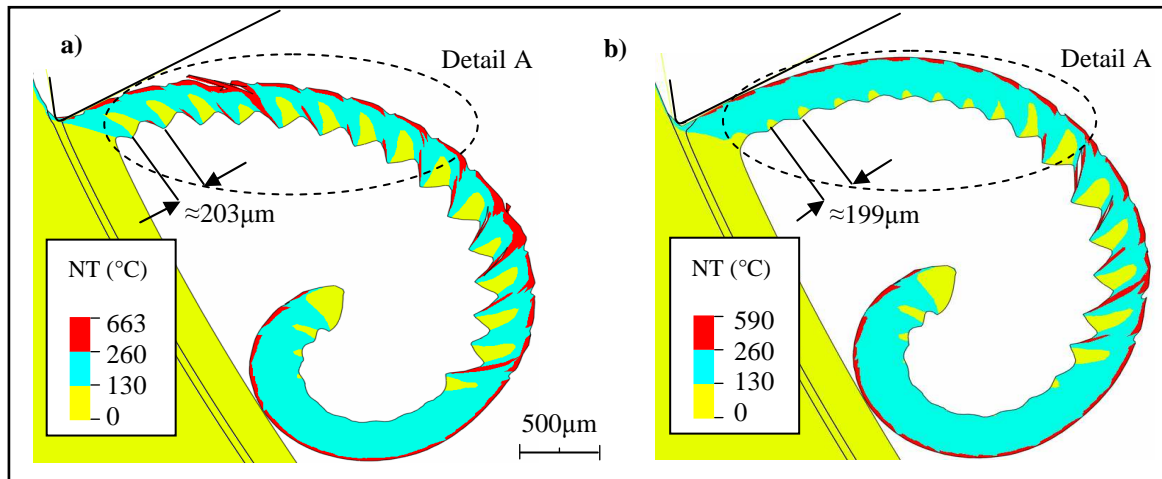


Fig. 4.5 Nodal temperature (NT) distribution and chip morphologies at $V_C = 800$ m/min (case of HDC-model, 2 dof and $\zeta_{eq} = 0$) a) $k_{eq} = 2E7$ N/m b) $k_{eq} = 2E8$ N/m

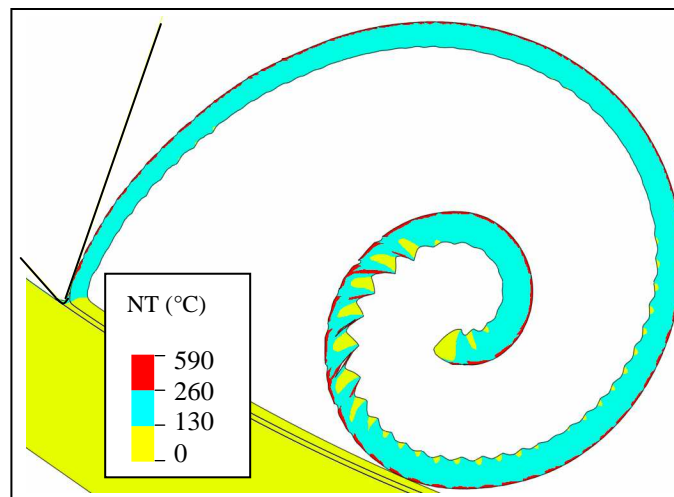


Fig. 4.6 Nodal temperature (NT) distribution and chip morphologies at $V_C = 800$ m/min (case of HDC-model, 2 dof, $\zeta_{eq} = 0$ and $k_{eq} = 2E8$ N/m)

Fig. 4.6, corresponds to the similar case of higher stiffness value ($k_{eq} = 2E8$ N/m) as shown in Fig. 4.5b, but for 57° of TTC angular position. By comparing Fig. 4.5 and Fig. 4.6 it can be

noticed that maximum nodal temperature on tool-chip interface have been increased to 663°C and 590°C for lower and higher values of system stiffness (2E7 N/m and 2E8 N/m), respectively. This increase in temperature is due to the higher TTC amplitude vibration in the milling elastic system (shown later in Fig. 4.8).

Fig. 4.7 shows the nodal temperature distribution on workpiece and chip morphology (HDC-model, 3 dof) for cutting speed of $V_C = 800$ m/min and a constant value of discrete system stiffness ($k_{eq} = 2E8$ N/m, $k_{eqr} = 2E8$ Nm/rad). It can be noticed that, by including rotational rigidity in the numerical model, nodal temperature at tool chip interface are reduced and comparatively continuous chip morphologies are obtained. In these conditions, it is remarked that the variation of equivalent damping ratio ζ_{eq} between 0 and 0.1 (Fig. 4.7a and Fig. 4.7b, respectively) causes the less pronounced segments on chip (detail B). This is due to the reduction in the amplitude of TTC oscillations (shown later in Fig. 4.8). Consequently, maximum nodal temperature at tool-chip interface had been slightly decreased. In these conditions, the simulated chip morphologies are comparable with that obtained experimentally.

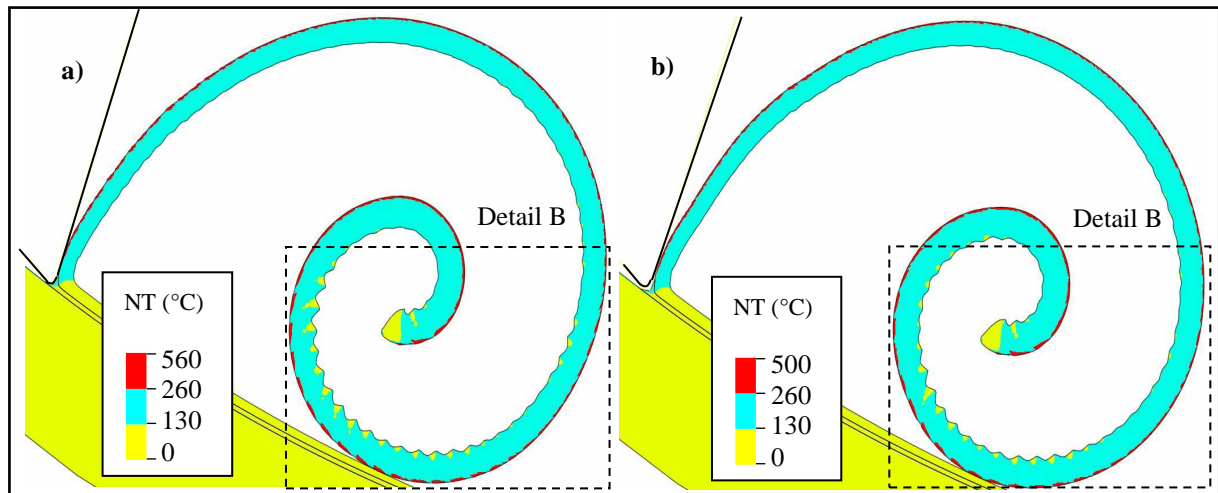


Fig. 4.7 Nodal temperature (NT) distribution and chip morphology at $V_C = 800$ m/min (case of HDC-model with 3 dof and $k_{eq} = 2E8$, $k_{eqr} = 2E8$ Nm/rad a) $\zeta_{eq} = 0$ b) $\zeta_{eq} = 0.1$

Fig. 4.8 presents, five TTC paths (rotation from 0 to 90° angular position) traced for SC and HDC-models in x-y frame of reference considering various parametric values (Table 4.2) at $V_C = 800$ m/min. It can be observed that for HDC-model cutter oscillates around the trochoidal path 1 traced during SC-model simulations. This figure shows globally, that the

cutter-tip entrance in the material is characterised by an important TTC's oscillation amplitude when compared with the end of cutting operation (in the vicinity of 90°).

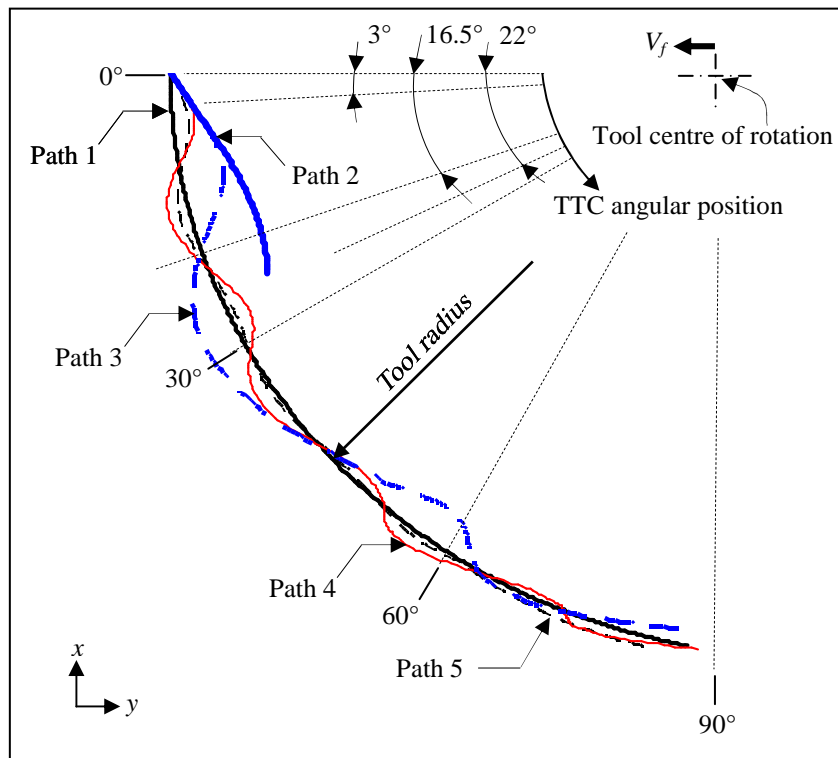


Fig. 4.8 Radial amplified five TTC paths traced for SC and HDC-models considering various parametric values (Table 4.2) at $V_C = 800$ m/min

| Models | Path/Plot/Profile number | k_{eq} | k_{eqr} | ξ_{eq} |
|-----------|--------------------------|----------|-----------|------------|
| SC-model | 1 | ∞ | ∞ | ∞ |
| HDC-model | 2 | 2E7 | ∞ | 0 |
| | 3 | 2E8 | ∞ | 0 |
| | 4 | 2E8 | 2E8 | 0 |
| | 5 | 2E8 | 2E8 | 0.1 |

Table 4.2 TTC paths, cutting force plots and machined surface profiles for various machining system parameters

Fig. 4.9 presents, the surface topology (in terms of radial displacements of machined surface nodes) regarding TTC angular position (from 0° to 30°). All the five cases of SC and HDC-

models considering various parametric values (Table 4.2) have been treated. Nevertheless, from 30° to 90° no considerable differences were found in all cases.

For angular position up to 3° all the TTC paths traced for HDC-model, had the same amplitude of oscillation (Fig. 4.8), generating similar surface topologies as shown in zone 1 Fig 4.9. Afterwards (less than 22° of TTC angular position), TTC had been oscillated to maximum amplitudes (peak-to-peak) of $12\ \mu\text{m}$ for path 2, and $4.7\ \mu\text{m}$ for path 3 (Fig. 4.8), producing highly wavy surfaces for profile 2 and profile 3 with average amplitude of vibration $10.5\ \mu\text{m}$ and $6\ \mu\text{m}$, respectively (zone 2, Fig. 4.9). It is interesting to note that, in the later zone nodal radial displacements are higher corresponding to maximum amplitudes of TTC oscillations in this angular position (Fig. 4.8).

Afterwards, as UCT decreases, TTC vibration amplitude is reduced to $2.6\ \mu\text{m}$ (in the vicinity of 90°) for path 3. It is to note that, vibration data amplitude is non available for lower uncut chip thickness; for path 2, as calculation had been stopped earlier due to higher distortion of the chip mesh element (as said previously). Whereas, for un-damped and damped 3dof HDC-model (for less than 22° of TTC angular position), TTC oscillations defined by path 4 and path 5, had been reduced to maximum amplitudes of $1.3\ \mu\text{m}$ and $0.97\ \mu\text{m}$, respectively. This had caused fewer effects on surface topologies (profiles 4 and 5 in Fig. 4.9). Likewise, as UCT decreases, TTC oscillation amplitude is reduced to $0.56\ \mu\text{m}$ and $0.35\ \mu\text{m}$, respectively (in the vicinity of 90°) comparable with SC-model one (profile 1). Zone 3 corresponds to TTC angular position from 30° till end where chip morphologies had been evolved to more or less continuous shape for both SC and HDC-models.

Moreover, Fig. 4.9 helps to summarize that the segmented chip morphology which is the result of TTC oscillations had been reflected on the machined surface in the form of wavy surface profiles; with average wavelengths of $200\ \mu\text{m}$ and $198\ \mu\text{m}$ on profile 2 and profile 3, respectively. These wavelengths are comparable to the pre-cited average segmentation ones shown in Fig. 4.5 ($203\ \mu\text{m}$ and $199\ \mu\text{m}$, respectively). This segmentation is due to thermal softening phenomenon. The latter is the result of the inelastic deformations which are directly affected by the TTC oscillation amplitudes.

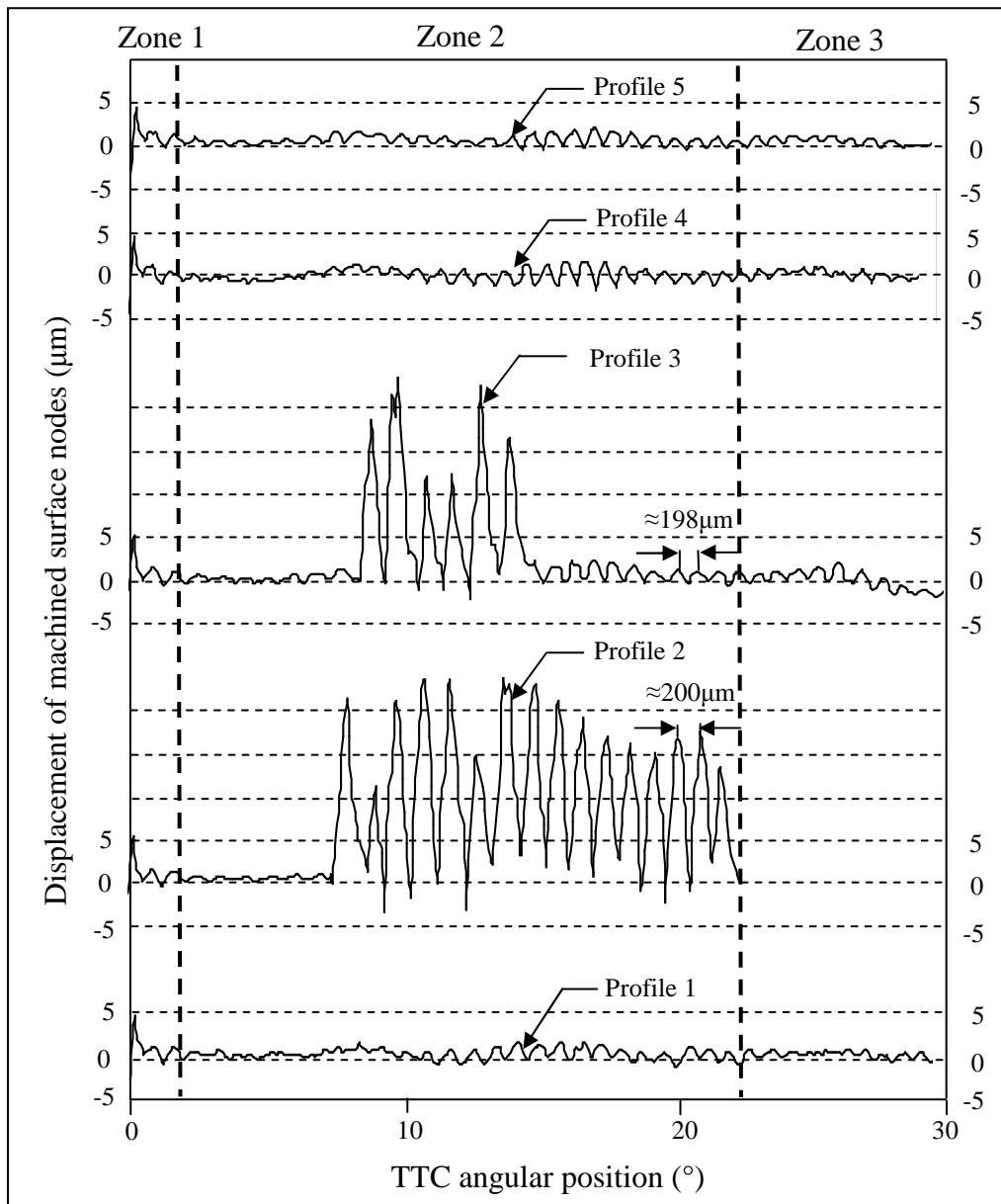


Fig. 4.9 Radial displacements of machined surface nodes for SC and HDC-models at $V_C = 800$ m/min, (Profile i defined in Table 4.2)

4.3.2 Cutting speed effects on cutting force, chip morphology and machined surface topology

Afterwards, numerical simulations for HDC-model considering $V_C = 300$ m/min were performed. The discrete system parameters were similar to those presented in Table 4.1. In these conditions, the temperature at tool-workpiece interface had been decreased due to the decrease in the frictional work caused by the cutting speed drop (Fig. 4.10).

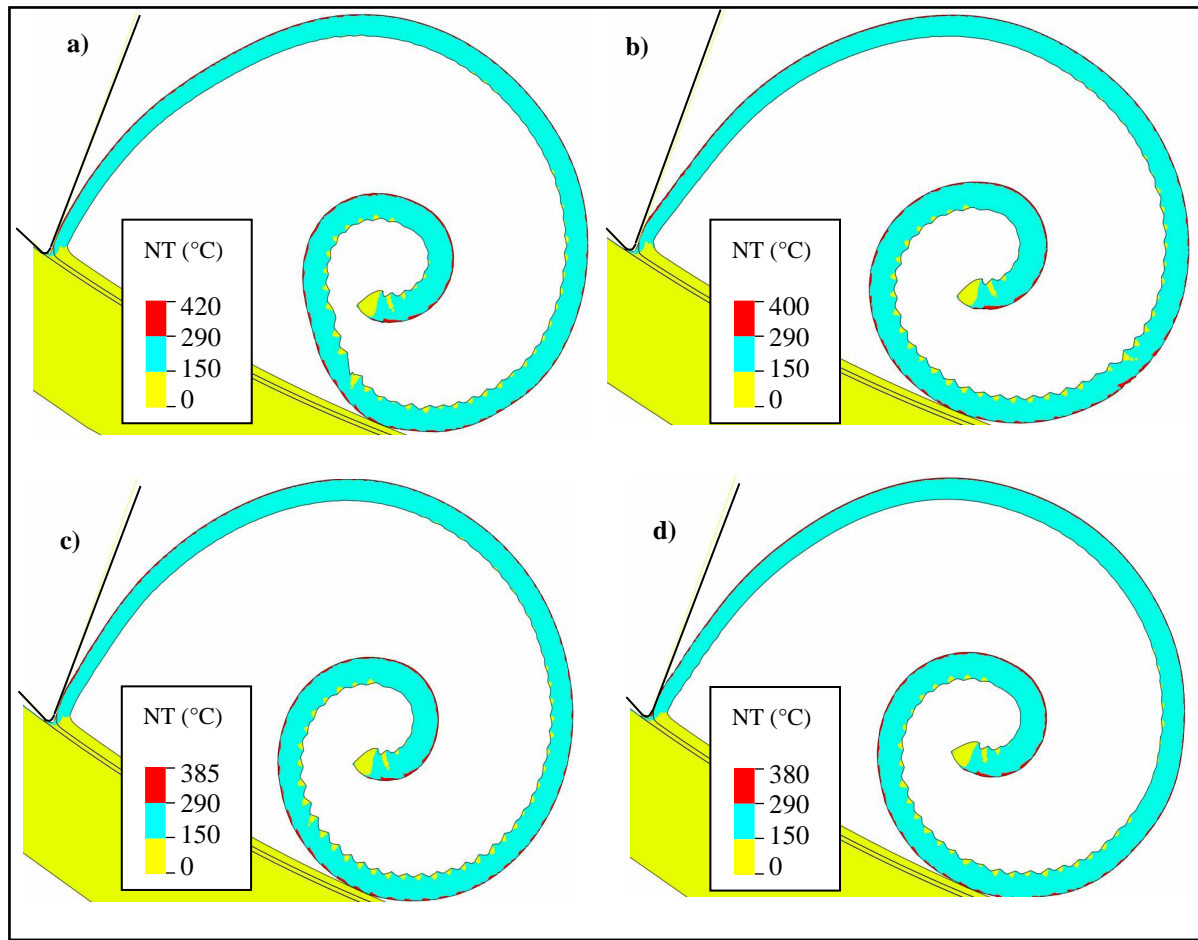


Fig. 4.10 Nodal temperature (NT) distribution and chip morphology at $V_C = 300$ m/min a) 2 dof ($k_{eq} = 2E7$ N/m, $\zeta_{eq} = 0$) b) 2 dof ($k_{eq} = 2E8$ N/m, $\zeta_{eq} = 0$) c) 3 dof ($k_{eq} = 2E8$, $k_{eqr} = 2E8$ Nm/rad, $\zeta_{eq} = 0$) d) 3 dof ($k_{eq} = 2E8$, $k_{eqr} = 2E8$ Nm/rad, $\zeta_{eq} = 0.1$)

It was also found that for all the four previously discussed cases in relationship with HDC-model (Fig. 4.5 and Fig. 4.7 for $V_C = 800$ m/min); TTC oscillations had been reduced by decreasing cutting speed. Accordingly, less wavy surface topologies were produced as shown in Fig. 4.11. The latter presents radial displacements of machined surface nodes as a function of TTC angular position (from 0° to 30°) for $V_C = 300$ m/min for both SC-model (profile 1) and HDC-mode 1 (profiles 2 to 5 for 2 dof and 3 dof cases).

Table 4.3, provides a comprehensive comparison between the effects of the two cutting speed conditions 300 and 800 m/min on the maximum amplitude (peak-to-peak) of TTC oscillations; calculated by using the HDC-model. It can be noted that for both cutting speeds considering discrete system of 3 dof at macroscopic level, with parameters: $k_{eq} = 2E8$ N/m, $k_{eqr} = 2E8$ Nm/rad and $\zeta_{eq} = 0.1$, the computed results of TTC oscillations and machined surface profile

are in close corroboration with SC-model ones and chip morphology hence obtained is comparable to the one obtained experimentally.

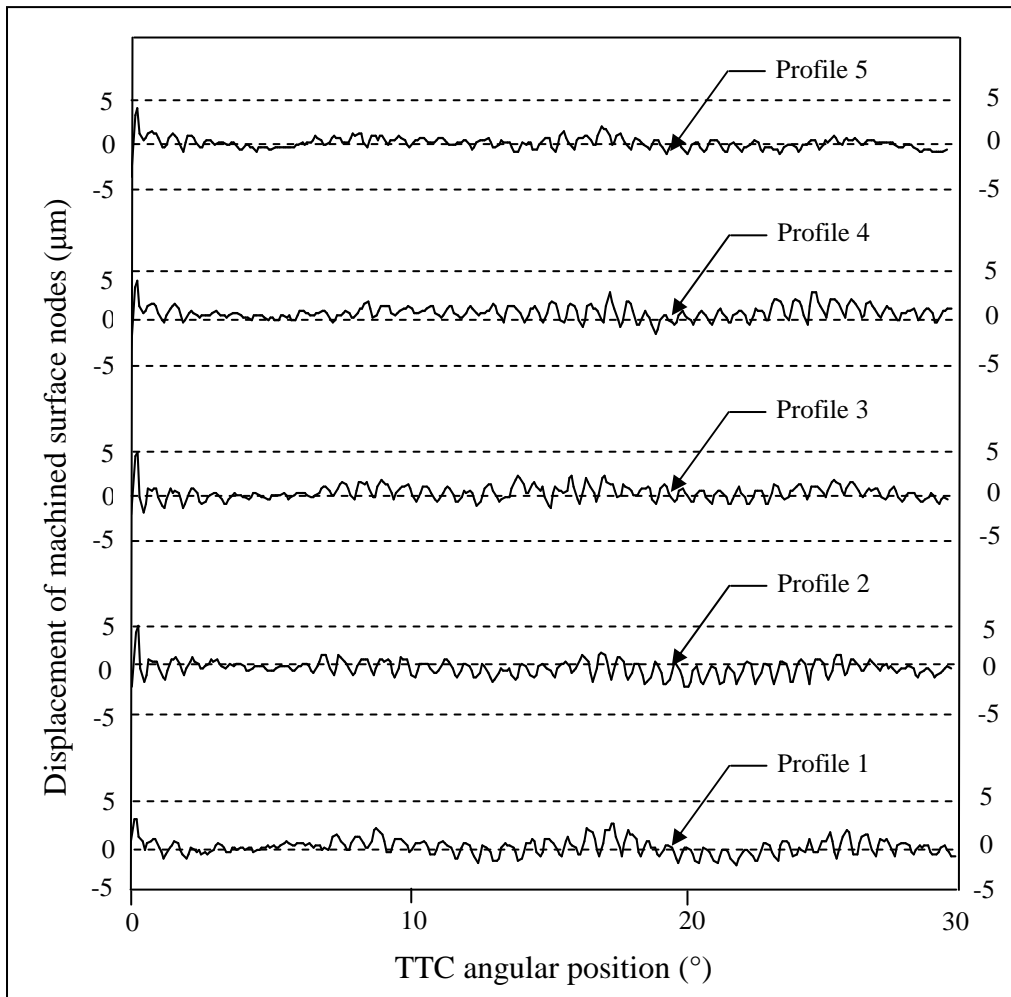


Fig. 4.11 Radial displacements of machined surface nodes for SC and HDC-models at $V_C = 300$ m/min, (Profile i defined in Table 4.2)

Fig. 4.12 presents the cutting force versus TTC angular positions at $V_C = 800$ m/min for SC and HDC-models considering various parametric values (Table 4.2). It can be seen that cutting force for all HDC models oscillates around SC-model (plot-1). It is interesting to note that cutting force oscillation periods resemble to those of TTC oscillation periods for all HDC-models (Fig. 4.8).

Additionally, the cutter-tip entrance in the material is characterised by high cutting force oscillation amplitude when compared with that corresponding to the end of cutting operation. For $V_C = 300$ m/min similar tendency of cutting force oscillations can be noted (Fig. 4.13). The average values of cutting force plots at various UCT values for HDC-model (3 dof $k_{eq} =$

2E8 N/m, $k_{eqr} = 2E8$ Nm/rad, $\zeta_{eq} = 0.1$) are globally comparable with those obtained experimentally for similar cutting parameters and material [FAN05, ZAG09].

| HDC-model | Maximum amplitude (peak-to-peak) of TTC oscillations (μm) | | | | Remarks |
|--|--|-----------------------------|-----------------------------|-----------------------------|--|
| | $V_C = 300$ m/min | | $V_C = 800$ m/min | | |
| | TTC at 20° angular position | TTC at 80° angular position | TTC at 20° angular position | TTC at 80° angular position | |
| Discrete system with 2 dof ($k_{eq} = 2E7$, $\zeta_{eq} = 0$) | 9.8 | 4 | 12 | NA | Undulated surface and sharply segmented chip morphology (for higher V_C and h) |
| Discrete system with 2 dof ($k_{eq} = 2E8$, $\zeta_{eq} = 0$) | 4.3 | 1.8 | 4.7 | 2.6 | Undulated surface and sharply segmented chip morphology (for higher V_C and h) |
| Discrete system with 3 dof ($k_{eq} = k_{eqr} = 2E8$, $\zeta_{eq} = 0$) | 1.1 | 0.35 | 1.3 | 0.56 | Surface and chip morphology fairly comparable with SC-model and experimental chip, respectively |
| Discrete system with 3 dof ($k_{eq} = k_{eqr} = 2E8$, $\zeta_{eq} = 0.1$) | 0.78 | 0.30 | 0.97 | 0.35 | Surface and chip morphology in good comparison with SC-model and experimental chip, respectively |

Table 4.3 Effects of cutting speed variation on TTC oscillations (μm), surface profile and chip morphology

The plots 2 to 4 in Figs. 4.12 and 4.13; where instantly the cutting forces become negative, help to state that, for less rigid machining systems (also with minimal structural damping) there will be a resistance of the workpiece material during very small instant(s) of time (order of μs) especially in the vicinity of the smaller thicknesses. Furthermore, elastic recovery of the material is also important under these conditions (higher V_C and lower h) [KIM04b, LIU04b]. Onward, the cutting phenomenon takes place and the cutting force becomes positive. The low chip thickness zone(s) is interesting to study, because in its vicinity the final machined surfaces are generated by the consequence of an adequate removal of the material (micrometric thicknesses of the chip). The obtained machined surface quality is however,

affected by the degree of machining vibration. In our case, it seems that plots 1 and 5 are most interesting cases of actual machining without much of disturbance.

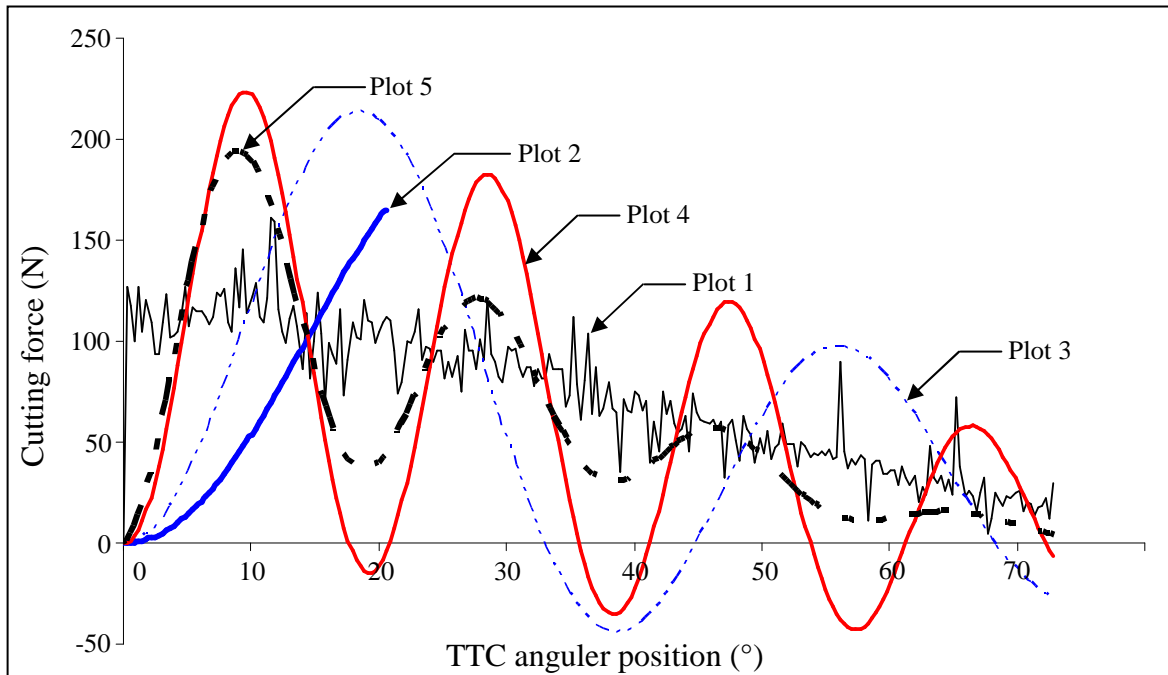


Fig. 4.12 Cutting force plots for SC and HDC-models considering various parametric values (Table 4.2) at $V_C = 800$ m/min, (Plot i defined in Table 4.2)

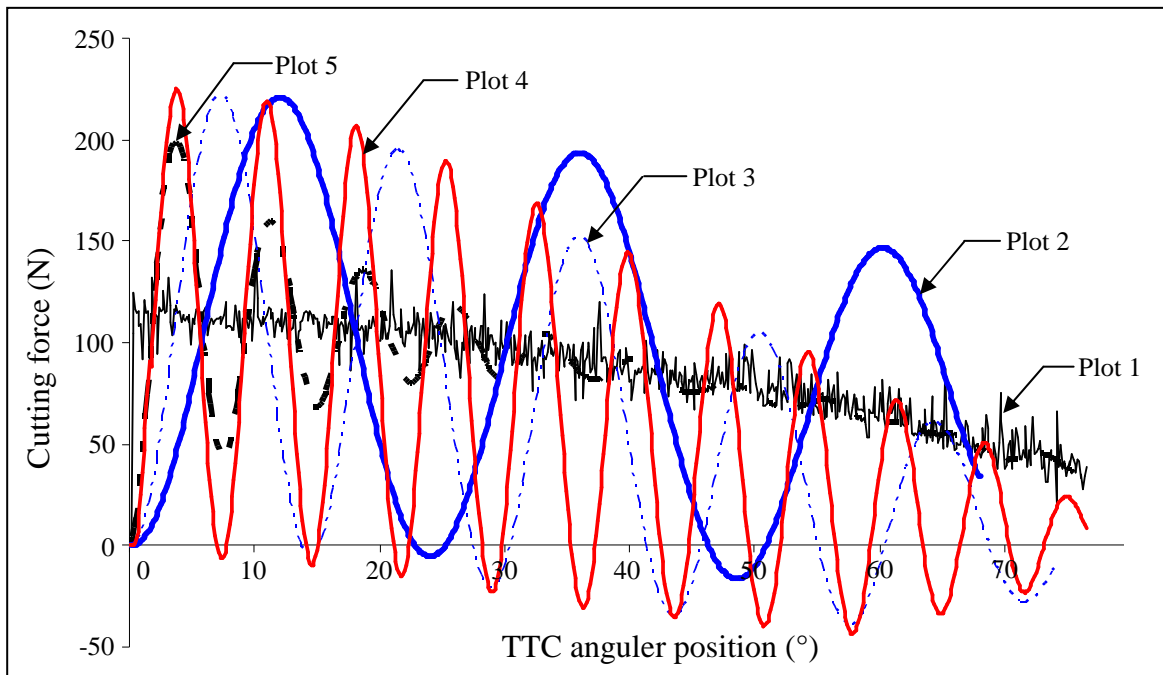


Fig. 4.13 Cutting force plots for SC and HDC-models considering various parametric values (Table 4.2) at $V_C = 300$ m/min, (Plot i defined in Table 4.2)

Nonetheless, it is important to underline that the simulations run with HDC-model are unable to capture high frequency cutting force oscillations (as shown in plot 1) which corresponds to chip segmentation frequency [MAB06], unless run with infinitely stiff and damped system.

4.3.3 Stiffness and damping effects on tool - chip interaction and chip shear angle

This subsection treats briefly the dynamic cutting effects on both tool-chip interaction and chip primary shear angles in the case of the two previous cutting speeds.

In terms of contact pressure and chip contact length at the tool-chip interface, it can be remarked, (at 16.5° of TTC angular position) that the lower the rigid and/or un-damped systems, the higher the contact pressures and chip contact lengths (Table 4.4). Specifically, for a case of less rigid un-damped system (Discrete system with 2 dof $k_{eq} = 2E7$, $\zeta_{eq} = 0$) and which can be qualified by a highly vibrating tool (Table 4.3), the high contact pressure at tool-chip interface leads to an increase in local temperature as it was shown in (Fig. 4.5). This enhances the segmented chip formation and the increase of the tool-chip contact length.

Moreover, this is important to underline that the tool flank face-workpiece contact which generates process damping has an important effect in dynamic cutting as it was shown by Kegg [KEG65]. The Latter has underlined that the process damping or friction between the wavy surface of the workpiece and flank face is crucial in determining the chatter stability at low speed cutting conditions. Other research work [ALT04] has pointed out nature of tool rake and workpiece contact to control this chatter stability when the cutting process is highly nonlinear due to time variation and process damping at low speeds, and also when the structural dynamics of the machining system vary along the tool path. The effect of this damping process is neglected at high cutting speeds which are considered in the present work. Concerning the chip deformation, fewer effects on the primary shear angle have been noted under various dynamic cutting conditions (HDC-models). Indeed, it has been seen that for $V_C = 300$ m/min (at TTC angular position of 16.5°) without considering damping ($\zeta_{eq} = 0$), the primary shear angles for 2 dof HDC-model are 38° and 37° when increasing k_{eq} from $2E7$ N/m to $2E8$ N/m, respectively. Otherwise, the shear angle remains unchanged (36°) for all other cutting models. A similar trend have been noted under the same conditions as previous, for higher cutting speed of 800 m/min, where the shear angles have been noted as 43° and 42° when increasing k_{eq} from $2E7$ N/m to $2E8$ N/m, respectively. Else not, shear angle remains equal to 39° for other cutting models.

At the end of this chapter it is important to underline that the essential findings are summarized via a schematic representation (Fig. 4.14) dealing with the effects of machining system characteristics (equivalent damping and stiffness), tool cutting speed and UCT on workpiece profile. So, it is shown that for higher cutting speeds and/or UCT values, TTC oscillations have remarkably influenced on the one hand, on the chip morphology and, on the other hand on the generated surface topology. This chip morphology had been replicated on machined surface; with the same wavelength of chip segments. Also, it is demonstrated that, the higher the machining stiffness and/or its damping; the lower the cutting force oscillation, chip segmentation process and fairly smooth machined surface profile.

| Models | $V_C = 800$ m/min | | $V_C = 300$ m/min | |
|---|------------------------|--|------------------------|--|
| | Contact pressure (MPa) | Tool-chip contact length (μm) | Contact pressure (MPa) | Tool-chip contact length (μm) |
| SC-model | 480 | 163 | 561 | 168 |
| HDC-model (Discrete system with 2 dof $k_{eq} = 2E7, \zeta_{eq} = 0$) | 1183 | 212 | 872 | 180 |
| HDC-model (Discrete system with 2 dof $k_{eq} = 2E8, \zeta_{eq} = 0$) | 547 | 178 | 719 | 172 |
| HDC-model (Discrete system with 3 dof $k_{eq} = k_{eqr} = 2E8, \zeta_{eq} = 0$) | 495 | 173 | 668 | 170 |
| HDC-model (Discrete system with 3 dof $k_{eq} = k_{eqr} = 2E8, \zeta_{eq} = 0.1$) | 475 | 170 | 572 | 168 |

Table 4.4 Dynamic cutting effects on friction at 16.5° of TTC angular position

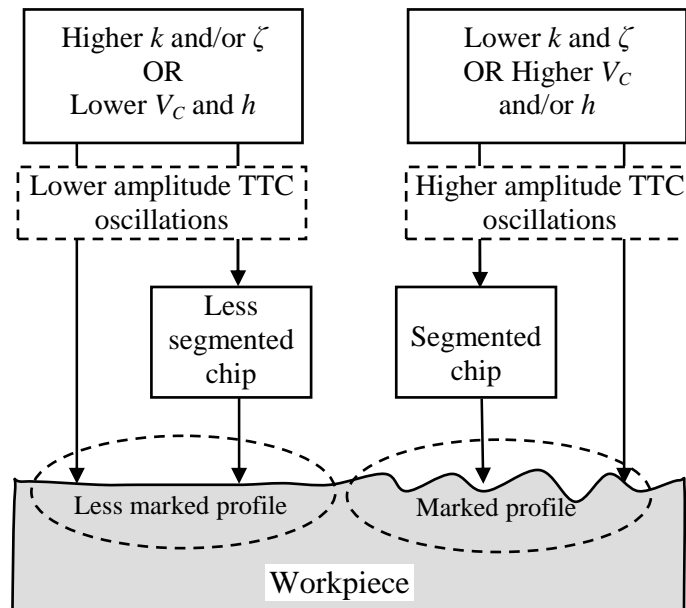


Fig. 4.14 A qualitatively representation of the milling TTC oscillation effects on chip morphology and machined surface

4.4 Conclusions

The global aim of the present study is to comprehend the milling-tool vibration effects on chip morphology, cutting force and surface topology by considering the machining system damping and stiffness with a variation of cutting speed. For that, a new orthogonal hybrid dynamic cutting model (HDC-model) has been proposed. This model puts forwards an original numerical approach which formalizes, on the one hand the machining system with discrete elements (dashpots, springs) and, on the another hand, the workpiece as a continuum material with thermo-visco-elasto-plastic behaviour.

The proposed HDC-model considers two and three degrees of freedom; representing the discrete milling vibration system. It had been found that for both higher cutting speed and UCT values, for a less rigid un-damped model (2 dof), milling-cutter oscillates with higher amplitudes inducing an increase in the temperature at tool-workpiece interface. Consequently, thermal softening phenomenon had been enhanced, affecting the chip morphology from a more or less continuous to a highly segmented chip with sharpened teeth. It was found that, chip morphology directly affects the surface topology. Indeed, segmented chip had produced higher radial displacements of surface nodes.

Though by increasing stiffness of HDC-model, chip segmentation had been reduced and the surface waviness was improved. However, a highly rigid damped model (3 dof) was found

more realistic with results of cutting force and chip morphology comparable to those obtained experimentally.

Finally, the proposed hybrid dynamic cutting model (HDC-model) [ASA10] for down-cut milling is suitable to account for real high speed milling system dynamics on chip formation process and surface topology. It permits also to make numerical parametric study to bring more physical understanding of the effect of machining system stiffness for large workpiece and cutting tool material ranges, numerous insert geometries and various cutting conditions ...etc.

In future, attention needs to be focused to exploit the HDC-model in order to study the effect of the regenerative vibration on the tool/workpiece interaction. Moreover, experimentation to validate the relationship between chip morphology and surface integrity from the points of view of metallurgical, geometrical and residual stresses need to be performed.

Synopses and Perspectives

A) Summary

The work presented in this dissertation focuses upon the selective aspects of the cutting process simulation with an ultimate aim of bringing multi-physical comprehension of chip formation process leading to a first-time-right design. Like any other research work produced in the field of science and technology, there always remains a margin for improvement; this dissertation is not an exception to the rule. Brief synopses of the efforts made, along with the perspectives for future work are described in following.

In this research work an orthogonal cutting model based on the coupling between damage evolution and material fracture energy for the case of turning and down-cut milling processes has been developed for an aeronautic strain rate dependent Aluminium alloy A2024-T351. On the one hand, the macroscopic/traditional level cutting focusing on chip genesis, chip segmentation, influence of fracture energy variation on chip morphology, chip fragmentation, machined surface topology were analyzed. On the other hand, the concepts of material strengthening at micro level cutting putting forward the role of strain rate, temperature and strain gradient (SG) hardening characteristics for the pre-cited material were investigated. To study the effect of SG hardening, material constitutive equations including SG effect were elaborated in ABAQUS[®]/EXPLICIT via its user subroutine VUMAT. In addition, to study milling-tool vibration effects on chip morphology, cutting force and surface topology under dynamic cutting conditions (with variable machining system stiffness and damping) a hybrid dynamic cutting model (HDC-model) has been established. The HDC-model combines the stiffness of a high speed milling spindle system (tool, tool-holder and rotor) at macroscopic level with the chip formation process at mesoscopic level. Finally, experiments have been carried-out to validate the proposed model(s).

B) Key findings of this work and future avenues

I) Numerical model with coupled material damage and fracture energy proposal

- The experimental results show that sharply segmented chip geometries are the result of higher cutting speeds for A2024-T351. This can provoke chip fragmentation in the chip zones where the segments are deeper.
- The chip visualizations (both numerical and experimental) demonstrate that fragmentation occurs just after the chip evacuation and not at the tool tip as it is commonly known in industrial community. The numerical results explain that this fragmentation, happening in the sharpest teeth zone, is the result of the bending loads caused by the effect of tool advance and chip–workpiece contact, simultaneously.
- The numerical simulations have helped to visualize clearly, the manner in which the damage is propagated during tool–workpiece interaction. Further, it has been underlined that the segmentation periodicity induces a waved machined surface and non uniform residual stress intensity on the machined surface. These directly dictate the structural and surface integrity of the machined workpiece.
- Sensitivity study of fracture energy (as an input value) on chip morphology shows that the stiffness of elements attributed with lower value of fracture energy could be degraded easily. This produces segmented chip morphology.
- Two dimensional elements with linear interpolation between the nodes were used for coupled temperature-displacement analysis. Improvement in results may be expected with quadratic interpolation between nodes, yet this would require a highly powerful computer and increased computation time.
- For the robustness of the numerical model, mechanical and thermal interactions between the contacting bodies need to be improved (user subroutine VUINTER can be used). Further a more realistic temperature and velocity dependent friction model can be implemented via user routine VFRIC.
- Experimental verification of the machined surface profile and residual stress pattern would be an interesting task.
- In future, model can be exploited to study the effect of the cutting tool radius, the tool layer grade and the boundary conditions on the machined workpiece.

II) Numerical model for macro-to-micro level cutting

For macro-to-micro level orthogonal down-cut milling model, the material strengthening factors that contribute to size effect in micro-cutting operations have been investigated and discussed. The important findings could be underlined as:

- During down-cut milling, tool-chip contact length decreases with the reduction of uncut chip thickness until it reaches a certain value. After that, this contact length increases as uncut chip thickness decreases to micro dimensions. This increase, in contact lengths, implies that a higher energy is dissipated during frictional interaction at tool-chip interface, resulting in higher specific cutting energy. This phenomenon is attributed to decrease in shear angle at lower chip thickness [ATK03] and higher strain rate sensitivity of A2024-T351.
- The decrease in the chip secondary shear zone temperature, while milling cutter approaches from macro to micro dimensions is not significant enough to cause any considerable contribution in increasing material strength and influencing size effect for the studied material.
- The implementation of a modified Johnson-cook material model via a user subroutine VUMAT in the commercial software ABAQUS[®]/EXPLICIT has allowed to analyze finely the contribution of the strain gradient based hardening on size effect phenomenon at micro cutting level for the studied material.
- The increments in the maximum von Mises stress magnitudes using strain gradient-based plasticity model, for various cutting speeds, are more or less the same. This suggests that strain gradient hardening is the dominant phenomenon for material strengthening at high cutting speeds and lower uncut chip thickness for the studied material.
- Specific cutting energy values obtained by numerical simulations using strain gradient –based plasticity model were quite close to the experimental ones. This shows that, to fully capture the size effect during micro cutting operations, strain gradient-strengthening mechanism can not be ignored even at high cutting speeds and for strain rate dependent materials.
- As frictional interaction has an increasing trend with the decrease in uncut chip thickness, this necessitates further investigation of frictional characteristic at micro level cutting.

- In future numerical model can be exploited to study the influence or the contribution of fracture energy on size effect phenomenon during micro level cutting as analytically proposed by Atkins [ATK03].

III) Hybrid dynamic cutting model (HDC-Model)

To study the milling-tool vibration effects on chip morphology, cutting force and surface topology by considering the machining system damping and stiffness, a new orthogonal hybrid dynamic cutting model (HDC-model) has been proposed. This model combines the machining system with discrete elements (dashpots, springs) and the workpiece as a continuous material with thermo-visco-elasto-plastic behaviour. HDC-model considers two and three degrees of freedom representing the discrete milling vibration system. The important findings could be highlighted as:

- For both higher cutting speed and uncut chip thickness values, for a less rigid undamped model (2 dof), milling-cutter oscillates with higher amplitudes inducing an increase in the temperature at tool-workpiece interface. Consequently, thermal softening phenomenon had been enhanced, affecting the chip morphology from a more or less continuous to a highly segmented chip with sharpened teeth.
- Chip morphology directly affects the surface topology. Indeed, segmented chip had produced higher radial displacements of surface nodes.
- A highly rigid damped model (3 dof) was found more realistic with results of cutting force and chip morphology comparable to those obtained experimentally.
- The proposed model permits to make numerical parametric study to bring understanding of the effect of machining system elasticity for large workpiece and cutting tool material ranges, numerous insert geometries and various cutting conditions ...etc.
- The simulations run with HDC-model are unable to capture high frequency cutting force oscillations which corresponds to chip segmentation frequency, unless run with infinitely stiff and damped system. This necessitates the coexistence of HDC-model along with the steady state (SC-model) cutting model.

- Linear behaviour of spring and dashpot elements was used for the present study. Improvement in results may be expected by considering temperature dependent, field variables dependent and visco-elastic behaviour of these elements.
- In future, attention needs to be focused to exploit the HDC-model in order to study the effect of the regenerative vibration on the tool-workpiece interaction.
- Experimentation to validate the relationship between chip morphology and surface integrity from the points of view of metallurgical, geometrical and residual stresses need to be performed.

The increase in the industrial requirements in terms of mechanical structure performance, coupled with the growing economic constraints enforces scientific and industrial communities to communicate together. The aim is to find and elaborate technological solutions. In our point of view this can be achieved by controlling the machining process. In this perspective, the FEM based numerical simulations have been emerged as a reliable tool with first-time-right design objective, especially after the advent of high speed computers and numerical algorithms. A well defined numerical cutting model not only brings the precise understanding of occurring phenomena and local useful information, but also suggests to improve tool design (geometry, surface coating), machined surface conditions (surface profile, surface integrity, roughness) and machine tool power requirements etc. It can even propose the structural modifications for an optimized reliable cutting.

Bibliography

- [ABQ07] **ABAQUS®/EXPLICIT** Theory and user manuals. Version 6.7.1 2007.
- [ACH00] **Acharya A, Bassani J L.** Lattice incompatibility and a gradient theory of crystal plasticity. *J. Mech. Phys. Solids*, 2000, 48(8), 1565-1595.
- [ALT04] **Altintas Y, Weck M.** Chatter stability of metal cutting and grinding. *Ann. CIRP Mfg. Technol.*, 2004, 53(2), 619-642.
- [ARG08] **Argon A S.** Strengthening Mechanisms in Crystal Plasticity. Oxford University Press Inc, New York , 2008.
- [ARS99] **Arsenlis A, Parks D M.** Crystallographic aspects of geometrically-necessary and statistically-stored dislocation density. *Acta Mater.*, 1999, 47, 1597–1611.
- [ASA08] **Asad M, Girardin F, Mabrouki T, Rigal J F.** Dry cutting study of an aluminium alloy (A2024-T351): a numerical and experimental approach. *Int. J. Mater. Form*, 2008, 1, 499-502.
- [ASA10] **Asad M, Mabrouki T, Rigal J F.** Finite-element-based hybrid dynamic cutting model for aluminium alloy milling. *Proc. IMechE Part B J. Engg. Mf.*, 2010, 224(1), 1-13.
- [ASH70] **Ashby M F.** The deformation of plastically non-homogeneous alloys. *Phil. Mag.*, 1970, 21, 399–424.
- [ATK03] **Atkins A G.** Modeling metal cutting using modern ductile fracture mechanics: quantitative explanations for some longstanding problems. *Int. J. of Mech. Sci.*, 2003, 45(2), 373-396.
- [BAC52] **Backer W R, Marshall E R, Shaw M C.** The size effect in metal cutting. *Trans. ASME*, 1952, 74, 61-72.
- [BÄK02] **Bäker M, Rösler J, Siemers, C.** A finite element model of high speed metal cutting with adiabatic shearing. *Comput. Struct.*, 2002, 80(5-6), 495–513.
- [BÄK03] **Bäker M, Rösler J, Siemers, C.** The influence of thermal conductivity on segmented chip formation. *Comput. Mater. Sci.*, 2003, 26, 175–182.
- [BÄK05] **Bäker M.** Finite element investigation of the flow stress dependence of chip formation. *J. Mat. Proc. Tech.*, 2005, 167(1), 1–13.

- [BAR05] **Barge M, Hamdi H, Rech J, Bergheau J M.** Numerical modelling of orthogonal cutting: influence of numerical parameters. *J. Mat. Proc. Tech.*, 2005, 164, 1148–1153.
- [BEL05] **Belhadi S, Mabrouki T, Rigal J F, Boulanouar L.** Experimental and numerical study of chip formation during a straight turning of hardened AISI 4340 steel. *IMech E part b. J. Engng. Mfg.*, 2005, 219(7), 515-524.
- [BIS51] **Bishop J F W, Hill R A.** theory of plastic distortion of a polycrystalline aggregate under combined stresses. *Phil. Mag.*, 1951, 42, 414–427.
- [CAL08] **Calamaz M, Coupard D, Girot, F.** A new material model for 2D numerical simulation of serrated chip formation when machining titanium alloy Ti–6Al–4V. *Int. J. Mach. Tools. Mf.*, 2008, 48(3-4), 275-288.
- [CER98] **Ceretti E.** FEM simulations of segmented chip formation in orthogonal cutting: further improvements. *CIRP Int. workshop on modeling of mech. oprns.*, 1998, 8, 1-7.
- [CER99] **Ceretti E, Lucchi M, Altan T.** FEM simulation of orthogonal cutting: serrated chip formation. *J. Mater. Processing Technol.*, 1999, 95(13), 17–26.
- [CHA06] **Chae J, Park S S, Freiheit T.** Investigation of micro cutting operations. *Int. J. Mach. Tools. Mf.*, 2006, 46, 313-332.
- [CHI00] **Childs T H C, Maekawa K, Obikawa T, Yamane Y.** *Metal machining: theory and applications.* Arnold, Paris, 2000.
- [CHR82] **Chryssolouris G.** Effects of machine-tool-workpiece stiffness on wear behaviour of superhard cutting materials. *Ann. CIRP*, 1982, 31(1), 65-69.
- [CHU02] **Chuzhoy L, Devor R E, Kapoor S G, Bammann D J.** Microstructure-level modeling of ductile iron machining. *ASME Trans. J. Mfg. Sci. Engng.* 2002, 124, 162-169.
- [CUS10] <http://www.custompartnet.com> (Access date: February 2010)
- [DIN01] **Dinesh D, Swaminathan S, Chandrasekar S, Farris T N.** An intrinsic size effect in machining due to the strain gradient. In: *Proceedings of 2001 ASME IMECE*, NY, November 11–16, 197–204.
- [DIR01] **Dirikolu M H, Childs T H C, Maekawa K.** Finite element simulation of chip flow in metal machining. *Int. J. Mech. Sci.*, 2001, 43(11), 2699–2713.
- [EE05] **Ee K C, Dillon O W, Jawahir I S.** Finite element modelling of residual stresses in machining induced by cutting using a tool with finite edge radius. *Int. J. Mech. Sci.*, 2005, 47(10), 1611–1628.

- [END95] **Endres W J, Devor R E, Kapoor S G.** A dual mechanism approach to the prediction of machining forces—Parts 1 and 2. *ASME J. Engg. Ind.* 1995, 117(4), 526–41.
- [FAN03] **Fang N.** Slip-line modeling of machining with a rounded-edge tool—part II: analysis of the size effect and shear strain-rate. *J. Mech. Phys. Solids*, 2003, 51(4), 743-762.
- [FAN05] **Fang N, Wu Q.** The effects of chamfered and honed tool edge geometry in machining of three aluminium alloys. *Int. J. Mach. Tools Mf.*, 2005, 45(10) 1178–1187.
- [FLE93] **Fleck N A, Hutchinson J W.** A phenomenological theory for strain gradient effects in plasticity. *J. Mech. Phys. Solids*, 1993, 41(12), 1825–1857.
- [FLE94] **Fleck N A, Muller, G M, Ashby M F, Hutchinson J W.** Strain gradient plasticity: theory and experiments. *Acta Metallurgica et Materialia*, 1994, 42(2), 475-487.
- [FRO82] **Frost H J, Ashby M F.** *Deformation-Mechanism Maps.* Pergamon Press, Elmsford, 1982, 1-16.
- [FUR88] **Furukawa Y, Moronuki N.** Effect of material properties on ultra precision cutting process. *CIRP Ann.*, 1988, 37(1), 113-116.
- [GAG07] **Gagnol V, Bouzgarrou B C, Ray P, Barra C.** Model-based chatter stability prediction for high-speed spindles. *Int. J. Mach. Tools Mf.*, 2007, 47(7-8), 1176-1186.
- [GAO99] **Gao H, Huang Y, Nix W D, Hutchinson J W.** Mechanism-based strain gradient plasticity - I. Theory. *J. Mech. Phys. Solids*, 1999, 47(6), 1239-1263.
- [GIR10] **Girardin F, Remond D, Rigal J F.** High frequency correction of dynamometer for cutting force observation in milling. *J. Mfg. Sci. Engg., Transactions of the ASME*, 2010, 132, 1–8.
- [GUO00] **Guo Y B, Dornfeld D A.** Finite element modeling of burr formation process in drilling 304 Stainless Steel. *J. Mfg. Sci. Engng.*, 2000, 122(4), 612– 619.
- [GUO02] **Guo Y B, Liu C R.** 3D FEA modeling of hard turning. *ASME Trans. J. Mfg. Sci. Engng.*, 2002, 124(2), 189–199.
- [GUO04] **Guo Y B.** A FEM study on mechanisms of discontinuous chip formation in hard turning. *J. Mat. Proc. Tech.*, 2004, 155, 1350-1356.

- [HAG08] **Haglund A J, Kishawy H A, Rogers R J.** An exploration of friction models for the chip–tool interface using an Arbitrary Lagrangian–Eulerian finite element model. *Wear*, 2008, 265, 452-460.
- [HAS99] **Hashimura M, Chang Y P, Dornfeld D.** Analysis of burr formation in orthogonal cutting. *J. Mfg. Sci. Engng.*, 1999, 121(1), 1-7.
- [HIG08] **Hignette C.** Master research report on micro milling operation on A2024-T351. 2008, INSA de Lyon France.
- [HIL76] **Hillerborg A, Modeer M, Petersson P E.** Analysis of crack formation and crack growth in concrete by means of fracture mechanics and finite elements. *Cement & Concrete Res.*, 1976, 6, 773–782.
- [HOV06] **Hovsepian P Eh, Luo Q, Robinson G, Pittman, M, Howarth M, Doerwald D, Tietema R, Sim W M, Deeming A, Zeus T.** TiAlN/VN superlattice structured PVD coatings: a new alternative in machining of aluminium alloys for aerospace and automotive components. *Surface & Coatings Technol.*, 2006, 201(1-2), 265–272.
- [HUA00] **Huang Y, Xue Z, Gao H, Nix W D, Xia Z C.** A study of micro-indentation hardness tests by mechanism-based strain gradient plasticity. *J. Mater. Res.*, 2000, 15, 1786–1796.
- [HUA04] **Huang Y, Qu S, Hwang K C, Li M, Gao H.** A conventional theory of mechanical-based strain gradient plasticity. *Int. J. Plast.*, 2004, 20, 753–82.
- [IWA84] **Iwata K, Osakada K, Terasaka Y.** Process modeling of orthogonal cutting by the rigid plastic finite element method. *ASME Trans. J. Engng. Ind.*, 1984, 106, 132–138.
- [JIA08] **Jiang H, Long X, Meng G.** Study of the correlation between surface generation and cutting vibrations in peripheral milling. *J. Mat. Proc. Tech.*, 2008, 208(1-3), 229-238.
- [JIN04] **Jing S, Liu C R.** The influence of material models on finite element simulation of machining. *ASME. J. Mfg. Sci. Engng.*, 2004, 126(4), 849-857.
- [JOH85] **Johnson G R, Cook W H.** Fracture characteristics of three metals subjected to various strains, strain rates, temperatures and pressures. *Engng. Fract. Mech.*, 1985, 21(1), 31–48.
- [JOS04] **Joshi S S, Melkote S N.** An explanation for the size-effect in machining based on strain gradient plasticity. *J. Mfg. Sci. Engng., Transactions of the ASME*, 2004, 126(4), 679–684.

- [KAL07] **Kalay F.** Master research report on La coupe des alliages d'aluminium: contribution à la compréhension du comportement elasto-thermo-plastique : application à l'AU4G (A2024-T351). 2007, INSA de Lyon, France.
- [KAL97] **Kalhuri V, Lundblad M, Lindgren L E.** Numerical and experimental analysis of orthogonal metal cutting. *ASME Trans. J. Mfg. Sci. engng.*, 1997, 6(2), 29–35.
- [KAR06a] **Karpat Y, Özel T.** Predictive analytical and thermal modelling of orthogonal cutting process—part I: predictions of tool forces, stresses, and temperature distributions. *Int. J. Mfg. Sci. Engng.*, 2006, 128(2), 435–444.
- [KAR06b] **Karpat Y, Özel T.** Predictive analytical and thermal modelling of orthogonal cutting process—part II: predictions of tool forces, stresses, and temperature distributions. *Int. J. Mfg. Sci. Engng.*, 2006, 128(2), 445–453.
- [KEG65] **Kegg R L.** Cutting dynamics in machine tool chatter. *Trans. ASME, J. Eng. Ind.*, 1965, 464-470.
- [KIM04a] **Kim C J.** Mechanism of the chip formation and cutting dynamic of the micro scale milling process. PhD thesis, 2004, University of Michigan.
- [KIM04b] **Kim B, Schmittiel M C, Degertekin F L, Kurfess T R.** Scanning grating micro interferometer for MEMS metrology. *J. Mfg. Sci. Engng.*, 2004, 126, 807–812.
- [KIM99a] **Kim K W, Lee W Y, Sin, HC.** A finite element analysis for the characteristics of temperature and stress in micro-machining considering the size effect. *Int. J. Mach. Tools Mf.*, 1999, 39(9), 1507–1524.
- [KIM99b] **Kim K W, Lee W Y, Sin, H C.** A finite-element analysis of machining with the tool edge considered. *J. Mat. Proc. Tech.*, 1999, 86(13), 45–55.
- [KNO07] <http://www.knovel.com> (Access date: April 2007)
- [KOC03] **Kocks U F, Mecking H.** Physics and phenomenology of strain hardening: the FCC case. *Prog. Mater. Sci.*, 2003, 48, 171–273.
- [KOC70] **Kocks U F.** The relation between polycrystal deformation and single crystal deformation. *Metall. Mater. Trans.*, 1970, 1, 1121–1144.
- [KOP84] **Kopalinsky E M, Oxley P L B.** Size effects in metal removal processes. *Inst. of Phy. Conf. Series Oxford*, 1984, 70, 389-396.
- [KOU02] **Kountanya R K.** Process mechanics of of metal cutting with edge radiused and worn tools. PhD dissertation, 2002, University of Michigan.

- [LAL97] **Lalanne M, Ferraris G.** Rotordynamics prediction in engineering. Second ed., Wiley, England, 1997.
- [LEM05] **Lemaitre J, Desmorat R.** Engineering damage mechanics, ductile, creep, fatigue and brittle failures. Springer, Berlin Heidelberg, 2005, 10–12.
- [LEM88] **Lemaitre J, Chaboche J L.** Mécanique des matériaux solides. 2nd ed., Dunod, 1988, 69–70.
- [LIN92] **Lin Z C, Lin S Y.** A coupled finite element model of thermo-elastic-plastic large deformation for orthogonal cutting. J. Eng. Mater. Tech. Trans. ASME, 1992, 114, 218–226.
- [LIS05] **List G, Nouari M, Géhin D, Gomez S, Manaud J P, Le Petitcorps Y, Girot F.** Behaviour of cemented carbide tools in dry machining of aluminium alloy. Wear, 2005, 259(7-12), 1177–1189.
- [LIU04a] **Liu K, Melkote S N.** A strain gradient based finite element model for micro/meso-scale orthogonal cutting process. Proc. Japan-USA Symposium on Flexible Automation, Denver, Colorado, 2004.
- [LIU04b] **Liu X, DeVor R E, Kapoor S G, Ehman K F.** The mechanics of machining at micro scale: assessment of the current state of the science. J. Manuf. Sci. Engg. 2004, 126, 666–678.
- [LIU05] **Liu B, Huang Y, Li M, Hwang K C, Liu C.** A study of the void size effect based on the Taylor dislocation model. Int. J. Plas., 2005, 21(11), 2107-2122.
- [LIU06] **Liu K, Melkote S N.** Material strengthening mechanisms and their contribution to size effect in micro-cutting. J. Manuf. Sci. Engg. 2006, 128(3), 730–738.
- [LIU07] **Liu K, Melkote S N.** Finite element analysis of the influence of tool edge radius on size effect in orthogonal micro-cutting process. Int. J. Mech. Sci., 2007, 49(5), 650-660.
- [LUC93] **Lucca D A, Rhorer R L, Komanduri R.** Effect of tool edge geometry on energy dissipation in ultraprecision machining. CIRP Ann., 1993, 42(1), 83-86.
- [MAB06] **Mabrouki T, Rigal J F.** A contribution to a qualitative understanding of thermo-mechanical effects during chip formation in hard turning. J. Mat. Proc. Tech., 2006, 176, 214–221.
- [MAB08] **Mabrouki T, Girardin F, Asad M, Rigal J F.** Numerical and experimental study of dry cutting for an aeronautic aluminium alloy (A2024-T351). Int. J. Mach. Tools Mf., 2008, 481(11), 187-1197.

- [MAD00] **Madhavan V, Chandrasekar S, Farris T N.** Machining as a wedge indentation. *ASME Trans. J. Appl. Mech.*, 2000, 67(1), 128–139.
- [MAM01] **Mamalis A G, Horvath M, Branis A S, Manolakos D E.** Finite element simulation of chip formation in orthogonal metal cutting. *J. Mat. Proc. Tech.*, 2001, 110, 19-27.
- [MAR01] **Marusich T D.** Effects of friction and cutting speed on cutting force. *Proceedings of ASME Manuf. Engng. Div.*, 2001, 115–23.
- [MAT07] <http://www.matweb.com> (Access date: April 2007)
- [MER44] **Merchant M E.** Basic mechanics of the cutting process. *ASME Trans. J. Applied Mechanics*, 1944, 11, 168-175.
- [MON91] **Montgomery D, Altintas Y.** Mechanism of cutting force and surface generation in dynamic milling. *J. Engng. Ind.*, 1991, 113(2), 160-168.
- [NAK67] **Nakayama K, Tamura K.** Size effect in metal cutting force. *ASME Trans.*, 1967, 9.
- [NAK68] **Nakayama K, Tamura K.** Size effect in metal cutting force. *Transactions of ASME J Engng. for Ind.*, 1968, 90 (1), 119-126.
- [NI06] **Ni W, Cheng Y T, Weiner A M, Perry T A.** Tribological behaviour of diamond-like carbon (DLC) coatings against aluminium alloys at elevated temperatures. *Surface and Coatings Technology*, 2006, 201(6), 3229–3234.
- [NIC02] **Nicolaou P, Thurston D L, Carnahan J V.** Machining quality and cost estimation and tradeoffs. *ASME Trans. J. Mfg. Sci. engng.*, 2002, 124, 840–851.
- [NIX98] **Nix W D, Gao H.** Indentation size effects in crystalline materials: a law for strain gradient plasticity. *J. Mech. Phys. Solids*, 1998, 46, 411–425.
- [NOU03] **Nouari M, List G, Girot F, Coupard D.** Experimental analysis and optimisation of tool wear in dry machining of aluminium alloys. *Wear*, 2003, 255(7-12), 1359–1368.
- [OBI96] **Obikawa T, Usui E.** Computational machining of titanium alloy-finite element modeling and a few results. *ASME Trans. J. Mfg. Sci. Engng.*, 1996, 118(2), 208–215.
- [OBI97] **Obikawa T, Sasahara H, Shirakashi T, Usui E.** Application of computational machining method to discontinuous chip formation. *J. Mfg. Sci. Engng.*, 1997, 119, 667-674.

- [OHB05] **Ohbuchi Y, Obikawa T.** Adiabatic shear in chip formation with negative rake angle. *Int. J. Mech. Sci.*, 2005, 47(9), 1377–1392.
- [ORH07] **Orhan S, Osman Er A, Camuscu N, Aslan E.** Tool wear evaluation by vibration analysis during end milling of AISI D3 cold work tool steel with 35 HRC hardness. *NDT & E international*, 2007, 40(2), 121-126.
- [ÖZE00] **Özel T, Altan T.** Determination of workpiece flow stress and friction at the chip-tool contact for high speed cutting. *Int. J. Mach. Tools Mf.*, 2000, 40, 133-152.
- [ÖZE06] **Özel T.** The influence of friction models on finite element simulations of machining. *Int. J. Mach. Tools Mf.*, 2006, 46(3), 518–530.
- [PAR96] **Park I W.** Modeling of burr formation processes in metal cutting. PhD dissertation, 1996, Dept. of Mech. Engng., Uni. of California at Berkeley.
- [RAM02] **Ramesh A.** Prediction of process-induced microstructural changes and residual stresses in orthogonal hard machining. PhD dissertation, 2002, Georgia Institute of Technology.
- [RAS08] **Rashid A, Mihai-Niculescu C.** Design and implementation of tuned viscoelastic dampers for vibration control in milling. *Int. J. Mach. Tools Mf.*, 2008, 48(9), 1036-1053.
- [REC09] **Rech J, Claudin C, Eramo E D.** Identification of a friction model-Application
- [REC64] **Recht R F.** Catastrophic thermoplastic shear. *J. app. Mech*, 1964, 86, 189-193.
- [RIV90] **Rivin E I, Kang H L.** Improving cutting performance by using boring bar with torsionally compliant head. *Trans of NAMRAI-SME*, 1990, 230-236.
- [RIV92] **Rivin E I, Kang H L.** Enhancement of dynamic stability of cantilever tooling structures. *Int. J. Mach. Tools Mf.*, 1992, 32(4), 539-562.
- [SAN07] <http://www.sandvik.com>. (Access date: April 2007)
- [SCH00] **Schimmel R J, Manjunathaiah J, Endres W J.** Edge radius variability and force measurement considerations. *ASME, J. Mfg. Sci. Engng.*, 2000, 122(3), 590-593.
- [SCH02] **Schimmel R J, Endres W J.** Application of an internally consistent material model to determine the effect of tool edge geometry in orthogonal cutting. *ASME Trans.*, 2002, 124, 536-543.
- [SEK93] **Sekon G S, Chenot J L.** Numerical simulation of continuous chip formation during non steady orthogonal cutting. *Engng. Comput.*, 1993, 10, 31-48.

-
- [SHA84] **Shaw M C.** Metal cutting principles. Oxford University Press Inc., New York, 1984.
- [SHI04] **Shi G, Deng X, Shet C.** The J -integral and geometrically necessary dislocations in non uniform plastic deformation. *Int. J. Plas.*, 2004, 20(8), 1739–1762.
- [SHI74] **Shirakashi T, Usui E.** Simulation analysis of orthogonal metal cutting mechanism. *Proc. 1st int. Conf. Prod. Engng. part I*, 1974, 535–540.
- [SHI90] **Shih A J, Chandrasekar S, Yang H T.** The finite element simulation of metal cutting processes with strain-rate and temperature effects. *ASME Publication PED*, 1990, 43, 11–24.
- [SRE00] **Sreejith P S, Ngoi B K A.** Dry machining: machining of the future. *J. Mat. Proc. Tech.*, 2000, 101(1-3), 287–291.
- [STE93] **Stelmashenko N A, Walls M G, Brown L M, Milman Y V.** Micro indentation on W and Mo oriented single crystals: an STM study. *Acta Metallurgica et Materialia*, 1993, 41 (10), 2855-2865.
- [SUB08] **Subbiah S, Melkote S N.** Effect of finite edge radius on ductile fracture ahead of the cutting tool edge in micro-cutting of Al2024-T3. *Mater. Sci. Engng. A*, 2008, 474(1-2), 283–300.
- [TAT08] **Tatar K, Gren P.** Measurement of milling tool vibrations during cutting using laser vibrometry. *Int. J. Mach. Tools Mf.*, 2008, 48(3-4), 380-387.
- [TAY34] **Taylor G I.** The mechanism of plastic deformation of crystals. Part I. – Theoretical. *Proc. Roy. Soc. (London)*, 1934, 145, 362–387.
- [TEN06] **Teng X, Wierzbicki T.** Evaluation of six fracture models in high velocity perforation engineering. *Fract. Mech.*, 2006, 73(12), 1653–1678.
- [UMB04] **Umbrello D, Hua J, Shivpuri R.** Hardness-based flow stress and fracture models for numerical simulation of hard machining AISI 52100 bearing steel. *Mater. Sci. Engng. A*, 2004, 374(1-2), 90–100.
- [USU82] **Usui E, Shirakashi T.** Mechanics of machining from descriptive to predictive theory, on the art of cutting metals-75 years later. *ASME Trans.*, 1982, 7, 13-15.
- [VAZ07] **Vaz Jr M, Owen D R J, Kalhori V, Lundblad M, Lindgren L M.** Modelling and simulation of machining processes. *Arch. Comput. Methods Engng.*, 2007, 14(2), 173-204.
-

- [VER02] **Vernaza-Pena K M, Mason J J, Li M.** Experimental study of the temperature field generated during orthogonal machining of an aluminium alloy, *Expt. Mechanics*, 2002, 42(2), 221–229.
- [VOG04] **Vogler M P, Devor R E, Kapoor S G.** On the modeling and analysis of machining performance in micro end milling, *J. Manuf. Sci. Engg.*, 2004, 126 (4), 685–705.
- [WAL96] **Waldorf D J.** Shearing, Ploughing and wear in orthogonal machining. PhD thesis, 1996, University of Illinois at Urbana-Champaign.
- [WEN06] **Wen Q, Guo Y B, Todd B A.** An adaptive FEA method to predict surface quality in hard machining. *J. Mater. Processing Technol.*, 2006, 173(1), 21–28.
- [WEU01] **Weule H, Huntrup V, Tritschler H.** Micro cutting of steel to meet new requirements in miniaturization. *Ann. CIRP*, 2001, 50, 61-64.
- [WIL00] **Williams Jr D C.** *Materials Science and Engineering: An Introduction.* Chapter 5, Wiley, New York, 2000.
- [WU88] **Wu DW.** Application of a comprehensive dynamic cutting force model to orthogonal wave generating processes. *Int. J. Mech. Sci.* 1988, 30(8), 581–60.
- [XIA03] **Xiao M, Sato K, Karube S, Soutone T.** the effect of tool nose radius in ultrasonic vibration cutting of hard metal, *Int. J. Mach. Tools. Mf.*, 2003, 43,1375-1382.
- [XIE94] **Xie J Q, Bayoumi A E, Zbib H M.** Characterization of chip formation and shear banding in orthogonal machining using finite element analysis. *ASME Trans., Mater. Instabilities Theory and Application*, 1994, 183, 285-301.
- [XIN08] **Xinmin L, Hongtao L, Chengfeng L, Zhongqin L, Jun N.** Modelling and analysis of micro scale milling considering size effect, micro cutter edge radius and minimum chip thickness, *Int. J. Mach. Tools. Mf.*, 2008, 48(1),1-14.
- [XUE02] **Xue Z, Huang Y, Li M.** Particle size effect in metallic materials: a study by the theory of mechanism-based strain gradient plasticity. *Acta Materialia*, 2002, 50(1), 149–160.
- [YAN02] **Yang X, Liu C R.** A new stress based model of friction behaviour in machining and its significant impact on residual stresses. *Int. J. Mech. Sci.*, 2002, 44, 703–723.
- [YEN04] **Yen Y C, Jain A, Altan T.** A finite element analysis of orthogonal machining using different tool edge geometries. *J. Mat. Proc. Tech.*, 2004, 146(1), 72–81.

- [ZAG09] **Zaghbani, I, Songmene V.** A force-temperature model including a constitutive law for dry high speed milling of aluminium alloys. *J. Mat. Proc. Tech.*, 2009, 209(5), 2532-2544.
- [ZOR63] **Zorev N N.** Interrelationship between shear processes occurring along tool face and on shear plane in metal cutting. *ASME Proc. int. research Prod. Engng. Conf.*, New York, 1963, 42–49.

FOLIO ADMINISTRATIF

THESE SOUTENUE DEVANT L'INSTITUT NATIONAL DES SCIENCES APPLIQUEES DE LYON

NOM : ASAD

DATE de SOUTENANCE : 17 septembre 2010

Prénoms : Muhammad

TITRE : Elaboration de concepts et méthodologies pour l'étude du fraisage lors du passage d'échelles macro-micro

NATURE : Doctorat

Numéro d'ordre : 10 ISAL

Ecole doctorale : MEGA

Spécialité : Mécanique- Génie Mécanique

Cote B.I.U. - Lyon : T 50/210/19 /

et

bis

CLASSE :

RESUME :

Aujourd'hui, la méthode des éléments finis est suffisamment développée pour apporter aux ingénieurs, une aide indispensable lors des étapes de conception et d'optimisation des produits manufacturés. Dans certains cas, cette aide dépasse la simple assistance technologique et permet de considérer des lois physiques dans l'intimité d'un milieu inaccessible aux expériences (fission et fusion nucléaire, propagation des fissures dans les matériaux,...). C'est dans ce contexte à la fois scientifique et technologique que porte notre contribution sur la formation du copeau. D'un point de vue applicatif et expérimental, notre étude est centrée sur l'usinage de l'alliage d'Aluminium A2024-T351. Cette étude a été accomplie avec 4 étapes principales. La première étape porte sur la mise au point d'un modèle numérique 2D, de coupe orthogonale en tournage. Ce travail permet de choisir des solutions de détails pour ce modèle numérique, aussi bien au niveau de la discrétisation et de la partition du maillage qu'au niveau du comportement du matériau usiné sur les aspects cruciaux d'endommagement et d'énergie de rupture. Lors de la deuxième étape ce modèle a été adapté au cas du fraisage de profil en avalant avec un angle d'hélice nul, où la matière susceptible d'être enlevée a une forme en demi lune, constant sur sa largeur, présente une épaisseur continûment variable et tendant vers zéro. Ce travail et les résultats obtenus permettent de distinguer la zone de coupe macroscopique de la zone microscopique à partir de l'épaisseur coupée. L'effet de taille bien connu en micromécanique a ainsi été retrouvé lors de ce passage macro-micro à travers l'influence de l'écrouissage due à la vitesse de déformation du matériau. Le phénomène bien connu expérimentalement de l'augmentation quasi exponentielle de l'énergie spécifique de coupe avec la diminution de l'épaisseur coupée a été étudié en relation avec les divers aspects de cet effet de taille. Pour faciliter l'exploitation et proposer un outil de compréhension physique de l'enlèvement de matière à la communauté scientifique et à l'industrie, dans une troisième étape, le modèle de comportement de « Johnson-Cook » modifié par une approche basée sur le second gradient de déformation a été développé dans ABAQUS®/EXPLICIT sous la forme d'un sous programme (ou sous-routine VUMAT). Finalement, au cours de la quatrième étape, l'application a été complètement développée pour simuler le fraisage de profil en avalant, de l'alliage d'Aluminium A2024-T351. En plus de l'effet de taille interne au copeau, les aspects dynamiques liés au comportement du système usinant ont été pris en compte à travers un modèle multi-échelle nommé « modèle dynamique hybride de coupe (HDC-modèle) » qui combine la rigidité équivalente d'une fraiseuse à grande vitesse (outil, porte-outil, broche, ...) au niveau macroscopique avec la mécanique de formation de copeau au niveau mésoscopique. Cette application intégrant à la fois les effets d'échelles a pour but de fournir des données numériques sur la surface usinée qui puissent être comparées à des résultats expérimentaux. Malgré les difficultés de modélisation nous avons tenu à élaborer ce modèle complet car c'est bien la partie microscopique de la coupe en dynamique haute fréquence ou grande vitesse qui génère la surface usinée. Pour finir, des coupes expérimentales ont été exécutées en tournage et en fraisage pour valider les modèles proposés. Les résultats numériques sont ainsi comparés à ceux expérimentaux à chacune des étapes. De manière générale la concordance des résultats est bonne. Il faut cependant noter le grand nombre de paramètres des modèles numériques qui certains d'entre eux peuvent être des paramètres de recalage expérimental. Il apparaît donc que le caractère prédictif du modèle est limité essentiellement par les caractéristiques physiques de la matière usinée. On se retrouve dans la situation purement expérimentale des années 1970-80 qui a vu naître la notion de couple outil-matière (COM). L'approche d'aujourd'hui, à la fois expérimentale et numérique permet cependant de réduire fortement les coûts et de quantifier des phénomènes locaux très intéressants comme par exemple dans notre contribution : La propension à la segmentation et donc à la fragmentation dans certaines conditions de coupe, La longueur du contact copeau, face de coupe, l'amplitude des défauts de la surface usinée due à la dynamique globale,.....

MOTS-CLES : Simulation numérique, Élément fini, Coupe orthogonal, Johnson-Cook, Endommagement, Effet de taille, Vitesse de déformation, Second gradient de déformation, Sous-routine Vumat, Segmentation de copeau, Modèle de coupe dynamique, A2024-T351, Expérimentation

Laboratoire (s) de recherche : Laboratoire de Mécanique des Contacts et des Structures

Directeur de thèse: Tarek MABROUKI, Jean François RIGAL

Président de jury :

Composition du jury : Martin BÄKER, Jean-Claude BOYER, Benjamin HAGEGE, Philippe LORONG, Tarek MABROUKI, Joël RECH, Jean François RIGAL